UNIVERSIDADE ESTADUAL PAULISTA
"JÚLIO DE MESQUITA FILHO"
Campus de Botucatu

FACULDADE DE CIÊNCIAS AGRONÔMICAS
UNESP | BOTUCATU

ANDERSON LUIZ DOS SANTOS SAFRE

EVAPOTRANSPIRATION AND SOIL MOISTURE ESTIMATION USING DIFFERENT REMOTE SENSING PLATFORMS

Botucatu

2022

ANDERSON LUIZ DOS SANTOS SAFRE

EVAPOTRANSPIRATION AND SOIL MOISTURE ESTIMATION USING DIFFERENT REMOTE SENSING PLATFORMS

Thesis presented to Faculdade de Ciências Agronômicas of Unesp Câmpus de Botucatu, to obtain the title of Doctor in Agronomy (Irrigation and Drainage).

Advisor: João Carlos Cury Saad
Co-adivisors: Alfonso Torres-Rua and Rodrigo Lilla Manzione

Botucatu

2022

S128e

Safre, Anderson Luiz dos Santos
Evapotranspiration and soil moisture estimation using different remote sensing platforms / Anderson Luiz dos Santos Safre. -- Botucatu, 2022
114 p. : tabs., mapas

Tese (doutorado) - Universidade Estadual Paulista (Unesp), Faculdade de Ciências Agronômicas, Botucatu
Orientador: João Carlos Cury Saad
Coorientador: Rodrigo Lilla Manzione

1. Remote Sensing. 2. Evapotranspiration. 3. Soil Moisture. I. Título.

Sistema de geração automática de fichas catalográficas da Unesp. Biblioteca da Faculdade de Ciências Agronômicas, Botucatu. Dados fornecidos pelo autor(a).

Essa ficha não pode ser modificada.

UNIVERSIDADE ESTADUAL PAULISTA

Câmpus de Botucatu

CERTIFICADO DE APROVAÇÃO

TÍTULO DA TESE: EVAPOTRANSPIRATION AND SOIL MOISTURE ESTIMATION USING DIFFERENT REMOTE SENSING PLATFORMS

AUTOR: ANDERSON LUIZ DOS SANTOS SAFRE
ORIENTADOR: JOÃO CARLOS CURY SAAD
COORIENTADOR: RODRIGO LILLA MANZIONE

Aprovado como parte das exigências para obtenção do Título de Doutor em AGRONOMIA (IRRIGAÇÃO E DRENAGEM), pela Comissão Examinadora:

Prof. Dr. JOÃO CARLOS CURY SAAD (Participaçao Presencial)
Engenharia Rural e Socioeconomia / Faculdade de Ciencias Agronomicas de Botucatu UNESP

Prof. Dr. EDSON LUÍS PIROLI (Participaçao Virtual)
Coordenadoria Executiva / Unesp - Câmpus de Ourinhos

Prof. Dr. ANTÔNIO HERIBERTO DE CASTRO TEIXEIRA (Participaçao Virtual)
. / Universidade Federal de Sergipe

Prof. Dr. RUBENS DUARTE COELHO (Participaçao Virtual)
Engenharia de Biossistemas / Escola Superior de Agricultura Luiz de Queiroz

Prof. Dr. RODRIGO MÁXIMO SÁNCHEZ ROMÁN (Participaçao Presencial)
Engenharia Rural e Socioeconomia / Faculdade de Ciencias Agronomicas de Botucatu UNESP

Botucatu, 19 de abril de 2022

To my beloved wife and son,

Gabryella and Lucas,

I dedicate

ACKNOWLEDGEMENTS

I did like to thank my advisor, Dr. João Carlos Cury Saad for accepting me and helping me though this rough journey of my PhD.

I am profoundly grateful to my co-advisor Dr. Alfonso Torres-Rua for helping me at Utah State University and for showing me a different and exciting way of seeing science and life.

I am grateful for my co-advisor Dr. Rodrigo Lilla Manzione, who helped me several times trough conversations and exploring the data.

The present work was carried out with the support of the Coordenação de Aperfeiçoamento de Pessoal de Nivel Superior – Brasil (CAPES) Código de Financiamento DS 88882.433001/2019-01 and DS 88887.646410/2021-01 and the PrInt doctoral program of the same agency Código 88887.467878/2019-00.

ABSTRACT

Evapotranspiration (ET) and soil moisture (SM) are important parameters for agricultural water management. Sensors mounted on remote sensing platforms such as satellites and Unamed Aerial Vehicles (UAVs) can provide reliable information on crop reflectance at different spatial, temporal and radiometric resolution. Machine learning nonlinear approach have shown the potential of estimating SM using optical images. The Simple Algorithm for Evapotranspiration Retrieval (SAFER) uses data from remote sensing and meteorological stations for the energy balance estimations and then actual evapotranspiration. We evaluated the performance of SAFER to estimate ET. First, we evaluated the results of SAFER using Landsat 8 imagery (30 m pixel size for optical bands and 100 m for thermal within a 18 days revisit) from 2013-2017 and standard coefficients. Then the regression coefficients were calibrated using data from Eddy Covariance (EC) towers and the results from field and remote sensing were compared. The next step was to assess SAFER performance and calibrate the algorithm with Sentinel-2 (10 m pixel size and 5 days revisit) imagery. SAFER results using the thermal band and using only optical bands were compared with six EC flux stations, located at two different sites. We applied Support Vector Regression (SVR), Random Forest (RF) and Artificial Neural Network (ANN) machine learning algorithms to estimate the soil moisture from UAV high-resolution images (2.4 cm/pix). Three bands (G, R, NIR) and NDVI was used as input. After the model calibration SAFER showed good agreement with EC data using Landsat-8 and Sentinel-2. In the Landsat-8 dataset the RMSE was 0.70 mm d^{-1} using the data from 5 years. The lowest RMSE (0.53 mm d^{-1}) was in 2015 and the highest RMSE (0.89 mm d^{-1}) in 2013. Seasonal ET was estimated and compared with the EC flux towers, showing an R^2 that ranged between 0.29 to 0.97. Regarding the SAFER using Sentinel-2 images results, the model RMSE was between 0.62 to 0.84 mm d^{-1}. The model tends to underestimate ET values when there is less water available in the root zone. The seasonal ET estimated using Sentinel-2 images showed a R^2 of 0.64, when compared to that from EC measurements. Results show that all three machine learning algorithms had a great performance on the estimation of soil moisture with RMSE < 1%. SVR was the best model with a RMSE of 0.45 % and R^2 = 0.71. We conclude that UAVS data and machine learning can be a great tool for soil moisture spatial variability modeling in heterogeneous terrains.

Keywords: remote sensing; evapotranspiration; eddy covariance; machine learning, soil moisture.

RESUMO

Evapotranspiração (ET) e umidade do solo (US) são importantes parâmetros para a gestão da água na agricultura. Sensores equipados em plataformas de sensoriamento remoto, como satélites e Veiculos Áreos Não Tripulados (VANT's), podem fornecer informações confiáveis sobre a reflectância das culturas em diferentes resoluções espaciais, temporais e radiométricas. A abordagem não linear de aprendizado de máquina mostrou o potencial de estimar a US usando imagens ópticas. O Simple Algorithm for Evapotranspiration Retrieval (SAFER) usa dados de sensoriamento remoto e dados de estações meteorológicas para estimar a ET. Avaliamos o desempenho do SAFER na estimativa da ET atual. Primeiro, avaliamos os resultados do SAFER usando imagens do Landsat-8 (tamanho do pixel de 30 m e revisita de 18 dias) de 2013-2017 e coeficientes padrões. Em seguida, os coeficientes do modelo foram calibrados usando dados de torres Eddy Covariance (EC) e os resultados foram avaliados. A próxima etapa foi avaliar o desempenho do SAFER e calibrar o modelo nas imagens do Sentinel-2B (tamanho de pixel de 10 m e revisita de 5 dias). Aplicamos algoritmos de aprendizado de máquina de Support Vector Regression (SVR), Random Forest (RF) e Artificial Neural Network (ANN) para estimar a umidade do solo a partir de imagens de alta resolução de VANT. Três bandas (G, R, NIR) e NDVI foram usados como entrada. Após a calibração do modelo, o SAFER mostrou boa concordância com os dados do EC usando Landsat-8 e Sentinel-2. No conjunto de dados Landsat-8, o RMSE foi 0,70 mm d^{-1} usando os dados de 5 anos. O menor RMSE (0,53 mm d^{-1}) foi em 2015 e o maior RMSE (0,89 mm d^{-1}) em 2013. A ET sazonal foi estimada e comparada com as torres de fluxo EC, apresentado um R^2 que variou entre 0,29 a 0,97. Em relação aos resultados do SAFER usando imagens Sentinel-2, o RMSE do modelo ficou entre 0,62 a 0,84 mm d^{-1}. O modelo tende a subestimar os valores de ET quando há menos água disponível na zona radicular. A ET sazonal estimada usando imagens Sentinel-2 apresentou R^2 de 0,64 quando comparado ao EC. Os resultados mostram que todos os três algoritmos de aprendizado de máquina tiveram um ótimo desempenho na estimativa da umidade do solo com RMSE < 1%. O SVR foi o melhor modelo com RMSE de 0,45 % e R^2 = 0,71. Concluímos que os dados de VANTs e o aprendizado de máquina podem ser uma ótima ferramenta para modelagem da variabilidade espacial da umidade do solo em terrenos heterogêneos.

Palavras-chave: sensoriamento remoto; evapotranspiração; eddy covariance; machine learning; umidade do solo.

SUMMARY

GENERAL INTRODUCTION **15**

CHAPTER 1 – CALIBRATION AND VALIDATION OF THE SAFER ALGORITHM FOR EVAPOTRASPIRATION ESTIMATION IN COMMERCIAL VINEYARDS IN CALIFORNIA..... 19

1.1 INTRODUCTION..... 20

1.2 MATERIAL AND METHODS..... 23

1.2.1 STUDY AREA…….. 23

1.2.2 SAFER MODEL..... 26

1.2.3 DATA PROCESSING..... 28

1.2.4 EDDY COVARIANCE FOOTPRINT..... 29

1.2.5 STATISTICS…..... 30

1.3 RESULTS AND DISCUSSION..... 31

1.3.1 SATELLITE MEASUREMENTS…..... 31

1.3.2 ET ESTIMATION…… 36

1.3.3 CALIBRATION OF A AND B COEFFICIENTS……. 38

1.3.4 SEASONAL ANALYSIS…… 40

1.3.5 SPATIAL 44

1.4 CONCLUSIONS……. 49

REFERENCES……. 50

CHAPTER 2 – PERFORMANCE OF SENTINEL-2 SAFER ET MODEL FOR DAILY AND SEASONAL ESTIMATION OF GRAPEVINE WATER CONSUPTIOM…… 56

2.1 INTRODUCTION…… 57

2.2 MATERIAL AND METHODS…… 62

2.2.1 STUDY AREA……. 62

2.2.2 IRRIGATION SCHEDULE AND STRATEGY…… 65

2.2.3 SAFER MODEL DESCRIPTION……. 67

2.2.4 AGROMETEOROLOGICAL DATA…… 69

2.2.5 REMOTE SENSING DATA……. 70

2.2.6 FLUX TOWER FOOTPRINT…….. 70

2.3 RESULTS AND DISCUSSION…… 71

2.3.1 LST ESTIMATION……. 71

2.3.2 MODEL CALIBRATION AND ET_A ESTIMATION PERFOMANCE……. 74
2.3.3 SEASONAL ET ESTIMATION……..... 79
2.3.4 SPATIAL ANALYSIS……. 84
2.4 CONCLUSION..... 86
REFERENCES……... 88
CHAPTER 3 – ESTIMATIVA DE UMIDADE DO SOLO POR MEIO DE APRENDIZADO DE MÁQUINA USANDO IMAGENS DE VEÍCULO AÉREO NÃO TRIPULADO (VANT)…… 93
3.1 INTRODUÇÃO……... 94
3.2 MATERIAL E MÉTODOS……. 95
3.2.1 ÁREA DE ESTUDO……... 95
3.2.2 SUPPORT VECTOR REGRESSION……. 98
3.2.3 RANDOM FORESTS……. 99
3.2.4 ARTIFICIAL NEURAL NETWORK…….. 100
3.2.5 ESTRATÉGIA DE MODELAGEM…… 101
3.2.6 MÉTRICAS ESTATÍSTICAS…… 102
3.4 RESULTADOS E DISCUSSÃO……... 103
3.4.1 UMIDADE DO SOLO E REFLECTÂNCIA…….. 104
3.4.2 PERFOMANCE DOS ESTIMADORES DE MACHINE LEARNING…… 105
3.4.3 MAPAS DE UMIDADE DO SOLO…… 106
3.5 CONCLUSÕES…….. 107
REFERÊNCIAS ……..... 107
GENERAL CONCLUSIONS..... **111**
REFERENCES……..... **113**

GENERAL INTRODUCTION

Total population will reach 9.6 billion on 2050, according to the United Nations Department of Economic and Social Affairs (UNITED NATIONS, 2009). To meet the food demand, the intensification of agricultural lands and the increase in yield are required. This intensification is enabled by increasing irrigation and greater water withdrawals (Dolan et al., 2021). Water scarcity is growing all over the world due to climate changes, requiring precise methods to evaluate crop water consumption. This is especially important in semi-arid areas, that account for about 15% of global land area, and feeds 14% of the global population (Safriel and Adeel, 2005).

Evapotranspiration (ET) is a major component of the water balance and the hydrologic cycle (Sun et al., 2011). Evapotranspiration can be subdivided into tree main concepts: actual evapotranspiration (ET_a), potential evapotranspiration (ET_p) and reference evapotranspiration (ET_0). ET_a is the real value of water loss by crops observed in the field. Is the amount of water vapor released in the atmosphere by the combined effect of plant transpiration and soil evaporation. The potential evapotranspiration as first defined by Thornthwaite (1948), is the maximum value of ET that could occur under ideal conditions. The concept of ET_p is related with plants that have no water or nutrient restrictions and that are not affected by pests and diseases. Therefore, is the “potential” value of ET a full covered crop can reach. The ET_0 was defined by the Food and Agriculture Organization (FAO) of the United Nations as the rate of evapotranspiration from an extensive surface of 8 to 15 cm tall, green grass cover of uniform height, actively growing. The ET_0 when combined with the crop coefficient (Kc) can provide estimates of the actual evapotranspiration.

Methods for measuring ET_a include Lysimeters (López-Urrea et al., 2021), Bowen Ratio (Sousa et al., 2021), Soil water balance (Reichert et al., 2021) and Eddy Covariance (Pang et al., 2021). While EC is the most used observation for ET_a , it only measures the flux in the footprint area (10^2-10^4 m^2), which is determined by the microclimate conditions around the flux tower and the instrument height (Yang et al., 2016). The major limitation of the mentioned methods is the spatial extrapolation of ET_a measurements because in most cases they represent punctual measurents.

Satellite Remote Sensing (RS) can provide information needed for quantifying ET at different spatial and temporal resolutions (Kustas and Norman, 1996). The

Landsat missions by the United States Geological Survey (USGS) and National Aeronautics and Space Administration (NASA), have lunched 9 platforms since 1972 providing an extensive dataset. The Sentinel-2 mission by the European Space Agency (ESA) comprises two platforms Sentinel-2A and Sentinel-2B, launched in June 2015 and March 2017, respectively. The Sentinel satellites can provide images with a pixel size of 10 m in a revisit time of 5 days.

There are several algorithms in literature to estimate ET based on its relationship with RS data. RS based mapping of ET is a cost-effective way its estimatimation, and the mainly methods can be divided into Surface Energy Balance, Penman-Monteith (PM) and surface temperature-vegetation index (T_s-VI) (Zhang et al, 2016). Surface Energy Balance methods include one-source methods such as SEBAL and two-source methods like TSEB (Bastiaanssen et al., 1999; Norman and Kustas 1999). The advantages of using this algorithms is the representation of the ET phenomenon with a spatial approach. However, many of the algorithms mentioned before requires a lot of information, especially related to the calibration of anchor pixels, named cold and hot pixels.

Vegetation indices (like NDVI or SAVI) are also related to surface temperature, i.e., more evapotranspiration tends to be associated with higher temperatures (Couralt et al., 2005). Usually VI-T_s method depends on measurements of reference evapotranspiration (ET_0).

SAFER is an algorithm developed by Teixeira (2010) that estimates the evaporative fraction (ET/ET0) by using the surface albedo, surface temperature and NDVI from remote sensing measurements. The ratio ET/ET_0 is related with the soil moisture, where lower values correspond to water stress conditions while higher values are related to good conditions of water availability, and in this case can be considered as the crop coefficient. The algorithm was initially developed to use Landsat surface reflectance images and the thermal bands for surface temperature calculation. Improvements of the model was done, regarding the estimation of surface temperature as a residual in the radiation equation (Teixeira et al., 2014). made possible the usage of Sentinel-2 images. Both Landsat and Sentinel have their advantages and limitations regarding ET_a estimation, mainly when aiming irrigation management. The ET_a can also be an indicator of yield and water productivity which is a measurement of how much water was used per biomass production. Water

resources managers can understand the water consumption in crops in such a way of finding the optimal amounts required for high productivity. This can help to solve the conflicts among different water users.

The soil moisture (SM) is also a great indicator of crop water stress, and it is strongly correlated with the ET/ET_0 ratio. Rapid acquiring and accurate monitoring of terrestrial SM is not only required in the hydrological research but also a significant benefit can be obtained for water management and agricultural production (Dong and Jin, 2021). Precision agriculture requires detailed soil moisture measurements, especially in heterogenous areas where there is more spatial moisture variability.

Surface soil moisture is also important as it impacts soil evaporation and transpiration, and thus the heat and mass transfers between the Earth and the atmosphere (Kerr, 2006. Recent technological Advances in satellite remote sensing have shown that soil moisture can be measured by a variety of remote sensing techniques, each of them with its own strengths and weakness (Wang and Qu, 2009). The spatial scale of the irrigation processes and the complexity of the study area make necessary the adoption of high-resolution (1km or less) soil moisture products to quantify irrigation requirements (Dari et al., 2021).

Remote sensing methods for retrieving soil moisture provide an alternative to the conventional field ones, which are impractical at large scales (Araya et al., 2021). Remote sensing researches have widely used the L-band microwave to estimate SM. This band has a strong sensibility to SM content in the soil surface, and have been used in Missions like the Soil Moisture and Ocean Salinity (SMOS) from ESA and the Soil Moisture Active Passive (SMPA) from NASA to map global SM. However recent studies have shown the potential of using optical and thermal images acquired from Unnamed Aerial Vehicles (UAV's) to estimate SM using Nonlinear regression methods like machine learning (Aboutalebi et al., 2019; Ge et al., 2019; Araya et al., 2021).

A UAV can be equipped with different sensors, like optical, thermal and radar, offering a large range of wavelengths that can be collected in clear and cloud sky condition. The flights can be scheduled according to farmer needs, making it possible to have high-resolution images in short periods of time. The advantages of machine learning techniques in remote sensing are their ability to learn and approximate complex non-linear mappings and the fact that no assumptions need to be made about the data distribution (Araya et al., 2021). The precision of machine learning algorithms

improves with big datasets, which represents a limitation of these techniques. However, recent technological changes have shown the increasing potential of data collection and distribution.

In this the current research we applied SAFER model for ET estimation and three machine learning algorithms to estimate soil moisture using UAV images. Estimated ET are evaluated in two different sites using six flux towers. Soil moisture content measured at 16 tensiometers along with MAPIR bands (R, G, NIR) and NDVI collected in two surveys were used as training/test dataset. The Objectives are to (1) Calibrate SAFER using data from EC flux towers; (2) evaluate the model performance to estimate daily and seasonal evapotranspiration using Landsat-8 and Sentinel-2 imagery; and (3) assess the performance of three machine learning models to estimate the soil moisture content on UAV data.

CHAPTER 1[1]

Calibration and validation of the SAFER algorithm for Landsat 8 evapotranspiration estimation in commercial vineyards in California

Anderson L. S. Safre[1]. Ayman Nassar[2]. Alfonso Torres-Rua[2]. Mayhar Aboutalebi[3]. João C. C. Saad[1]. Rodrigo L. Manzione[4]. John H. Prueger[5]. Lynn G. McKee[4]. Joseph G. Alfieri[6]. Lawrence E. Hipps[7]. Hector Nieto[8]. William A. White[6]. Maria del Mar Alsina[3]. Luis Sanchez[3]. William P. Kustas[6]. Nick Dokoozlian[3]. Feng Gao[6]. Martha C. Anderson[6]. Antonio Heriberto de Castro Teixeira[9].

Anderson L. S. Safre
anderson.safre@unesp.br

[1] Department of Rural Engineering, Falculdade de Ciências Agrônomicas – UNESP, Botucatu, SP 18610-337, BR

[2] Department of Civil and Environmental Engineering, Utah State University, Logan, UT 84322, USA

[3]E & J Gallo Winery, Viticulture, Chemistry and Enology, Modesto, CA 95354, USA

[4]Department of Biosystems Engineering, Faculdade de Ciências e Engenharia – UNESP, Tupã, SP, 17602-496, BR

[5]National Laboratory for Agriculture and the Environment, USDA ARS, Ames, IA 50011, USA

[6]Hydrology and Remote Sensing Laboratory, USDA ARS, Beltsville, MD 20705-2350, USA

[7]Plants, Soils and Climate Department, Utah State University, Logan, UT 84322-4820, USA

[8]COMPLUTIG, Alcalá de Henares, Madrid 28801, Spain

[9]Embrapa Monitoramento por Satélite, Campinas, SP, 13070-115, BR

Abstract

The water consumption monitoring at different spatial resolutions is important to agricultural water resources managements in a precise and sustainable way. The Simple Algorithm for Evapotranspiration Retrievement (SAFER) model was developed for evapotranspiration (ET) and energy balance estimation with remote sensing images

[1] Paper to be submitted to Agricultural Water Management journal

using the relationship between NDVI, surface albedo and surface temperature. In this research, we evaluate the performance of the SAFER model in ET estimation using Landsat 8 images with ground-based flux measurements in vineyards located in Lodi, California, USA. After performing the calibrations of these equations, the algorithm showed an agreement with the eddy covariance measurements, the RMSE in ET was 0.53 mm in 2015 and 0.89 mm in 2013. Considering all the years the RMSE was 0.70 mm, while the MAE 0.55 and the NSE 0.56. The modelling equations represented well the season behavior of the ET values, with the residuals of 73.41 mm (20%) in 2013 and 7.8 mm (2%) in 2016. The model was able to represent the spatial variations in ET over the different vineyards. Using field energy balance measurements, the model can be calibrated and validated for specific locations and used for daily ET estimation with good accuracy.

.

1.1 INTRODUCTION

Water demand in agriculture has increased as natural vegetation areas are being transformed into agriculture lands for food production. Monitoring the energy and water balances, combining high productivity and precision irrigation is essential for a sustainable use of the resource as the tension between different water uses has increased due to the threat of water scarcity. The success of any dialog depends on the base knowledge and general trust in the source of information, such as actual evapotranspiration (ET) of each land use type (Teixeira, 2010). This is important in semiarid regions where the water availability is restricted, which is the Central Valley case in California.

The state of California has the major production of grapes in the United States with 925,000 acres planted in 2018 (California Department of Food and Agriculture & USDA National Agricultural Statistics Service, 2019). Vineyard is one of the most difficult crops for the ET estimation due to the soil effect in the interrows. The typical architecture of wine grape vineyards in California is characterized by widely spaced rows (~ 3 m) and tall plants (~ 2 m) with most of the biomass concentrated in the upper one-third to one-half of the plant (Kustas el al., 2018).

Actual ET in vineyards can be estimated using eddy covariance towers, Bowen ratio and lysimeters (Yunusa et al., 2004, Zhang et al., 2007, Li et al., 2008, Lopéz-Urrea et al., 2012, Holland et al., 2013). The Eddy Covariance (EC) has been widely

used for the estimation of *Rn*, *G*, *H* and *LE* and is considered the reference methodology to observe the atmospheric turbulence in the surface boundary layer (Camamalieri et al., 2013) However, the method is usually constrained by the lack of surface energy budget closure (Madugundu et al., 2017) and the data is usually restricted at 0.1 to 1 km scales (Rana & Katerji, 2000). Those measurements are punctual and cannot describe the spatial variability of the ET in large fields or multiple fields. One method to efficiently assess and monitor water use and stress in vineyards is through satellite-based estimation of evapotranspiration, quantifying the net flux of water vapor from the crop field to the atmosphere (Semmens et al., 2016).

The main algorithms used for ET estimation can be separated between one-source energy balance and two-source energy balance. The most commons one-source energy balance models are the Surface Energy Balance Algorithm for Land, SEBAL (Bastiaansen et al., 1998), and the Mapping Evapotranspiration with Internalized Calibration, METRIC (Allen et al., 2007), which is a sophisticated and optimized version of SEBAL. These models consider soil and canopy as a single flux source and often employ an additional resistance term because heat transport is less efficient than momentum from land surface (Nieto et al., 2018) These models use hot (bare soil) and cold pixels (irrigated areas) to derive the sensible heat flux, and the main difference is how the function is approximated and additional information for surface roughness can be derived by a digital elevation model. The delimitation of these anchor pixels can lead to great errors in the modeling process, especially during wet seasons when is hard to delimit zero ET (hot pixels)

The Two-Source Energy Balance (TSEB) was introduced by Normal et al., (1995) and has been modified into different versions: Priestley-Taylor (Kustas and Norman, 1999) and Dual Temperature (Nieto et al., 2018). This model separates the surface energy fluxes and radiometric temperature between soil and canopy and incorporated a physical approach to the energy balance estimation. The TSEB model requires the leaf area index, canopy height, fractional cover, canopy width and the ratio between canopy width and canopy height. The results of the model can be affected by the grid resolution and can only be used with high-resolution imagery that can distinguish soil and canopy temperature (Nassar et al., 2020)

The SAFER algorithm, presented by Teixeira (2010), belong to the one-source energy balance models, and use the relationship between the NDVI, Land Surface

Temperature (LST), and Surface Albedo to calculate the ET/ET_0 fraction. The results are then multiplied by the ET_0 to retrieve the daily evapotranspiration. The advantages of the model are that it only requires a few parameters collected by an agrometeorological station or a network of stations using interpolation methods. In addition, its application does not require identification of extreme conditions classifications (wet and cold pixels) making the model practical for commercial irrigation management. The biggest advantage in its applicability is that there is no need of the assumption of zero latent heat in dry pixels because, during the rainy season, the mixed ecosystems are homogenously wet, with the whole region presenting high ET_a rates (Teixeira et al., 2013)

The first version of the SAFER requires thermal images to derive the Land Surface Temperature (LST) and the second version can approximate the LST using a relation between the surface emissivity and atmosphere emissivity which can be explained by the Stefan-Boltzmann law. Hernandez et al., (2014) found good ET_a agreement on corn, beans and sugarcane on center pivot irrigation systems in the northeast of São Paulo, Brazil. Lima el al., (2019) also found a good correlation between SAFER and crop coefficients presented by FAO model 56 in Bahia, Brazil. The ET/ET_0 can also be used to estimate the kc when there is no restrictions to water availability in the root zone

Many studies have applied the SAFER model to different locations without performing the calibration of empirical coefficients related to site-specific conditions (Santos et al., 2020; Nuñez et al., 2017; Sales et al., 2016; Silva et al., 2018) that can lead to a misunderstanding of the ET spatial variability due to inconsistencies in the relationship between surface albedo, NDVI and surface temperature with the evapotranspiration fraction. However, local calibrations may be difficult, due to the high cost and technical operations of EC towers.

In the current study we focus on evaluating the performance of SAFER on the estimating of evapotranspiration using Landsat 8 images compared with EC energy fluxes measured at two different sites in Lodi, California. We did this investigation in order to answer some questions regarding the use of a simple algorithm for daily ET estimation at field scale. How SAFER performs on estimating ET in vineyards using the original regression coefficients? Do SAFER ET estimations follow the seasonal

pattern of ET observed by the Eddy Covariance flux towers? Does the variations in the field are captured by SAFER using the Landsat spatial resolution (30 m)?

1.2 MATERIALS AND METHODS

1.2.1 Study area

The study site is part of the E. & J. Gallo vineyards located near Lodi, California (38.29°N, 121.12°W) in Sacramento County with 120 ha of cropped area. It consists of two vineyard blocks with different age and crop stages of pinot noir for wine production, which are part of the Grape Remote Sensing Atmospheric Profile and Evapotranspiration Experiment (GRAPEX) project run by the USDA Agricultural Research Service in collaboration with E&J Gallo Winery, Utah State University, University of California (Davis) among others (Kustas et al., 2018).

The North vineyard is 6 years old and was planted in 2007 while the South vineyard is 3 years and was planted in 2010. The trellising system and interrow configurations are the same in both experimental fields, with a 3.35 m space between the trellises and east-west orientation in a vertical system. The height of the vines varies between 1.4 and 2.5 m above ground level. The irrigation system consists of drip irrigation lines at 30 cm above ground level (agl) with two emitters (4 L h^{-1}) between each vine. In the interrow the cover crop (a mixture of grasses) is approximately 2 m in width with bare soil on either side approximately 0.7 in width (Kustas et al., 2018a). The vineyards phenological cycles can be divided in 4 major cycles with an average cycle of 6-7 months. The first one in March (Bud break) with significantly cover crop biomass and can be classified as the grape flowering stage. The second one in Mid-June with the cover crop going to senescence and can be classified as berry development stage. The third in Mid-July early August when the vines and fruits are fully developed. The last one is by late August or early September; the vineyard grapes reached the required sugar content and are harvested. The leaves then reach senescence and start to defoliate towards the dormancy period in the winter. (Ohana-Levi et al., 2020). Figure 1 shows the different phenological stages of the vineyards.

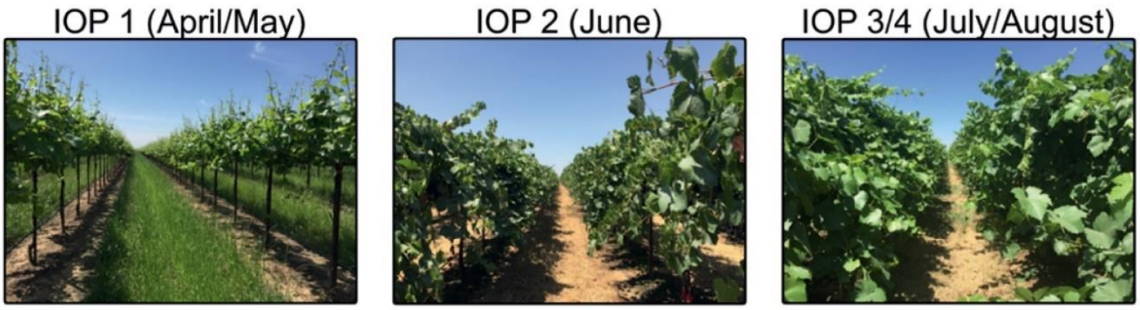

Figure 1. Phenological stages of the vineyards.

Since the 2013 growing season, turbulent fluxes and micrometeorological data have been collected using two eddy covariance flux towers. The towers are located at the east border of the vineyards as shown in Figure 2, due to predominant wind directions and are measuring R_n, LE, H and G. For more detailed information of EC post processing see Alfieri et al. (2019).

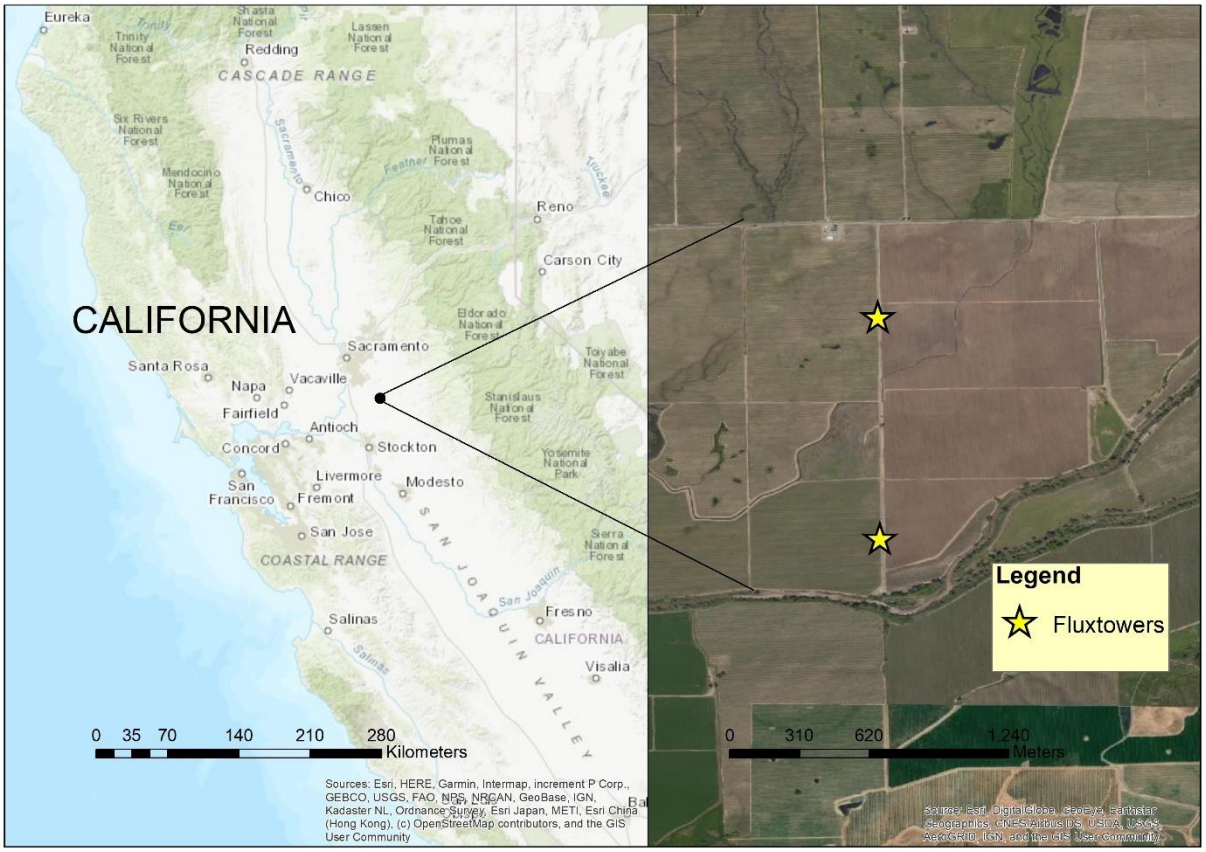

Figure 2. Study area location that shows the position of the 2 EC towers.

The EC data also included wind speed, air temperature, water vapor density, water vapor pressure, air pressure, rain, shortwave radiation, and photosynthetically

active radiation (PAR). Hourly averages were computed for each meteorological variable and the energy budget.

Table 1. Description of field measurements.

Micrometeorological measurement	Instrument	Height
*Wind Speed	Sonic anemometer (CSAT3, Campbell Scientific)	5 m above ground level
Water vapor pressure	Humidity probe (HMP45C, Vaisala, Helsink, Finland)	5 m above ground level
Air Temperature	Gill shielded temperature (Vaisala, Helsinki, Finland)	5 m above ground level
Soil heat flux	Five plates (HFT-3, Radiation Energy Balance Systems, Bellevue, Washington)	-8 cm bellow ground level centered at the midrow
Net Radiation	4-way radiometer (CNR-1, Kipp and Zonen, Delft, The Netherlands)	6 m above ground level

The reference evapotranspiration (ET_0) was calculated using the Ref_ET software considering the Penman-Monteith (PM) equation (Allen, 2000). The data used for the ET_0 calculation was the air temperature, wind speed, actual vapor pressure (e_a), saturation vapor pressure (e_s), global radiation (R_G), and soil heat flux. The maximum and minimum air temperature and their respective e_a and e_s were used to compute the ET_0 daily average values. As the wind speed is slowest at the surface and increases with height, the PM requires that the data be collected at 2 agl. To adjust the wind speed data collected at 5 m agl, the logarithmic wind speed profile was considered (Allen et al., 1998).

To evaluate the SAFER energy balance results, the footprints from the EC towers were estimated for the hourly period of the Landsat-8 passing time using the two-dimensional model developed by Kljun et al. (2015). Because a 100% EC footprint fetch could extend over the study area, a 90% footprint area (90% cutoff) was used for analysis; then, the weighted footprint area was divided by 0.9 (Nassar et al., 2020).

1.2.2 Safer Model

The SAFER algorithm uses satellite images and agrometeorological data to calculate the radiation and energy balance for each pixel. Agtometeorological data include global radiation (R_G), air temperature (T_a) and ET_0. The bands 1 to 7 from Landsat 8 were used to calculate the surface albedo (a_0). The LST can be calculated using the bands 10 and 11 using the equations provided by Landsat developers and linear regression. However, we used the product Landsat Provisional Surface Temperature from USGS. This product offers a more reliable measurement of the surface temperature for the entire United States using emissivity data to calibrate T_0.

SAFER performs an atmospheric correction to Landsat images using a relationship with the planetary albedo and field measurements. The spectral radiance is obtained by the following equation (USGS, 2019):

$$\boldsymbol{L_b = Gain\ x\ DN + Offset} \quad (1)$$

The Gain and offset are the rescaling factors for each band from the MTL file.

The planetary albedo (apb_b) was calculated using the equation:

$$\boldsymbol{ap_b = \frac{L_b \pi d^2}{R_{ab} cos\varphi}} \quad (2)$$

Where L_b is the spectral radiance of the bands 1 to 7; d is the relative earth-sun distance; φ is the solar zenith angle; R_{ab} is the atmospheric irradiance calculated for the bands 1 to 7 according to the Planck's law, integrating the radiation over the wavelength intervals and considering its fraction over the solar spectrum, assuming the sun as a blackbody (Teixeira, 2015).

The broadband planetary albedo (a_p) for was calculated by the weighted sum of the narrow-bands apb_b:

$$ap = \sum w_b ap_b \quad (3)$$

We used the following weight values (Table 2) calculated using the Plack law (Teixeira, 2010).

Table 2. Radiometric parameters for the Landsat 8 planetary albedo calculation: λ_b - bands wavelengths; R_{ab} -TOA mean solar irradiation; w_b – weight for each band.

L8 parameter	B1	B2	B3	B4	B5	B6	B7
λ_b(μm)	0.43-0.45	0.45-0.51	0.53-0.59	0.64-0.67	0.85-0.88	1.57-.165	2.11-2.29
R_{ab}(W m^{-2} μm^{-1})	1718.8	1810.4	1741.7	1558.3	962.5	206.3	68.8
w_b	0.10	0.31	0.30	0.13	0.08	0.05	0.04

Atmospheric correction was applied to obtain the instantaneous albedo (a_0) using regression equations calculated from satellite and field measurements in the Brazilian semiarid region (Teixeira, 2009; Teixeira, 2010; Teixeira, 2014).

$$a_0 = 0.6054 * ap + 0.079 \quad (4)$$

The Normalized Difference Vegetation Index (NDVI) is calculated as follows:

$$NDVI = \frac{ap_{(nir)} + ap_{(red)}}{ap_{(nir)} - ap_{(red)}} \quad (5)$$

The evaporative fraction was acquired at the satellite overpass time using the equation:

$$ET_{rf} = exp\left[a + b\left(\frac{T_0}{a_0 NDVI}\right)\right] \quad (6)$$

Where a and b are regression coefficients found to be 1.9 and -0.0008 for the reference semiarid area (TEIXEIRA, 2009).

The ET_0 was calculated by the Ref-ET for the EC towers and then interpolated using Inverse Weight Distance (IDW) algorithm. Then the daily ET was calculated for each pixel using the following equation:

$$\boldsymbol{ET = ET_{rf} ET_0} \quad (7)$$

1.2.3 Data processing

The SAFER model with Landsat 8 images was implemented in *ILWIS 3.4* (https://www.itc.nl/ilwis/download/). Then the outputs of the model were processed and analyzed with the EC footprints using *ArcGIS 10.8.* The process involved converting the MPR files to TIFF, clipping the aoi, using the raster calculator to multiply the ET_a pixels within the EC footprint and summarizing the results with the zonal statistics tool.

In this study we used 68 Landsat 8 images over 5 years to evaluate the SAFER algorithm performance. The dataset consists of cloud free images from April/2013 to September/2017 downloaded from NASA Earth Explorer website. The values were extracted using the Eddy Covariance footprint for each day.

Table 3. Satellite data over the period from August 2014 to September 2016. Day of Year (DOY)

Year	DOY
2013	115; 163; 170; 179; 186; 195; 202; 211; 218; 227; 234; 259; 266; 275
2014	134; 157; 166;173; 182; 198; 205; 214; 221; 230; 237; 253; 278
2015	121; 144; 169; 176; 192; 201; 208; 217; 224; 233; 249; 265

2016	108; 131; 140; 163; 172; 179; 188; 195; 204; 220; 236; 252; 259; 268;
2017	133; 142; 149; 165; 174; 181; 190; 197; 206; 213; 222; 229; 238; 245; 270

1.2.4 Eddy Covariance Footprint

The flux footprint model describes the area of influence of the turbulent flux measurements. The orientation and size of this area depend on the friction velocity (u_*), wind speed and direction, Obukov length, canopy, and EC tower measurements height (Kljun et al., 2015). The footprint represents a dynamic area where the pixels from the rasters generated by the model are extracted as a statistical sample of the energy flux components.

Some examples of the Flux Footprint Prediction (FFP) results calculated by the 2D flux model developed by Kljun et al. (2015) are presented in Figure 3. The ET and energy fluxes from SAFER were multiplied by the source area estimated by the footprint model, and then a sum of all pixels within the area was calculated using the spatial statistics tool of ArcGIS *10.8*. The value obtained was then divided by 0.9, representing 90% of the source area of the measured fluxes.

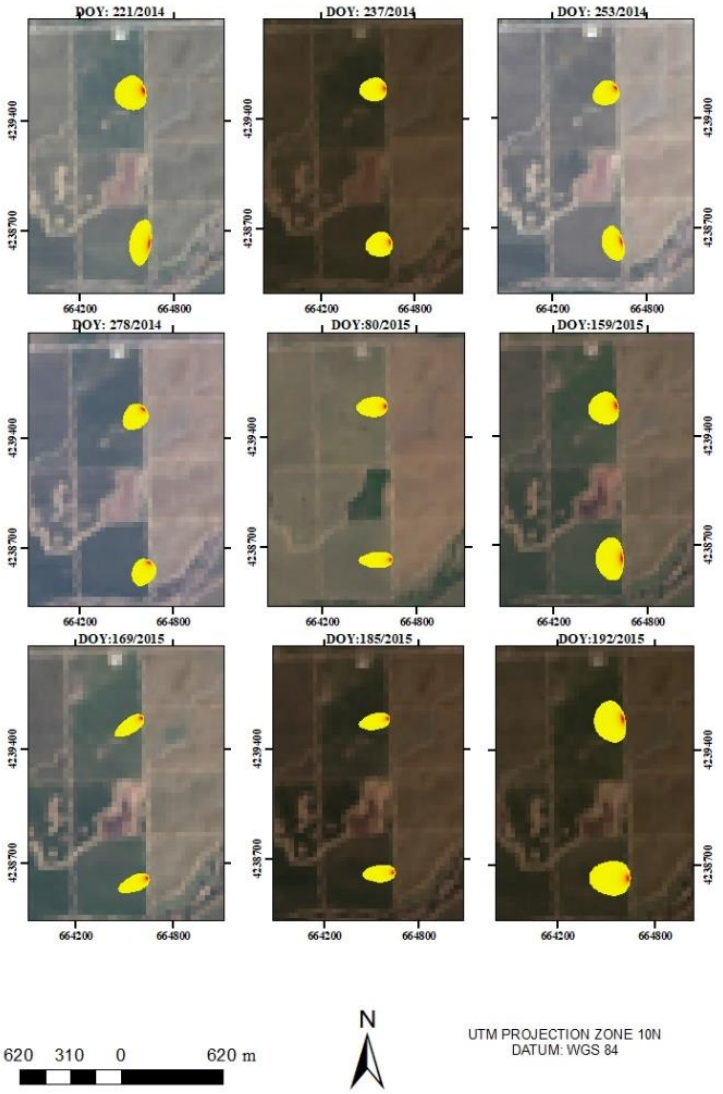

Figure 3. Flux footprint prediction for the two Eddy Covariance towers.

1.2.5 Statistics

To evaluate SAFER performance in the estimation of ET and surface fluxes, the values of Rn, LE, G and H from the EC were compared with the weighted sum of the pixel values within the calculated footprint for each DOY. The statistical metrics used in this study were the Root Mean Square Error (RMSE):

$$\boldsymbol{RMSE} = \sqrt{\frac{\mathbf{1}}{\boldsymbol{N}}\sum_{\boldsymbol{i=1}}^{\boldsymbol{N}}(\boldsymbol{y_i} - \boldsymbol{x_i})^{\mathbf{2}}} \quad (8)$$

The Mean Absolute Error (MAE):

$$\boldsymbol{MAE} = \frac{\mathbf{1}}{\boldsymbol{N}}\sum_{\boldsymbol{i=1}}^{\boldsymbol{n}}|\boldsymbol{y_i} - \boldsymbol{x_i}| \quad (9)$$

The Mean Absolute Percentage Error (MAPE):

$$\boldsymbol{MAPE} = \frac{\mathbf{1}}{\boldsymbol{N}}\sum_{\boldsymbol{i=1}}^{\boldsymbol{n}}\left|\frac{\boldsymbol{y_i} - \boldsymbol{x_i}}{\boldsymbol{x_i}}\right| * \mathbf{100} \quad (10)$$

and Nash-Sutcliffe efficiency coefficient (NSE):

$$\boldsymbol{NSE} = \mathbf{1} - \frac{\sum_{\boldsymbol{i=1}}^{\boldsymbol{n}}(\boldsymbol{y_i} - \boldsymbol{x_i})^{\mathbf{2}}}{\sum_{\boldsymbol{i=1}}^{\boldsymbol{n}}(\boldsymbol{y_i} - \bar{\boldsymbol{y}})^{\mathbf{2}}} \quad (11)$$

Where y_i is the observed values from the EC flux tower; x_i is simulated flux values obtained from SAFER using the footprint area; n is the number of observations and $\bar{y}$ is the average of the observed values.

1.3 RESULTS AND DISCUSSION

1.3.1 Satellite Measurements

The radiation balance depends on the surface albedo (α_0), NDVI and the surface temperature (T_0), which is variable among different vegetation types and spatially within the same crop type. The α_0 determines how much of the short-wave radiation is reflected into the atmosphere, thus the rest of the energy that will be available for the surface fluxes. NDVI is directly affected by the landcover and can be used to vegetation with different stages of maturation, bare soil areas and the presence of lakes and reservoirs. The longwave radiation emitted from the surface is directly proportional to

T_0 (Teixeira et al., 2015). Figure 4 presents the albedo values for the investigated period.

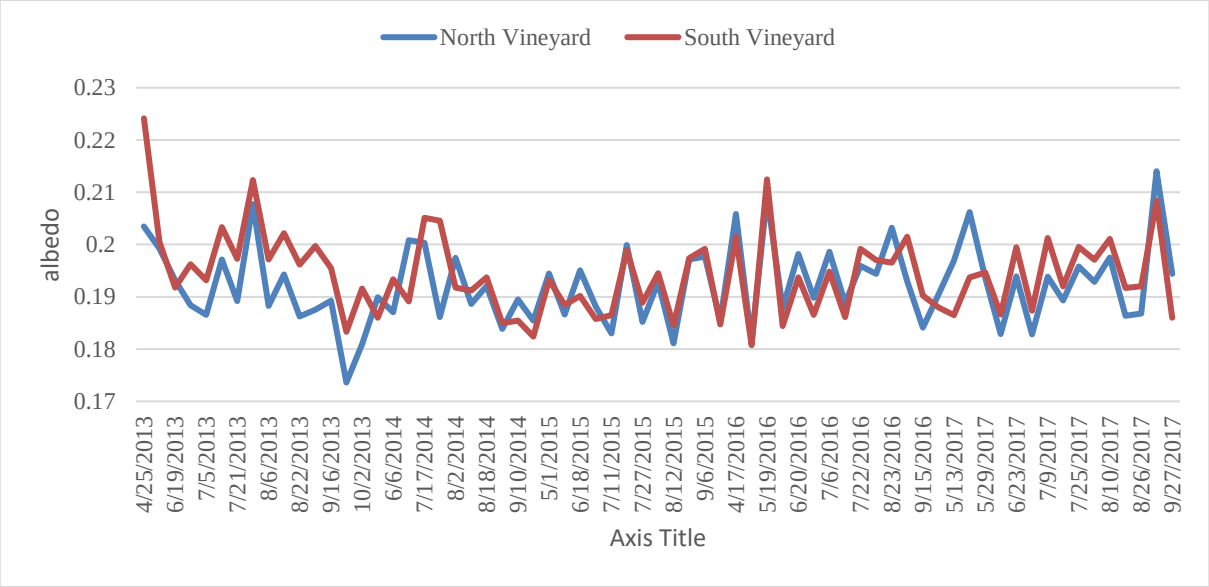

Figure 4. Surface albedo measurements from SAFER over the study period.

The estimated instantaneous α_0 varied from 0.17 to 0.22. In the 2013 to 2017 records the lowest values were observed at the start of the growing season between May and June. The high values at the start of the year (April) be associated with low soil cover and biomass in the vineyards. Both sites seem to have the same α_0 trend, although the South vineyard had the highest values associated with a younger crop. It is expected a decrease of the albedo as the Leaf Area Index increases or canopy biomass.

Figure 5 shows the correlation between surface albedo and the ET_a measured at the flux towers. The ET data is independent of the surface albedo, showing no correlation. This means that although this parameter is used as a multiplicative factor in equation 13, its impact is very weak in the regression, that is the reason why is combined with NDVI and LST. The surface albedo calculated by the SAFER model also did not have any correlation with the surface albedo calculated at the tower by the ratio of reflected and incoming solar radiation meaning that those regression coefficients found in previous studies in the Brazilian semiarid cannot be used in other areas (equation 6).

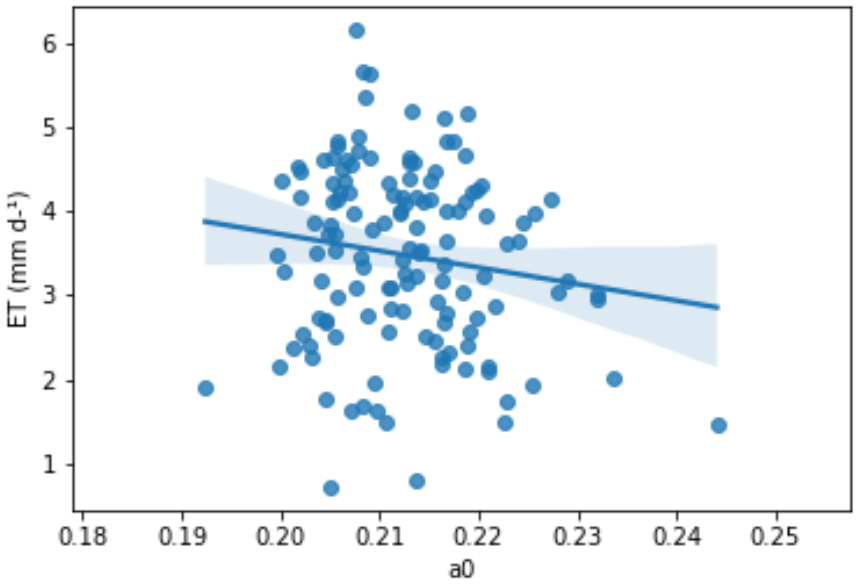

Figure 5. Correlation between Eddy Covariance ET and Surface albedo.

The NDVI values ranged from 0.37 to 0.76. The average was 0.57, with a standard deviation of 0.08. The lowest values were observed at the beginning and the end of the crop cycle, respectively, April and September. It is possible to see a trend in Figure 4 where values start to increase in June, when the crop is in full development and then decreases towards September for all analyzed years. The NDVI tendencies in both vineyards were pretty much the same, with slightly higher values in the North vineyard in the first 3 years. That is related to the maturity of the crops, as the South vineyard is the younger. Figure 6 presents the NDVI values observed throughout the seasons.

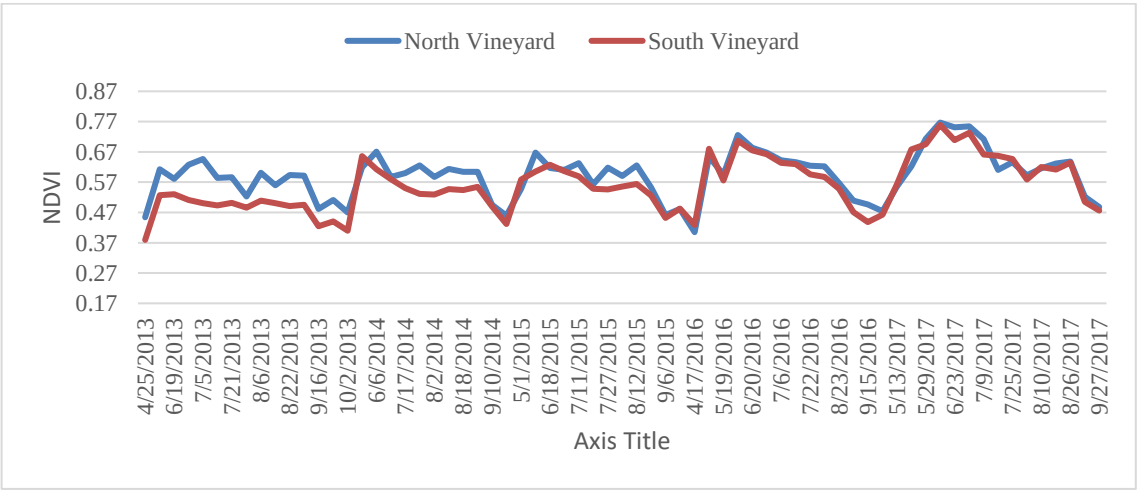

Figure 6. NDVI values over the study period.

As expected, the correlation between ET_a and NDVI has a positive trend, increasing ET_a as the NDVI gets higher (Figure 7). The data did not have a strong correlation; however, it seemed to be enough to represent ET_a. Healthy vegetation absorbs the red light in the chlorophyll pigments, and the leaves reflect the near-infrared radiation. When the plant is healthier and has enough soil moisture available the exchange between water vapor and CO_2 in the stomata while the photosynthesis increases. However, if the soil moisture is scarce, the evapotranspiration will be limited despite the NDVI.

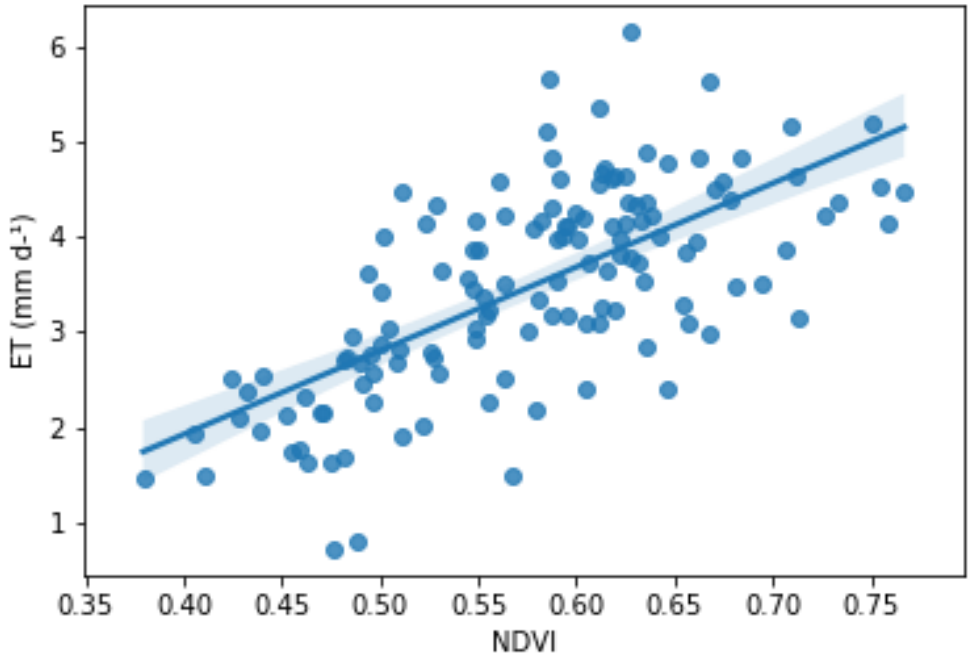

Figure 7. Correlation between actual evapotranspiration (ET) and the Normalized Daifference Vegetation Index (NDVI).

The LST values ranged from 301 to 322 °K. The average was 310 °K and the standard deviation 3.78 °K for both vineyards (Figure 6). The values in both vineyards were very similar, with the highest ones in the South vineyard in 2013 related to bare soil and low LAI. The lowest LST values were observed at the start and end of the growing seasons related to low incoming solar radiation values. During the fruit set stage, we can see variations in the order of 10 °K, probably related to irrigation

management. The peaks are associated with induced water stress to produce sugar on the grapes, and the cooler temperatures indicate days when the irrigation system was active, the variations of LST also relates to the crop cover levels. Figure 8 presents the observed values of LST in both vineyards.

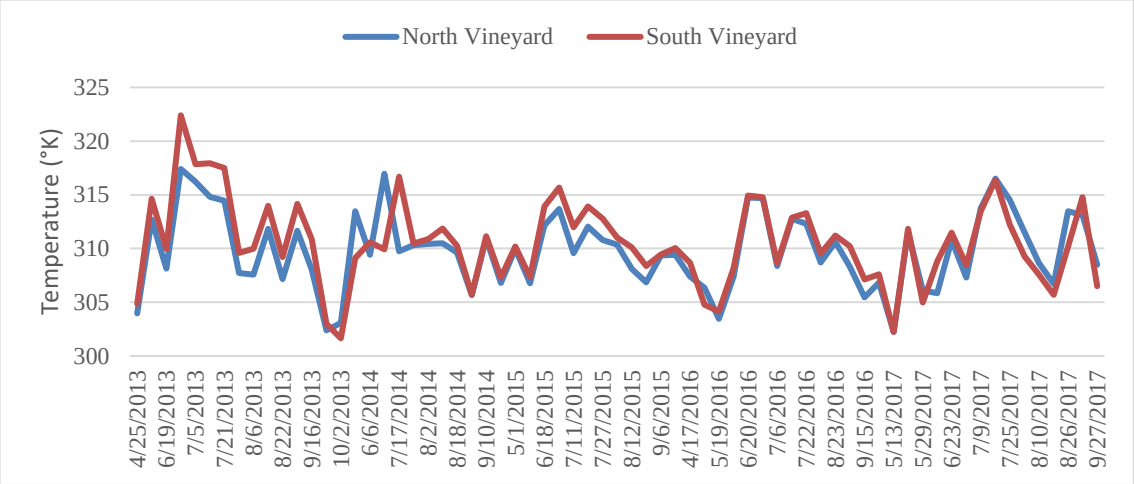

Figure 8. Surface temperature over the observed period.

In Figure 9, we can see the correlation between surface temperature and ET. The plot shows a different behavior than the expected, with a positive trend indicating higher ET in hot areas. Usually, cold areas are associated with high water content in the soil working as irrigation indicators. However, the effect of bare soil in the interrow must be considered as the pixel resolution of thermal images is low, causing a different relationship between the surface temperature data and ET_a.

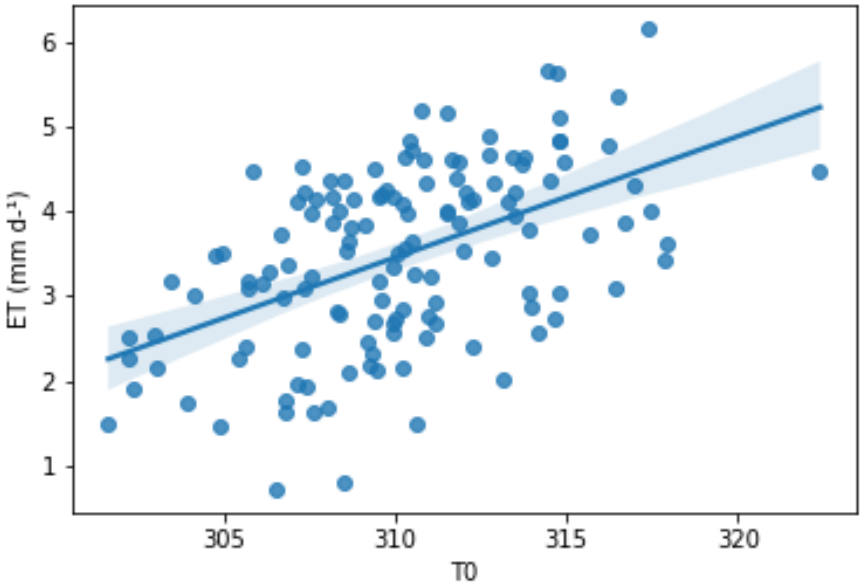

Figure 9. Correlation between ET and surface temperature.

The differences in a_0, NDVI and T_0 are mostly related to the incoming short-wave radiation and water availability variations and are also related to the crop phenological phase. In irrigated crops, where water availability is not a problem, those variations are usually related to irrigation uniformity, crop maturity, treatments, and fertilizer application.

1.3.2 ET estimation

Figure 10 shows the scatterplot of ET_a calculated by SAFER using the original regression coefficients and observed ET_a at the eddy covariance flux towers. The mean ET_a obtained for the period was 3.58 mm d^{-1} with a standard deviation of 1.41 mm d^{-1}. The highest value was 6.63 mm d^{-1} found in 2017 (DOY 165) and the lowest value 0.75 mm d^{-1} on 2015 (DOY 249). The highest ET_a error of 3.59 mm d^{-1} was observed in 2016 (DOY 140).

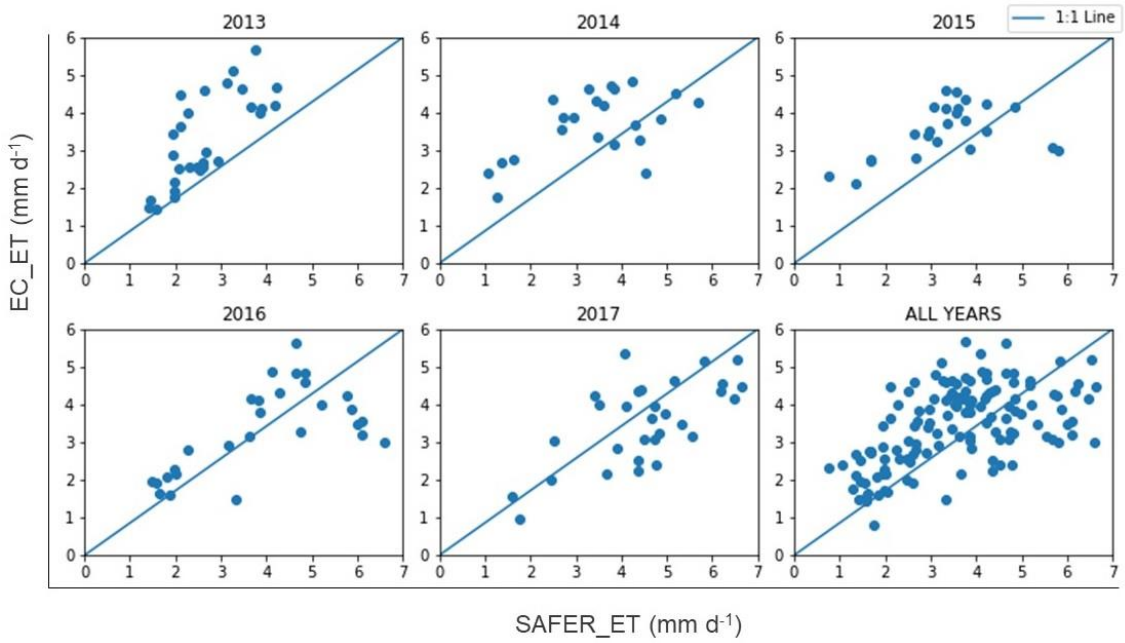

Figure 10. Scatterplot of observed vs estimated ET_a using original regression coefficients.

Goodness of fit statistics were estimated and are presented in Table 4. The model was performing very poorly with high RMSE errors for daily ET_a . The year of 2013 showed the best fit with RMSE of 1.08 mm d^{-1}, MAE of 0.8 mm d^{-1}, MAPE of 21%, R^2 of 0.59 and NSE of 0.24. The highest RMSE of 1.41 mm d^{-1} was observed in 2017, with also the highest MAE of 1.22 mm d^{-1} and MAPE of 43%. The year with the worst fit was 2015 with R^2 of 0.20 and NSE of -1.48. The months with the best performance was September, with a RMSE of 0.73 mm d^{-1}, and July, with a RMSE of 1.23 mm d^{-1}. On the other hand, the months with the worst performance were May and June, with RMSE values of 2.17 and 1.28 mm d^{-1}, respectively.

Table 4. Statistics between SAFER and EC evapotranspiration.

	RMSE (mm d^{-1})	MAE (mm d^{-1})	MAPE (%)	R^2	NSE
2013	1.08	0.8	21	0.59	0.24
2014	1.09	1.0	29	0.30	-0.66
2015	1.09	0.83	25	0.20	-1.48
2016	1.34	0.92	30	0.40	-0.42
2017	1.41	1.22	43	0.44	-0.48
All Years	1.22	0.96	30	0.28	-0.32

1.3.3 Calibration of a and b coefficients

Using the approach presented by Teixeira (2010) a linear regression was implemented to estimate the *a* and *b* parameters of equation 13 (Figure 11). The dependent variable LST/a_0*NDVI had a low correlation with the independent variable ln(ET/ET_0). This fact might be related to bare soil in the interrow of the vineyards. Landsat pixel resolution of 30 x 30 m in optical bands and 100 x 100 m in the thermal band mix canopy and soil, causing a noise in the reflectance value acquired by the sensor. Measurement errors in the EC system should also be considered as a cause for the low correlation between the satellite measurements (LST, a_0 and NDVI) and ground measurements (ET and ET_0)

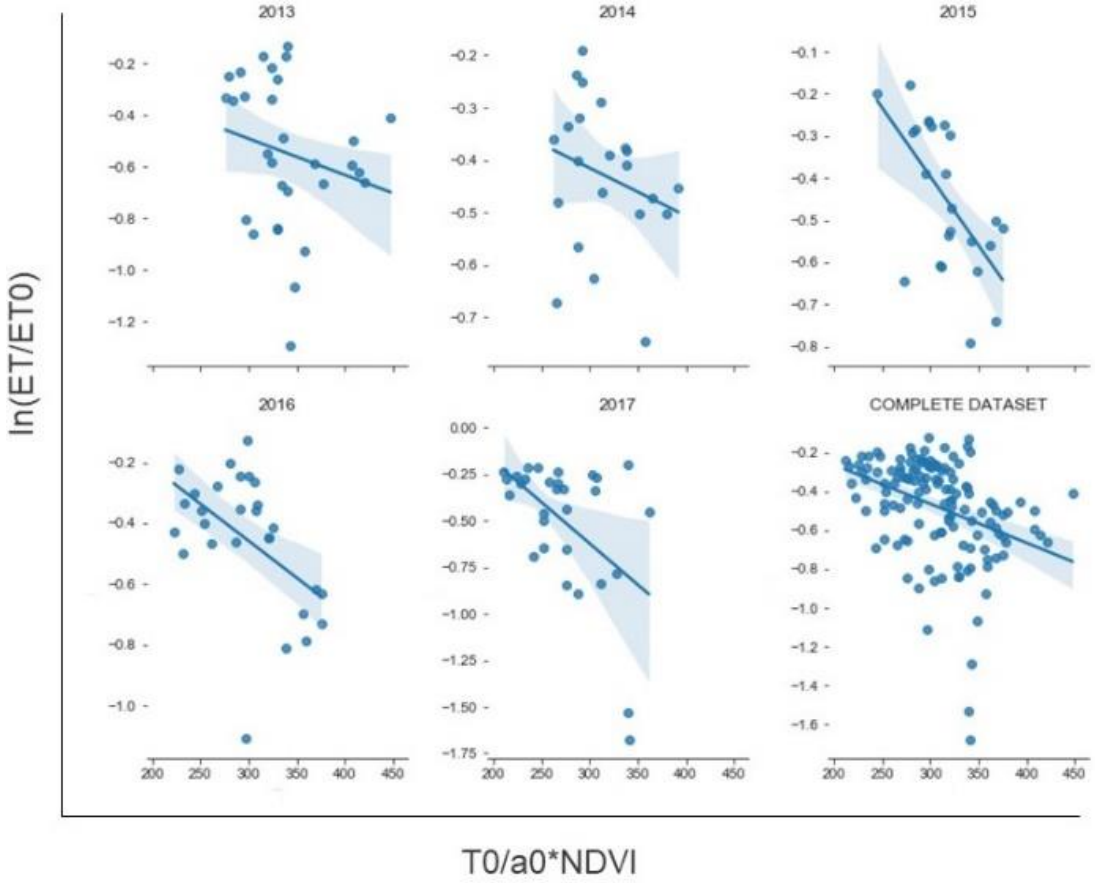

Figure 11. Calibration using satellite measurements and field data.

We tried this approach using the instantaneous and daily ET_a and ET_0 values for each year and using the whole dataset. The ET_0 values were calculated for the EC towers, while the recommend approach by Teixeira (2010) is to use

agrometeorological stations in the surroundings of the vineyards. Even though corrections were applied in order to calculate the wind speed at 2 m above ground level, this can be a source of errors because the wind resistance is different at different heights.

The daily ET/ET_0 showed stronger correlation with the satellite data. All the years had a negative trend as observed by Teixeira (2010); however, the R^2 was low, ranging from 0.01 to 0.2. Using the whole dataset, the total R^2 was 0.12. The coefficients found using the linear regression were 0.1382 and -0.002, a and b respectively.

Figure 12 represents the scatter plot of observed and estimated ET after the calibration. The data is closer to the curve showing a relatively good fit with the R^2 of 0.61 and NSE of 0.56. Carrasco-Benavides et al. (2012), reported an RMSE of 0.62 mm d^{-1} using METRIC over vineyards in Chile. After the calibration, in all the analyzed years the data is closer to the 1:1 line. That means that the model has a better agreement with the observed values after the calibration.

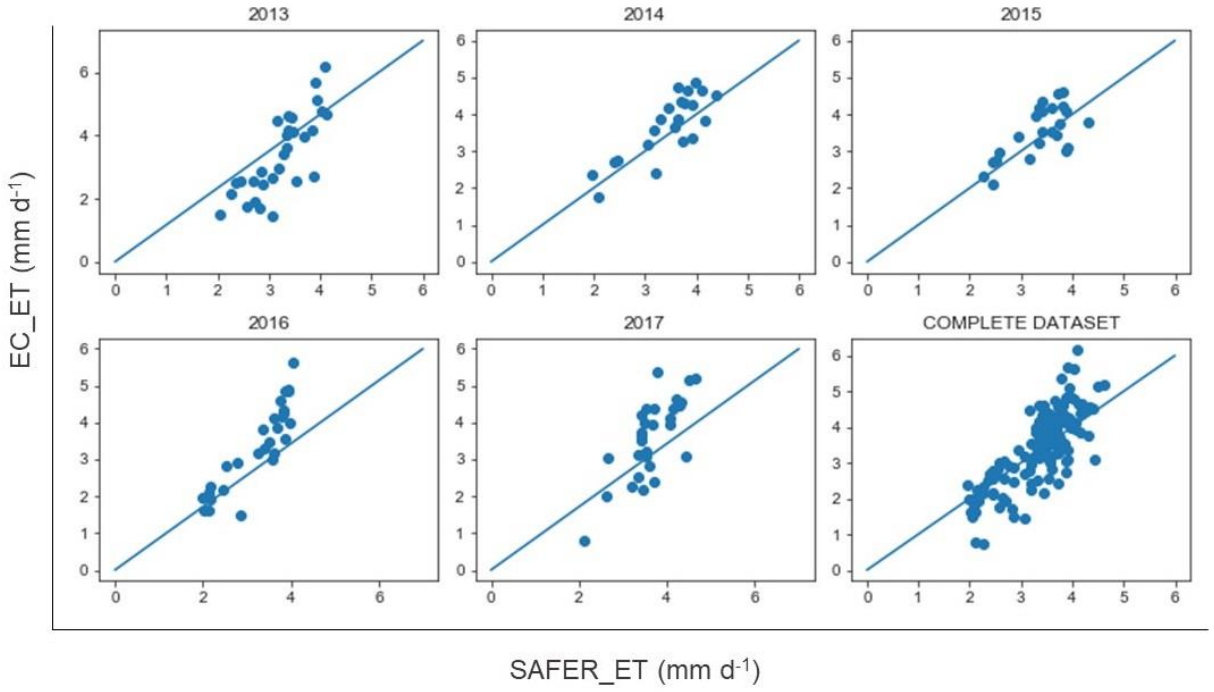

Figure 12. Modeled ET versus observed ET after calibration.

The RMSE of the whole dataset was 0.70 mm d^{-1} and the MAE 0.55 mm d^{-1}. The average estimated ET_a was 3.32 mm d^{-1} and the standard deviation of 0.63 mm d^{-1}. The maximum error in SAFER ET_a was 2.08 mm d^{-1} in the year of 2013 (DOY 28

JUN) when compared with the EC measurements. The RMSE is consistent with the previous results found on the same site. Semmens et al., (2016) using a multi sensor fusion approach, observed RMSE of 0.63 to 0.67 mm d^{-1} over the same vineyards. Knipper et al. (2019) found an RMSE of 0.76 on daily ET using Landsat images also over the same site. In this study, the highest RMSE of 0.89 mm d^{-1} was observed in 2013 while the lowest RMSE was 0.53 mm d^{-1} in 2015. A summary of all the statistics is presented in table 6

Table 6. Statistics of the SAFER model after a and b calibration.

	RMSE (mm d^{-1})	MAE (mm d^{-1})	MAPE (%)	R^2	NSE
2013	0.89	0.73	23	0.46	0.38
2014	0.54	0.47	13	0.63	0.49
2015	0.53	0.45	12	0.68	0.59
2016	0.59	0.44	14	0.80	0.71
2017	0.73	0.60	23	0.63	0.51
All Years	0.70	0.55	19	0.61	0.56

Sánchez (2019) found an RMSE of 0.6 mm d^{-1} comparing the results of STSEB with ad eddy covariance tower over vineyards in Spain. Venâncio et al., (2020) using SAFER over corn crops reported MAE values in the ET ranging from 0.34 mm d^{-1} to 0.68 mm d^{-1} after performing the calibration of a and b parameters. Considering that SAFER was applied to a full cover crop, their results are like those found in the current study. The year of 2013 presented the worst fit while 2015 had the best fit.

1.3.4 Seasonal Analysis

Time series of the estimated and observed daily ET_a after the calibration for the months of June, July, August, and September (2013-2017) are displayed in Fig. 13.

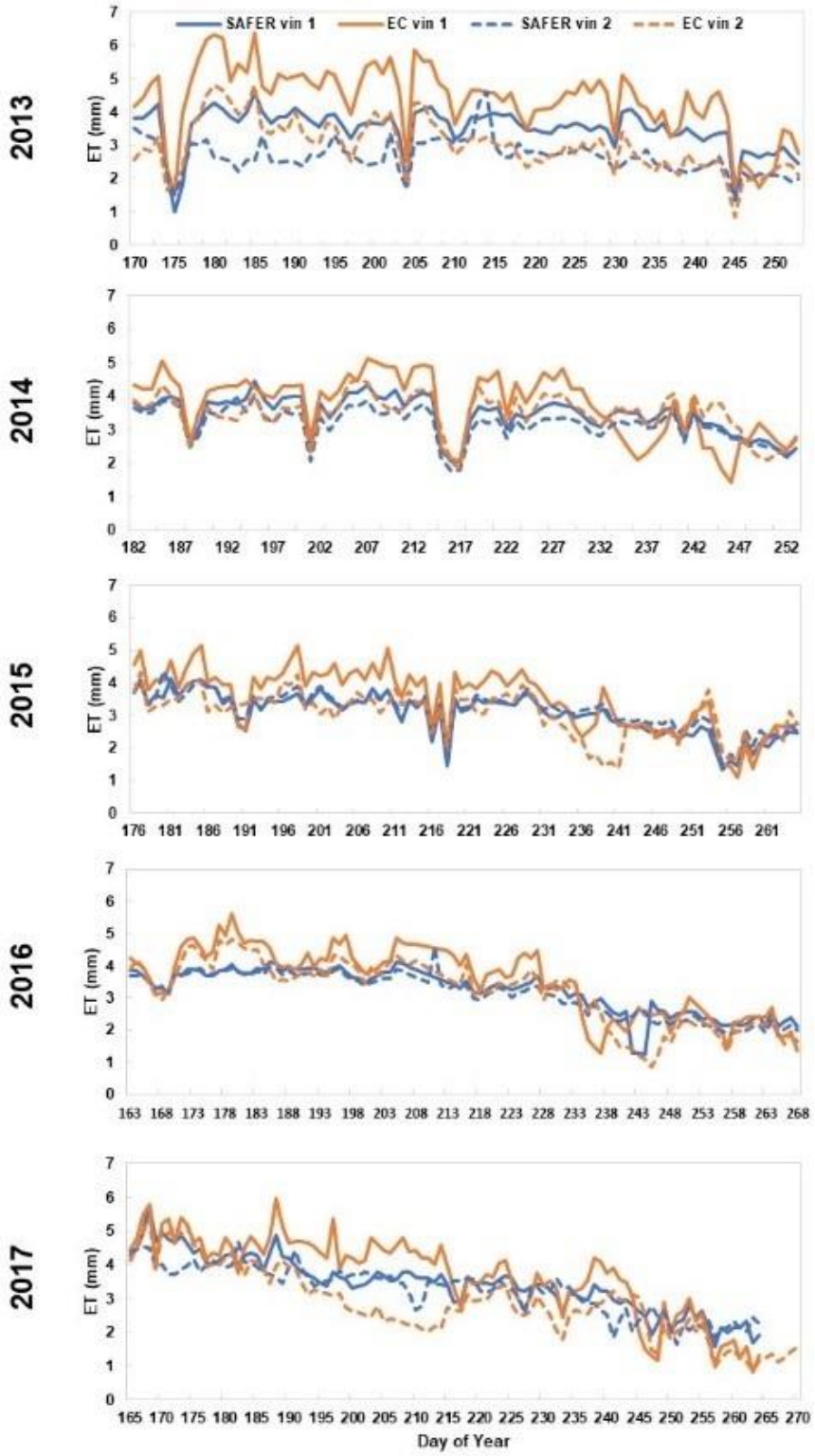

Figure 13. Time series of modeled ET_a from SAFER and observed ET_a from EC.

Daily values were extrapolated using a linear regression using the ET_0 and considering that the kc changed linearly between the images dates. The average

actual-to-reference ET ratio over the studied period for the North vineyard was 70%. For the South vineyard the average observed ET_a was 60% of reference ET. The area is within the overlap between two adjacent LANDSAT paths what contributed to an improvement for the temporal resolution as more images available during the analyzed period. Water consumption is underestimated by SAFER in the North Vineyard in every year based in comparison to the EC measurements. The worst performance is in 2013 with an error of 73.41 mm (20%) with the estimated average for that season being 3.49 mm while the observed average 4.36 mm for the crop season. The best performance was in 2014 where the estimated cumulative ET was 247.39 mm while the observed was 267.78, with an underestimation of 20.4 mm (8%). While the model was underestimating in the North Vineyard for the whole analyzed time series the model showed different results in the South Vineyard underestimating in 2013, 2014 and 2016 and overestimating in 2015 and 2017. The most accurate year was in 2016 when the estimated cumulative ET was 330.52 mm and the observed was 338.33 mm with an error of 2% (7.8 mm). Knipper et al., (2018) also found a discrepancy in the data during the late season of 2013 and 2015.

The estimated daily average ET_a for 2016 was 3.11 mm while the observed one was 3.19 mm. The water consumption is overestimated by 49 mm in 2017 (15%), the estimated average was 3.33 mm and the observed was 2.86 mm. The peaks in every year in the cumulative ET were higher in the North vineyard than the South vineyard, showing an agreement with seasonal pattern of the flux towers data.

According to Semmens et al., (2016) there is an early season bias in this area due to the presence of inter-row cover crop, which is completely senescence in DOY 160. This was the reason that we choose dates before the DOY 160 and the difference in the starting and ending dates for the years are related to missing data for the EC flux towers. It has also been reported that SAFER did not have a good performance in the early stages of the crop (Souza et al, 2020; Venâncio et al., 2020; Althoff et al., 2019)

The cumulative ET curves are shown in Fig. 14. Cumulative ET is underestimated in the North vineyard by 18 mm at DOY 247/2014 (8%) and underestimated by 76 mm (22 %) at DOY 247/2013, respectively the years with the best and worst performance. While in the South vineyard, Cumulative ET is

underestimated by 10.5 mm (4%) at DOY 247/2016 and overestimated by 33.1 mm (11%) at DOY 247/2017.

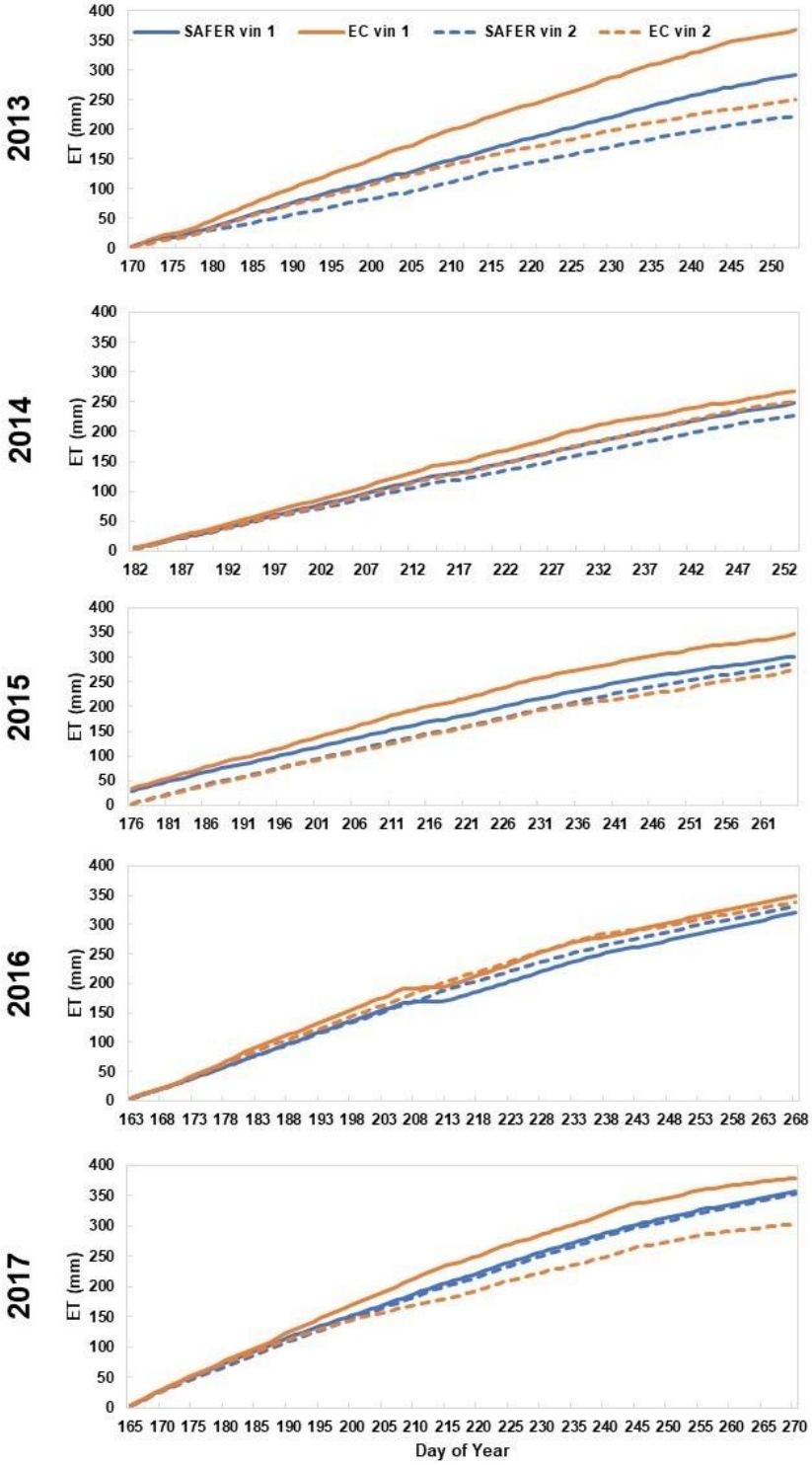

Figure 14. Cumulative curves of SAFER modeled ET and observed ET from EC.

Agreement between the model and flux towers improved from 2013 to 2017. The model underestimated ET in both vineyards with an exception for the years of 2015 and 2017 at the South vineyard. However, the curves followed the same pattern showing good agreements. The statistics of the estimated and observed the seasonal ET values are shown in the Table 7.

Table 7. Statistics of the seasonal ET over the analyzed vineyards.

	EC Accumulated	SAFER Accumulated	Residuals	R^2
2013_NV	366.82	293.41	73.41	0.71
2014_NV	267.78	247.38	20.40	0.66
2015_NV	346.08	301.50	44.58	0.87
2016_NV	348.07	319.67	28.40	0.97
2017_NV	379.09	356.90	22.19	0.86
2013_SV	274.61	250.58	24.02	0.29
2014_SV	343.99	327.25	16.73	0.57
2015_SV	273.06	286.07	13.00	0.49
2016_SV	338.33	330.52	07.81	0.82
2017_SV	303.98	353.62	49.63	0.75

In 2015 the amount of irrigation + precipitation at the North vineyard was 592.89 mm (Ohana-Levi et al, 2020). Unfortunately, we did not have access to the irrigation amounts in the south vineyard. The precipitation mainly occurred in early spring and irrigation occurs from May to September with the peaks late May and earlier September (Kustas et al., 2018a). The model presented a good performance because the estimated amount of cumulative ET is something in between half of the water applied trough the crop development.

1.3.5 Spatial variability of ET

Spatial patterns in ET over the vineyards and surrounding are shown in Figure 15.

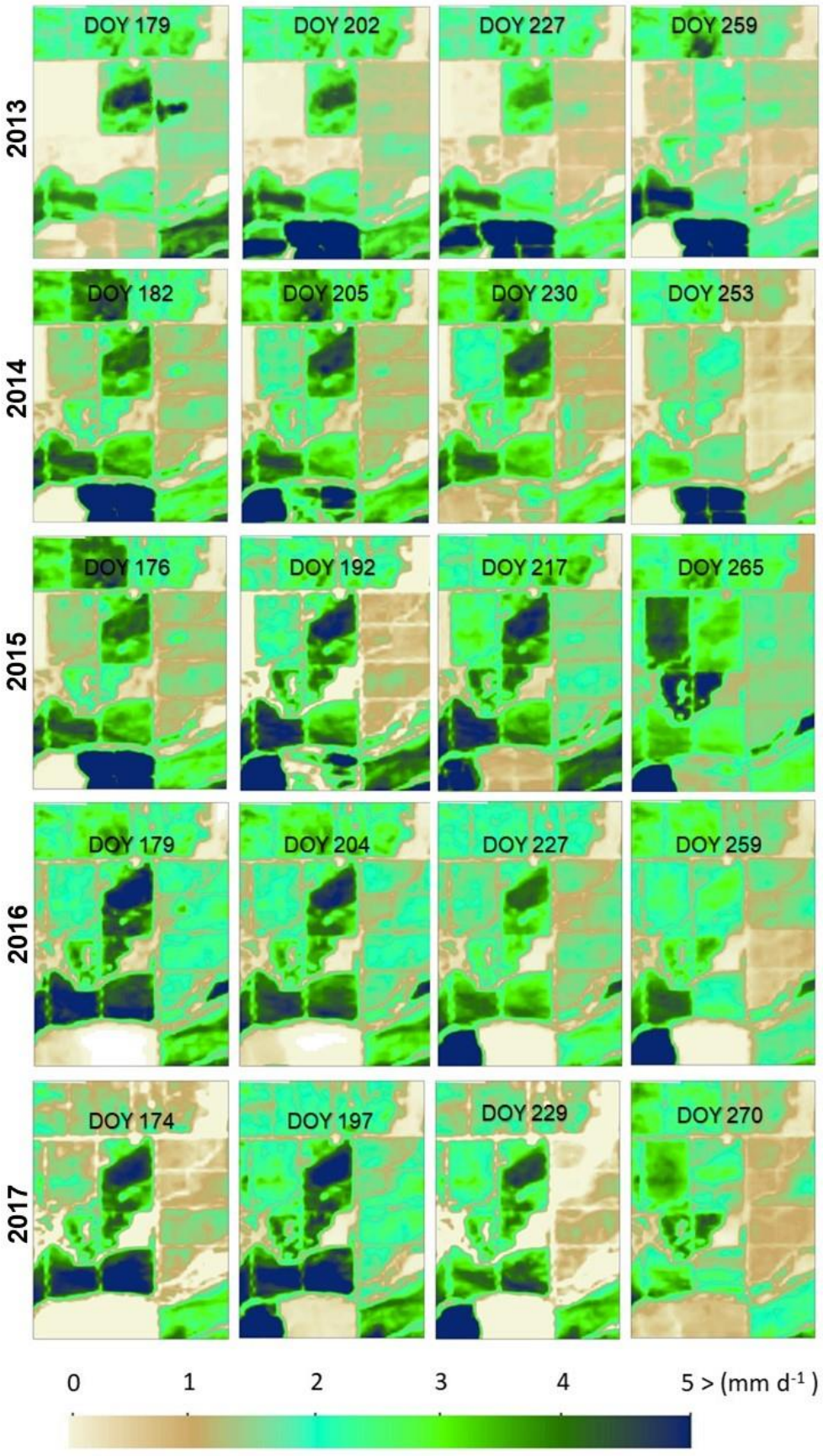

Figure 15. Spatial behavior of estimated ET over the analyzed period.

It is possible to observe how water consumption increases along the phenological phases. During the berry development stage (Mid-June) and the veraison (Mid-July, early-August), when the vines and fruit are fully and occur the highest values of ET_a . Daily water use reduces after DOY 250 as it gets closer to harvest (Mid-September). According with Knipper et al., (2019) the North vineyard exhibits a higher degree of ET_a spatial variability that increases during the growing season when compared to the south vineyard.

It's possible to observe a trend in the ET_a over the years. The North vineyard has a higher water consumption in the early years while the South vineyard has an opposite trend. That might be because the vineyards have maturity levels, resulting in different water demands. The south vineyard has a low ET_a in the early years and as the crop grows older the water use increases. The ET_a differences in the vineyards might be related to soil properties and irrigation practices. The management of the vineyards (timing and amount of irrigation, pruning activities) can vary between blocks and season (Kustas et al., 2018a)

In the south of the vineyards there are a four alfalfa fields which we can be identifid by higher values of ET_a. The alfalfa water requirements are higher than those for vineyards and changes in ET can be seen. In 2015 for instance, when the crops are fully developed in DOY 176 the ET_a is more than 5 mm d^{-1}, but in DOY 217 after the alfalfa was harvested the ET is close to 0 mm d^{-1}

The estimated ET_a by SAFER in 2015 along with pictures from the tower sites can be seen in Figures 16 and 17. The ET observed in the DOY 192/2015 (July 11th) is 4.14 mm at the North Vineyard and 3.52 mm d at the South Vineyard. The irrigation depth for that period is around 5 mm. The irrigation requirements were calculated using water leaf potentials and visual observation by the farm managers. Even the most uniform irrigation systems, like drip irrigation, have losses due to evaporation and percolation, so there is an agreement between the observed and estimated ET and the irrigation amount.

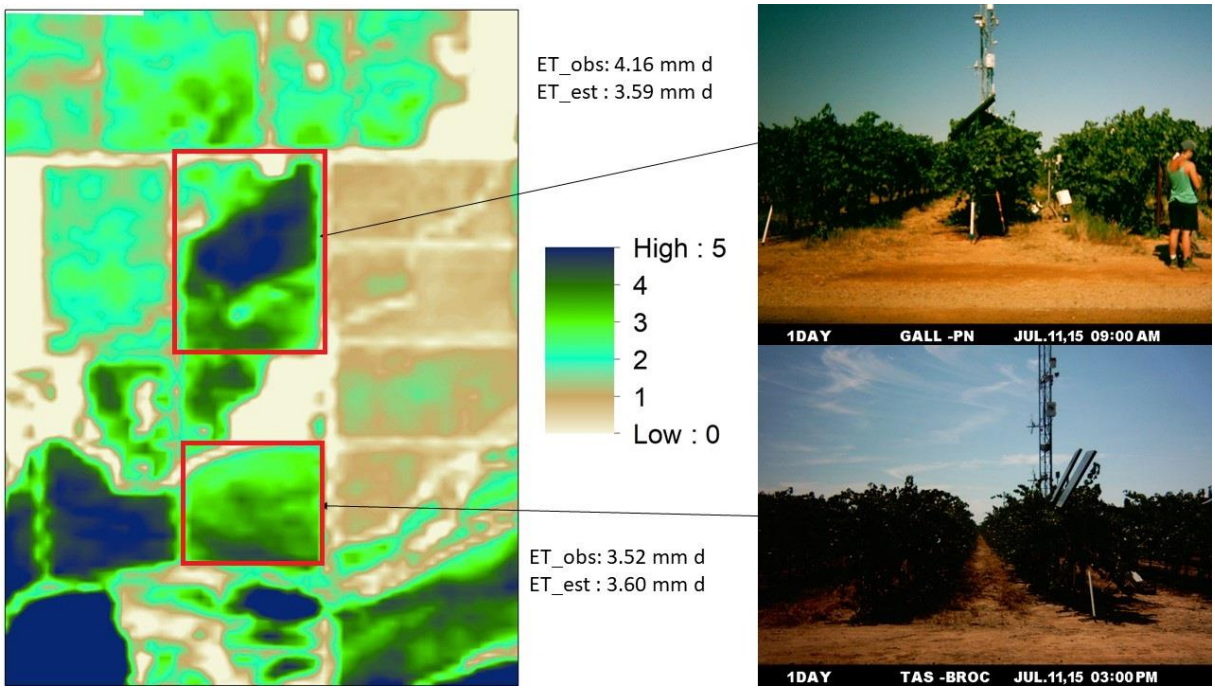

Figure 16. Estimated ET in the early season of 2015.

It is possible to see in the pictures that the vineyards have reached the full development and the canopy width reached a maximum covering. Typical vine canopy width is nominally 1 m midseason (Kustas et al, 2018a). After the harvest the crop reached senescence and there is only bare soil affecting the heat fluxes, with increase in sensible heat flux transfer and decrease in latent heat is required The bare soils reach higher temperatures in these conditions warming up the surrounding air, then the air transfers energy to the plants in the form of sensible heat flux increasing the ET rates when there is enough soil moisture available.

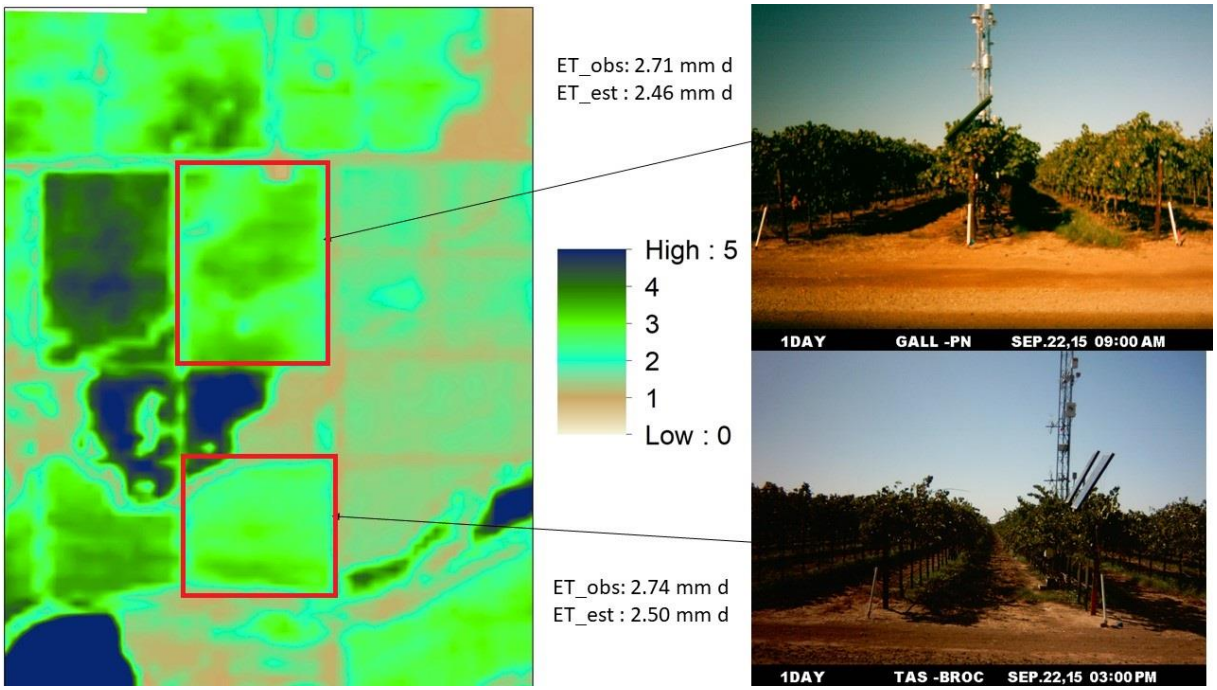

Figure 17. Estimated ET in the late season of 2015.

The plants reach the required sugar content by late August or early September and then they are harvested. It is possible to observe in the images that the canopy width decreased, and the color of the leaves changed to a yellowish tone. The observed ET_a rates decreased as well with values around 2.7 mm d^{-1} in both vineyards. Structural characteristics of the canopy can significantly influence the turbulent flow and exchange of heat and water vapor from the vineyard (Kustas, 2018b)

The pattern in irrigation follows the four main physiological stages (flowering, berry development, fruit set, and veraision). Budbreak of the vines occurs at mid-March/May and harvest in late August/early September when we can see the higher irrigation amounts (DOY 125 and 250). Unfortunately, Irrigation data are not available for 2013 and 2014. The irrigation inputs were lower in 2018 because there were more precipitation events while in the years of 2015 and 2016 the irrigation amounts were higher. For the North vineyard the total irrigation was 491.03 mm, 479.87 mm and 300 mm for 2015, 2016 and 2017 respectively.

Conclusions

The SAFER algorithm was tested in two commercial vineyards in California and showed a good performance on ET estimation despite that is not a full cover crop. Previous studies showed that SAFER had a bad performance on the first stages of the crops when the NDVI values are low. That source of error was attributed to the mixing information on the pixels caused by the bare soil

The original a and b values of the SAFER model showed not adequate for vineyards, with RMSE larger than 1.3 mm d^{-1} and a R^2 value of 0.28. This is an indicator that due to its ET_f estimation simplicity; the SAFER model needs to be calibrated with local ground information. It is also important to consider the errors inherent to using ET_0 values calculated from the EC towers as the algorithm normally uses data from surrounding agrometeorological stations.

After SAFER a and b calibration, the model was substantially improved. After the calibration the values showed more agreement with EC measurements with a R^2 of 0.61 and a NSE of 0.56. The RMSE after calibration was 0.70 mm d^{-1}. This result is very similar to the ones found in previous studies in the same area using different remote sensing energy balance models. Errors in the EC measurements must also be considered and a quality control of data should be employed to remove outliers or unrealistic values.

The season analysis indicated the SAFER follows the seasonal pattern of ET observed in the EC, however, the algorithm tends to underestimate ET. In the first analyzed years SAFER daily ET estimations presented a bias that decreased over the following years. The peaks of ET estimated by SAFER agreed with the ones registered by the EC. The highest residual in the cumulative ET was 73.41 mm and the lowest 7.81 mm.

The spatial variations were associated with the vineyards differences in age and maturity. It was possible identify the water consumption of the vineyards changing over time. The older vineyard had a higher ET in the first years and the younger in the last years.

The results showed in this study indicates that after performing a local calibration SAFER can be used for daily ET estimation. This is very promising because SAFER only requires the surface temperature, NDVI, surface albedo and ET0.

Furthermore, the model can also be applied without using the thermal band which will be explored in future analysis.

Acknowledgments
The Brazilian Ministry of Education supported this research through the CAPES PRINT process number 88887.467878/2019-00. The authors are very grateful to the Utah State University Water Research Laboratory and Alfonso Torres-Rua for welcoming the first author as a visiting scholar.

References

Alfieri, J.G., Kustas, W.P., Nieto, H., Prueger, J.H., Hipps, L.E., McKee, L.G., Gao, F., Los, S., 2019. Influence of wind direction on the surface roughness of vineyards. Irrig. Sci. 37, 375-388.

Allen, R.G., 2000a. REF-ET, Reference Evapotranspiration Calculator Version Windows 2.0. Univ of Idaho Res. And Ext. Center, Kimberly, ID, 82 p.

Allen, R.G., Hartogensis, O., de Bruin, H.A.R., 2000b. Long-Wave Radiation over Alfalfa During the RAPID Field Campaign in Southern Idaho. Research Report, Kimberly, Univ. of Idaho, ID.

Allen, R., G., Tasumi, M., Morse, A., Trezza, R. Wright, J.L, Bastiaanssen, W., Kramber, W., Lorite, I., Robision, C., 2007. Satellite-Based Energy Balance for Mapping Evapotranspiration with Internalized Calibration (METRIC)-Applications. Jour. of Irrig. and drain. engin. 133, 395-406.

Althoff, D., Alvino, F.C.G.; Filgueras, R.; Aleman, C.C., Cunha, F.F. 2019. Evapotranspiration for irrigated agriculture using orbital satelittes. Bioscience Journal, 35, 670-678.

Bastiaanssen, W.G.M., Menenti, M., Feddes, R.A., Holtslag, A.A.M., 1998. A remote sensing surface energy balance algorithm for land (SEBAL). 1. Formulation. Jour. of Hydro. 212, 198-212.

California grape Acreage Report, 2018 summary. https://www.nass.usda.gov/Statistics_by_State/California/Publications/Specialty_and_Other_Releases/Grapes/Acreage/2019/201904grpacSUMMARY2018Crop.pdf (acessed 18 May, 2020)

Cammalleri, C., Rallo, G., Agnese, C., Ciraolo, G., Minacapilli, M., Provenzano, G. Combined use of eddy covariance and sap flow techniques for partition of ET fluxes and water stress assessment in an irrigated olive orchard. Agri. Water Manag. 120, 89-97.

Carrasco-Benavides, M., Ortega-Fárias, S., Lagos, L.O., Kleissl, J., Morales, L., Poblete-Echeverría, C., Allen, R.G., 2012. Crop coefficients and actual evapotranspiration of a drip-irrigated Merlot vineyard using multispectral satellite images. Irrig. Sci. 30, 485-497.

Carrasco-Benavides, M., Ortega-Fárias, S., Lagos, L.O., Kleissl, J., Morales-Salinas, L., Kilic, A., 2014. Parameterization of the Satellite-Based Model (METRIC) for the Estimation of Instantaneous Surface Energy Balance Components over a Drip-Irrigated Vineyard. Remote Sens. 6, 11342-11371.

Coaguila, D., Hernandez, F.B.T., Teixeira, A.H. de C., 2017. Estacionalidade da evapotranspiração e produtividade da água na microbacia do córrego da mula em Santa Fé do Sul-SP. Rev. Bras. de Agr. Irr. 9, 232-238.

Crop evapotranspiration – Guidelines for computing crop water requirements – FAO Irrigation and drainage paper 56, 1998. http://www.fao.org/3/x0490e/x0490e00.htm (access 14 May 2020).

González-Dugo, M.P., Campos, I., Gonzalez-Piquerias, J., Andreu, A. 2012. Evapotranspiration monitoring in a vineyard using satellite-based thermal remote sensing. Proceedings of SPIE.

Hernandez, F.B.T., Neale, C. M. U., Teixeira, A.H.C, Taghvaeian, S., 2014. Determing large scale actual evapotranspiration using agrometeorological and remote sensing data in the northwest of São Paulo state, Brazil. Acta Hort. 1038, 263-270.

Holland, S., Heitman, J.L, Howard, A., Sauer, T.J., Giese, W., Ben-Gal, A., Agam, N., Kool, D., Havlin, J., 2013. Micro-Bowen ration system for measuring evapotranspiration in a vineyard interrow. Agr. and Forest Meteo. 177, 93-100.

Kljun, N., Calanca, P., Rotach, M.W, Schmid, H.P., 2015. A simple two-dimensional parameterisation for Flux Footprint Prediction (FTP). Geosci. Model Dev. 8, 3695-3713.

Knipper, K.R., Kustas, W.P., Anderson, M.C., Alfieri, J.G., Prueger, J.H., Hain, C.R., Gao, F., Yang, Y., McKee, L.G., Nieto, H., Hipps, L.E., Alsina, M.M, Sanchez, L., 2019.

Evapotranspiration estimates derived using thermal-based satellite remote sensing and data fusion for irrigation management in California vineyards. Irrig. Sci. 37, 431-449.

Kustas, W.P., Norman, J.M., 1997. A two-source approach for estimating turbulent fluxes using multiple angle thermal infrared observations. Water Resour. Res. 33, 1495–1508.

Kustas W., Anderson, M.C., Alfieri, J.G., Knipper, K., Torres-Rua, A., Parry, C. K., Nieto, H., Agam, N., White, W. A., Gao, F., 2018a. The Grape Remote Sensing Atmospheric Profile and Evapotranspiration Experiment. Bull. Amer. Meteor.Soc., 99, 1791-1812.

Kustas, W., Alfieri, J.G., Nieto, H., Wilson, T.G., Gao, F., Anderson, M.C. 2018b. Utility of the two-source energy balance (TSEB) model in vine and interrow flux partitioning over the growing season. Irrig Sci., 37, 375-388.

Li, S., Kang, S., Zhang, L., Li. F. Zhu, Z. Zhang, B., 2008. A comparison of three methods for determining vineyard evapotranspiration in the arid desert regions of northwest China. Hydrol. Process. 22, 4554-4564.

Lima, A. L.B., Filgueiras, R., Mantovani, E.C., Althoff, D., Santos, R.A., Venancio, L.P., 2019. Biophysical Parameters and Actual Evapotranspiration of Bean Culture by Means of Remote Sensing. Jour. of Agr. Sci. 11, 156-166.

López-Urrea, R., Montoro, A., Manas, F., López-Fuster, P., Fereres, E., 2012. Evapotranspiration and crop coefficients from lysimeter measurements of mature 'Tempranillo' wine grapes. Agr. Water Manag. 112, 13-20.

Madugundu, R. Al-Gaadi, K.A., Tola, E., Kayad, A.G., Hassaballa, A.A., Patil, V.C, 2017. Seasonal dynamics of surface energy fluxes over a center-pivot irrigated cropland in Saudi Arabia. Jou. of Envir. Biol. 38, 743-751.

Nassar, A., Torres-Rua, A., Kustas, W., Nieto, H., McKee, M., Hipps, L., Stevens, D., Alfieri, J., Pruger, J., Alsina, M.M., McKee, L., Coopmans, C., Sanchez, L., Dokoozlian, N, 2020. Influence of Model Grid Size on the Estimation of Surface Fluxes Using the Two Source Energy Balance Model and sUAS Imagery in Vineyards. Remote Sens. 12, 342.

Nieto, H., Kustas, W.P., Torres-Rúa, A., Alfieri, J.G., Gao, F., Anderson, M.C., White, W.A., Song, L., Alsina, M.D.M., Prueger, J.H. 2018. Evaluation of TSEB turbulent fluxes using diferent methods for the retrieval of soil and canopy component temperatures from UAV thermal and multispectral imagery. Irrig. Sci., 37, 389–406.

Norman, J.M., Kustas, W.P., Hume K.S., 1995. A two-source approach for estimating soil and vegetation energy fluxes from observations of directional radiometric surface temperature. Agric. For. Meteor, 77, 263– 293.

Ohana-Levi, N., Knipper, K., Kustas, W., P., Anderson, M., C., Netzer, Y., Gao, F., Alsina, M., M., Sanchez, L., A., Karnieli, A., 2020. Using Satelitte Thermal-Based

Evapotranspiration Time Series for Defining Management Zones and Spatial Association to Local Attributes in a Vineyard. Remote Sensing, 12, 2436.

Rana, G., Katerji, N., 2000. Measurement and estimation of actual evapotranspiration in the field under Mediterranean climate: a review: Europ. Jour. of Agron. 13, 125-153.

Santos, J.E.O. Cunha, F.F., Filgueiras, R. Silva, G.H, Teixeira, A.H de C., Silva, F.C.S., Sediyama, G.C., 2020. Perfomance of SAFER evapotranspiration using missing meteorological data. Agri. Wat. Manag. 233, 106076.

Sánchez, J. M., López-Urrea, R., Valentín, F., Caselles, V., Galve, J. M., 2019. Lysimeter assessment of the Simplified Two-Source Energy Balance model and eddy covariance system to estimate vineyard evapotranspiration. Agr. and For. Meteor. 274, 172-183.

Semmens, K. A., Anderson, M.C., Kustas, W.P., Gao, F., Alfieri, J.G., McKee, L., Prueger, J.H., Hain, C.R., Cammalleri, C., Yang, Y., Xia, T., Sanchez, L., Alsina, M.M., Vélez, M., 2016. Daily evapotranspiration over two California vineyards using Landsat 8 in a multi-sensor data fusion approach. Rem. Sens. of Env. Monitoring. 185, 155-170.

Silva, C.O.F, Manzione, R.L., Albuquerque Filho, J.L., 2018. Large-Scale Spatial Modeling of Crop Coefficient and Biomass Production in Agroecosystems in Southeast Brazil. Horticulturae, 4, 44.

Souza, J.M.F, Casaroli, J.A.J.D, Evangelista, A.W.P, Mesquista, M., 2020. Validação do modelo SAFER na estimativa da evapotranspiração da cana-de-açucar. Irriga, 25, 247-262.

Teixeira, A.H. de C., 2009. Water productivity assessments from field to large scale: a case study in the Brazilian semi-arid region. Lambert, Academic Publishing, p. 236.

Teixeira, A.H.C., 2010. Determining regional actual evapotranspiration of irrigated crops and natural vegetation in the São Francisco river basin (Brazil) using remote sensing and Penman-Monteith equation. Remote Sens. 2 (5), 1287-1319.

Teixeira, A.H.C., Hernandez, F.B.T., Lopes, H.L., Scherer-Warren, M., Bassoi, L.H., 2013. Modelagem espaço temporal dos componentes dos balanços de energia e de água no Semiárido brasileiro. Embrapa, Brasília.

Teixeira, A. H. de C., Hernandez, F.B.T., Andrade, R.G., Leivas, J.F., Bolfe, E.L., 2014. Energy balance with Landsat images in irrigated central pivots with corn crop in the São Paulo State, Brazil. Proceedings of SPIE, 9239.

Teixeira, A.H. de C., Leivas, J.F., Andrade, R.G., Hernandez, F.B.T., Franco, R.F., 2015. Modelling radiation and energy t with Landsat 8 images under different thermohydrological conditions in the Brazilian semi-arid region. In: Remote Sensing for Agriculture, Ecosystems, and Hydrology, 17. Toulouse. SPIE.

US Geological Survey, 2019. Landsat 8 Data Users Handbook. v. 5, Sioux Falls, SD.

Venancio, L.P., Mantovani, E.C., Amaral, C.H., Neale, C.M., Filgueiras, R., Gonçalves, I.Z., Cunha, F.F., 2020. Evapotranspiration mapping of commercial corn fields in Brazil using SAFER algorithm. Sci. Agric. 78.

Yunusa, I.A.M, Walker, R.R, Lu, P., 2004. Evapotranspiration components from energy balance sapflow and microlysimetry techniques for and irrigated vineyard in inland Australia. Agri. and Forest Meteo. 122, 93-107.

Zhang, B.Z., Kang, S.Z., Zhang, L., Du, T.S., E Li, S., Yang X.Y., 2007. Estimation of seasonal crop water consumption in a vineyard using Bowen ratio-energy balance method. Hydrol. Process. 21, 3635-3641.

CHAPTER 2[2]

PERFORMANCE OF SENTINEL-2 SAFER ET MODEL FOR DAILY AND SEASONAL ESTIMATION OF GRAPEVINE WATER CONSUMPTION

Anderson L. S. Safre[1]. Ayman Nassar[2]. Alfonso Torres-Rua. Mayhar Aboutalebi[3]. João C.C. Saad[1]. Rodrigo L. Manzione[4]. Antonio Heriberto de Castro Teixeira[5]. John H. Prueger[6]. Lynn G. McKee[7]. Joseph G. Alfieri[7]. Lawrence E. Hipps[8]. Hector Nieto[9]. William A. White[7]. Maria del Mar Alsina[3]. Luis Sanchez[3]. William P. Kustas[7]. Nick Dokoozlian[3]. Feng Gao[7]. Martha C. Anderson[7].

Anderson L. S. Safre

anderson.safre@unesp.br

[1]Department of Rural Engineering, Faculdade de Ciências Agrônomicas – UNESP, Botucatu, SP 18610-337, BR

[2]Department of Civil and Environmental Engineering, Utah State University, Logan, UT 84322, USA

[3]E & J Gallo Winery, Viticulture, Chemistry and Enology, Modesto, CA 95354, USA

[4]Department of Biosystems Engineering, Faculdade de Ciências e Engenharia – UNESP, Tupã, SP, 17602-496, BR

[5]Embrapa Monitoramento por Satélite, Campinas, SP, 13070-115, BR

[6]National Laboratory for Agriculture and the Environment, USDA ARS, Ames, IA 50011, USA

[7]Hydrology and Remote Sensing Laboratory, USDA ARS, Beltsville, MD 20705-2350, USA

[8]Plants, Soil and Climate Department, Utah State University, Logan, UT 84322-4820, USA

[9]COMPLUTIG, Alcalá de Henares, Madrid 28801, Spain

[2] Paper accepted in Irrigation Science Journal

Abstract

Assessment of water consumption is a crucial task for irrigation management in grapevines, especially in areas with limited water resources, which is the case for many vineyards in California Central Valley. This study evaluated the utility of the Simple Algorithm for Evapotranspiration Retrievement (SAFER) to estimate daily and seasonal actual evapotranspiration (ET_a) using Sentinel 2 images at 10-m spatial resolution and 5-day revisit time in 3 vineyards located at two sites in California. The energy balance is monitored with six eddy covariance (EC) flux towers as part of the Grape Remote-sensing Atmospheric Profile and Evapotranspiration eXperiment (GRAPEX). The estimated surface temperature derived from upwelling longwave radiation measurements was closely correlated with the observed surface temperature with R^2 higher than 0.86 for the analyzed EC towers. After performing an internal calibration, SAFER root-mean-square error (*RMSE*) values on daily ET_a were between 0.64 to 0.75 mm day^{-1}. Additionally, the seasonal ET_a was estimated and compared with the EC observations showing an average R^2 ranging from 0.64 to 0.52. Spatial patterns of ET_a showed variability differed between sites. The results indicate both limitations and potential utility of SAFER for irrigation management in vineyards using daily or seasonal ET_a under different irrigation treatments.

2.1 Introduction

The scarcity of water resources worldwide has become more prevalent due to rapid population growth in water-limited regions and the impact of climate change on the frequency and severity of drought. Irrigated agriculture plays a significant role in water use, using up to 70% of freshwater resources for the irrigation of 25% of the world crops (FAO, 2021). High-value crops, like vineyards, require special care for water use as the total water consumption is usually higher than the annual average precipitation in many places where the crops are grown (Medrano et al., 2015). This is the case of the irrigated vineyards in California, where the water resources are limited, and surface water cannot fulfill the demand throughout the year. Grape growers are becoming more dependent on groundwater extraction (Kustas et al. 2018), which is a limited supply as groundwater recharge is decreasing due to long-term drought, climate change, impermeabilization, and changes in land cover.

Better management of the water resources requires determining how much irrigation water is being applied. Growers can plan their irrigation based on crop water use requirements, depending on the crop type, phenology, and atmospheric demand. The actual evapotranspiration (ET_a) is the amount of water transferred from plants and soil to the atmosphere, and its value determines crop water use. ET_a can be used for irrigation account during the growing season as well as a tool for stress management in specific crops. The determination of ET_a in vineyards is important because growers need to regulate vine growth and induce a level of stress during grape development to achieve and berry quality targets (Santesteban and Royo 2006; Gago et al. 2017; Cataldo et al. 2021). The irrigation amount is also vital for achieving yield targets (Kliewer et al. 1983; Paranychianakis et al. 2004; Sanchez et al. 2017). The determination of ET_a allows growers to manage crop water stress and potentially attain a higher irrigation efficiency while maintaining yield targets. Some measurements methods for estimating ET_a include lysimeters, Bowen Ratio, Eddy Covariance (EC), and the soil water balance approaches using a network of soil moisture sensors.

The most precise method for water consumption estimation is using Lysimeters with an accuracy in the order of 0.05 mm (Howell et al. 1995). Traditional lysimeters were prone to various errors, which were overcome by weighable precision lysimeters. (Schrader et al. 2013). Mariano et al. (2015) showed that the ET_a determined by four weighting lysimeters in vineyards followed closely the variations of reference evapotranspiration (ET_0) validating the accuracy of these equipments. Libardi et al (2018) observed excellent accuracy and precision detection of equivalent mass variations around 0.1 mm of three lysimeters in vineyards. This method has been applied several times for ET_a estimation in vineyards (Trambouze et al. 1998; López-Urrea et al. 2012, Munitz et al. 2019). However, they are costly to install, maintain, and operate, which is why they are typically considered research tools (Moorhead et al., 2017). The Eddy Covariance (EC) method is based on high-frequency wind, temperature, and water vapor measurements for estimating the turbulent fluxes, sensible and latent heat, and EC application has been extensively validated against lysimeter measurements (Kustas et al. 2015; Sanchez et al., 2019). However, the technique suffers from a lack of energy balance closure and what to do with the extra available energy (Foken 2008). Soil water balance methods is a relatively simple method for estimating ET_a, but variability in soil properties, soil water content, drainage,

and runoff components can be challenging to determine accurately, and the measurements are only valid for a reduced area in the field (Wilson et al. 2001; Cai et al. 2009; Ukkola and Prentice 2013).

The Bowen-Ratio approach is another widely used method that assumes temperature and humidity gradients near the canopy surface are correlated to the turbulent fluxes having the same eddy diffusivity (Spittlehouse and Black 1980). Its accuracy has been validated with lysimeters (Prueger et al. 1997), but they are difficult to operate over taller canopies or when gradients are small, and the method is tenuous when the Bowen Ratio values approach -1 (Shi et al. 2008). The Surface Renewal (SR) method is another reliable method for ET estimation with relatively technical simplicity. The SR method is established on the turbulent exchange of sensible heat flux between plant canopy and atmosphere, which requires high-frequency air temperature measurements using a miniature temperature sensor, usually a thermocouple (Hu et al. 2018). Many studies compared the results of SR method with lysimeters indicating good agreement, with $R^2 > 0.9$ (Sanden et al. 2008; Castellví and Synder 2009; Moratiel et al. 2013)

Due to the limitations in the operational applications of ET_a measurement methods and the fact that they are limited in the spatial sampling of ET_a, FAO-56 is the most common method used for Evapotranspiration estimation by growers (Allen et al., 1998). It calculates ET_0 for grass under standard conditions, with enough soil moisture, nutrients, and no diseases based on agrometeorological data. The crop *evapotranspiration* (ET_c) is obtained by multiplying the ET_0 by the crop coefficient (K_c). The K_c is related to phenological properties and varies from crop to crop and growth stage. FAO-56 is a straightforward and accessible method but has some uncertainty due to the assumptions in the ET_0 equation and its sensitivity to temperature (Westerhoff 2015; Tablemorad et al. 2020). In addition, the implementation of generalized K_c values recommended by FAO-56 can lead to biases due to variations in climate and crop physiological characteristics (Knipper et al., 2019).

Thermal-based remote sensing models are a promising tool for ET_a estimation as they provide a means of determining ET_a and stress based on energy balance principles and crop canopy temperature. These models have the advantage of mapping ET_a at multiple resolutions spanning from field to watershed and regional scales, providing spatially distributed ET_a. They have been widely used for water

consumption estimation (Courault et al. 2005; Wood and McCabe 2006; Glenn et al. 2007; Kustas and Norman 2009; Zhang et al. 2016). Several remote sensing algorithms have been developed for mapping ET_a using satellite data. One of the more common approaches is contextually based, namely The Surface Energy Balance Algorithm for Land (SEBAL; Bastiaanssen et al. 1998) and Mapping EvapoTranspiration at high Resolution with Internalized Calibration model (METRIC; Allen et al. 2007). These algorithms calculate ET_a based on anchor pixels (hot and cold) that represent wet and dry soil moisture conditions, associated with well-watered conditions where ET_a is at the potential rate and zero ET_a respectively. The Two-Source Energy Balance (TSEB; Normal et al. 1995; Kustas et al. 1999) partitions the radiometric temperature and modeled evaporative fluxes between soil and canopy components, has provided acceptable accuracy for modeling ET_a in structured canopies such as vineyards (Knipper et al. 2020). TSEB has also been applied on UAV images showing high correlation with eddy covariance flux towers (Nieto et al., 2019a; Aboutalebi et al., 2020) The Atmosphere-Land Exchange Inverse ALEXI (Anderson et al. 1997, 2007) is based on TSEB coupling a time-differencing mode to map daily fluxes using geostationary satellites at continental scales. In addition, the DisALEXI algorithm disaggregates the fluxes to a finer scale using Thermal Infrared (TIR) imagery from polar-orbiting satellites (Anderson et al., 2010).

The Simple Algorithm for Evapotranspiration Retrievement (SAFER) was developed by Teixeira (2010) and was design to calculate ET_a as a function of the Land Surface Temperature (LST), NDVI, and surface albedo. The first version of the model uses a linear regression with Landsat TIR imagery to approximate LST. However, the second version (Teixeira et al. 2014b; Teixeira et al. 2015) uses the thermal radiation balance to estimate LST without the TIR images. SAFER estimates LST using the relation between total incoming radiation and air temperature measured by a meteorological station and net radiation, surface and atmosphere emissivity based on the albedo derived by optical images. This LST estimation is particularly interesting because the model can be applied using satellites like Sentinel-2, which provides images with a 10 m pixel resolution and five days revisit time, offering a higher resolution with a more frequent earth observation than models that uses Landsat data such as the ones embedded in Open ET project and the ECOSTRESS mission.

The Grape Remote sensing Atmospheric Profile and Evapotranspiration eXperiment (GRAPEX; Kustas et al. 2018) is a US Department of Agriculture project that started in 2013 collecting micrometeorological, biophysical, and soil moisture data for multi-scale Evapotranspiration mapping approach for vineyards. The goal of the project is to provide regional, operational irrigation management decision support. Several studies were conducted in order to apply remote sensing models such as ALEXI/DisALEXI (Semmens et al. 2016, Knipper et al. 2019) and TSEB (Kustas et al. 2019; Nieto et al., 2019b) and to refine and validate remote sensing retrieval algorithms of vine leaf area, biomass, phenology, radiation, and wind extinction, surface energy balance and ultimately ET_a estimation using ground-based biophysical and micrometeorological measurements of leaf and canopy level processes and ET_a measurements using EC flux towers. The GRAPEX project is contributing scientific and applied research for measuring and modeling vine physiological processes, energy fluxes, and ET_a that are advancing irrigation scheduling and water conservation efforts. Recently, Knipper et al (2019) provided weekly ET totals derived by an ET fusion model (DisALEXI + STARFM) to assist irrigation decision making during 2018 growing season in Ripperdan, demonstrating the potential for reducing water consumption in irrigated vineyards. However, the major limitation of this model for operational application was the latency in data availability (16-day revisit time) over the course of the growing season.

In this study, the performance of SAFER was evaluated using a 5-day period Sentinel-2B visible and near-infrared images along with agrometeorological data. The goal was to quantify the daily and seasonal *ETa* estimation in vineyards to monitor the ET dynamics during the 2018 growing season. The model was applied at two GRAPEX sites located in Sierra Loma and Ripperdan, California. The vineyards were managed with different irrigation levels, which was essential to assess SAFER sensitivity to soil moisture and stress conditions. The ET_a estimations were compared with six eddy covariance flux towers to validate the model.

2.2 Material and methods

2.2.1 Study area

The study was carried out over two sites in Central Valley, California. The field data in both vineyards was collected as part of the USDA-ARS Grape and Remote Sensing Atmospheric Profile and Evapotranspiration eXperiment (GRAPEX). Fig 1 shows the location of the two sites.

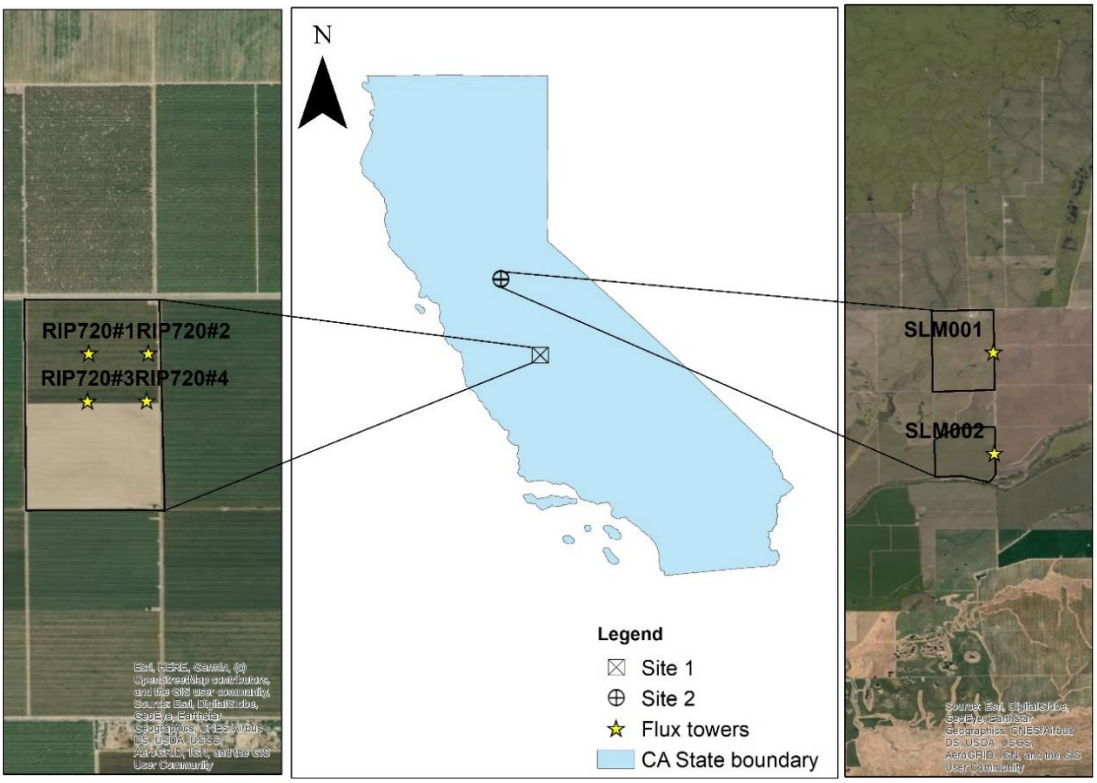

Fig. 1 The location of the study area. Site 1 is represented by the square with an x, and site two is represented by a circle with a cross. Yellow stars represent the Eddy Covariance tower locations within the vineyard. RIP = Ripperdan, SLM = Sierra Loma

The first site is a commercial vineyard located in Ripperdan, Madera County, with 16 ha with the Merlot variety planted in 2010. The trellis system consists of quadrilateral cordons on a horizontally split trellis. The spacing between vines is 1.5 m, and the spacing between rows is 3.5 m with an east-west row orientation. Most of the vineyard has similar soil type characterized as a sandy loam. The area is located in a Mediterranean climate with two very defined seasons: hot and dry summer and

rainy, mild winter. Most of the precipitation are concentrated in the winter. The late spring and summer months are often cloud-free with high evaporative demand. The vineyard is equipped with a Variable Rate Drip Irrigation (VRDI) system on a 30 x 30 m grid. The vineyard was divided into four subblocks, each monitored by four identical eddy covariance micrometeorological systems that started recording data in early May 2018. The flux towers were placed in the SE corner of each block in order to maximize fetch within the block, as the predominant winds are from the northwest (Knipper et al., 2019). The eddy covariance towers are equipped with an IRGASON water vapor and carbon dioxide sensor and a sonic anemometer (Campbell Scientific, Inc, Logan, Utah[3]) mounted 4 m above ground level (a.g.l.) collecting data at 20 Hz producing 30 min averages; an NR01 net radiometer mounted 4.35 m a.g.l.; five HFT3.1 soil heat flux plates at 8 cm depth; an EE08 temperature and a relative humidity sensor (Apogee) mounted 4m a.g.l. More details about the eddy covariance systems are described by Kustas et al. (2018).

The second site is located within Borden Ranch, near Sierra Loma, Sacramento County. It consists of two Pinot noir vineyards that differ in age and maturity, with the north vineyard being a 25-ha block and vines planted in 2009 while the south vineyard has an area of 21 ha and was planted in 2011. The vines are trained in a quadrilateral cordon trellis system with a 3.35 m spacing between rows and 1.52 between plants with an East-West row orientation. The soil type in the north vineyard is Loam/clay Loam, while the south vineyard has a Silt loam type of soil. The terrain on the north vineyard has less than 5% slope in the N-S direction, while the south vineyard is primarily flat because it is located near a creek flood plain. The climate is also Mediterranean, but temperatures and evaporative demand are not as high as at the Ripperdan site further south.

Figure 2 shows observed Temperature and ET0 values for the six flux towers at the two different sites. It is possible to identify the differenes in temperature throughout the season between the two sites. At site 1 the temperatures reached values higher than 30°C between July and August, while at site 2 the values were around 25°C. The ET0 was also discrepant between sites, with values ranging from 6-8 mm d^{-1} at site 1 and values ranging from 4-6 at site 2. This clearly demonstrates differences in

[3] Mention of trade names or commercial products in this publication is solely for the purpose of providing specific information and does not imply recommendation or endorsement by the U.S. Department of Agriculture.

atmospheric demand which is justified by the geographical location of the vineyards. Those differences are extremelly important in order to understand the limitations and potentials of the application of SAFER ET model. Therefore a wide range of climate areas represents a good validation approach for this algorithm.

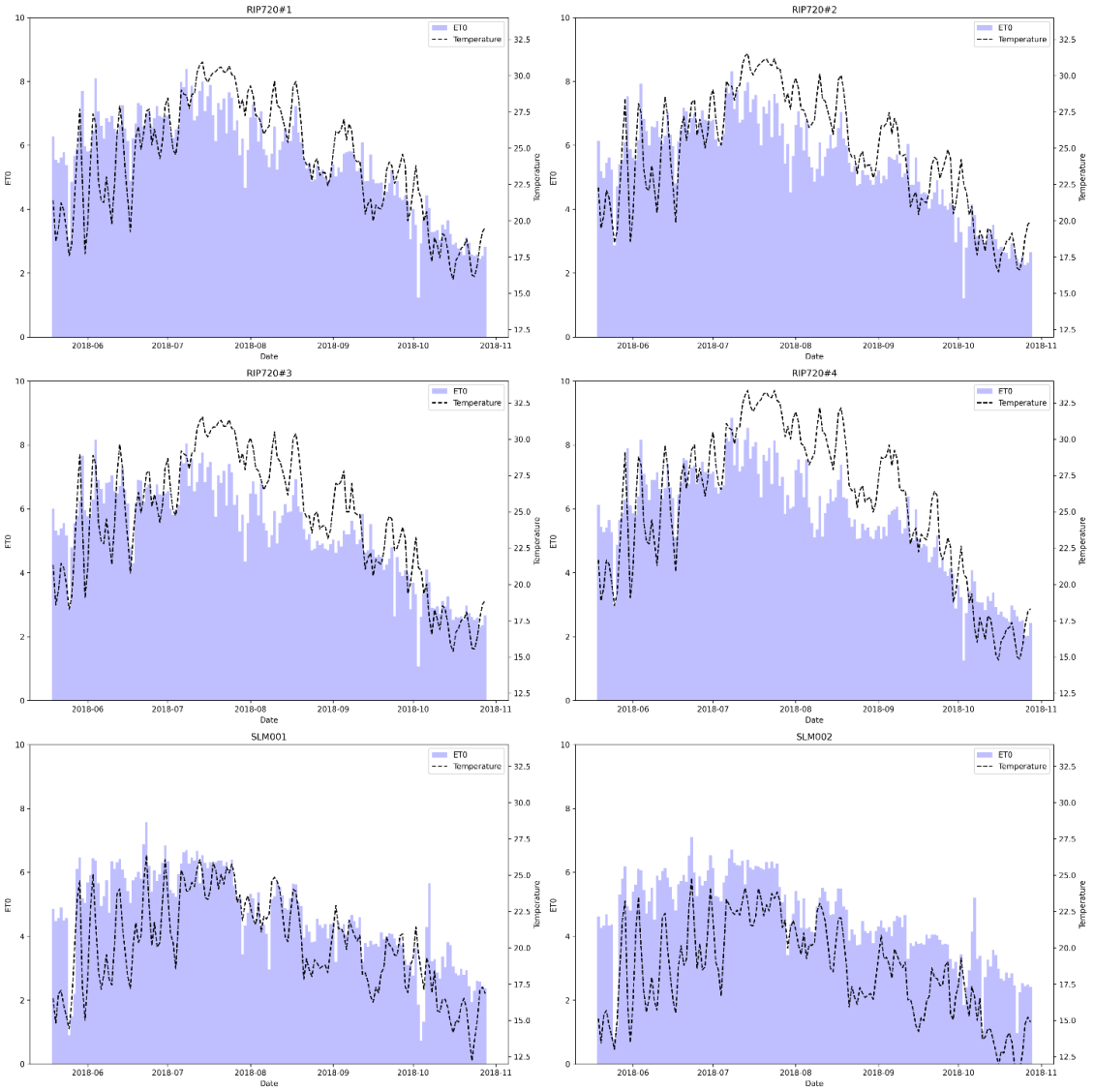

Fig. 2 Climatological information of the 6 flux towers during 2018 growing season.

Surface fluxes were measured using two eddy covariance towers during the growing season. The flux towers sensors consist of an EC150 water vapor and carbon dioxide sensor (Campbell Scientific) and a CSAT3 three-dimensional sonic anemometer mounted 5 m a.g.l. A CNR-1 four-way radiometer was measuring the net

radiation (Kipp and Zonen Inc). Five HFT-3 soil heat flux plates at a depth of 8 cm. A Gill shielded temperature sensor and an HMP45C Humidity probe measured the water vapor pressure at 5 m a.g.l. The measurements were collected at 20 Hz producing 15 min averages. More details on the eddy covariance data processing are available at Alfieri et al. (2019).

Table 1 presents the location of each flux tower and average temperature and ET0.

Table 1. Location, temperature and ET0 averages during the 2018 season of the flux towers in each vineyard.

Site	Vineyard ID	Latitude	Longitude	Mean Temperature	Mean ET0
Sierra Loma	SLM001	38.289	-121.118	20.27	4.58
Sierra Loma	SLM002	38.280	-121.118	18.41	4.66
Ripperdan	RIP720#1	36.849	-120.176	24.12	5.57
Ripperdan	RIP720#2	36.849	-120.174	24.67	5.38
Ripperdan	RIP720#3	36.847	-120.176	24.51	5.28
Ripperdan	RIP720#4	36.847	-120.174	25.48	5.64

2.2.2 Irrigation schedule and strategy

The site 1 was divided in four experimental blocks where different irrigation strategies were applied using the VRDI system. The irrigation system consists of emitters with a 1 L/h flow, 3 emitters per vine and a set 50.8 cm spacing between emitter. Figure 3 shows the design of the experimental areas. Blocks 1 and 2 were subject to a severe water stress. The irrigation was suspended during the early growing season until root zone depletion. There were visible and measurable signs of stress observed on vineyard, such as repressed shot tip growth, leaf water potentials below -1.5 MPa, and leaf senescence (Knipper et al. 2019). After the depletion of the root zone, the depth of water applied was approximately equal to the ET0. Irrigation on blocks 3 and 4 was conducted using measurements of leaf water potentials and visual inspection applying normal deficit irrigation. The irrigation depths on these

experimental treatments were calculated based on experience of resident vineyard managers, reproducing the commercial operation.

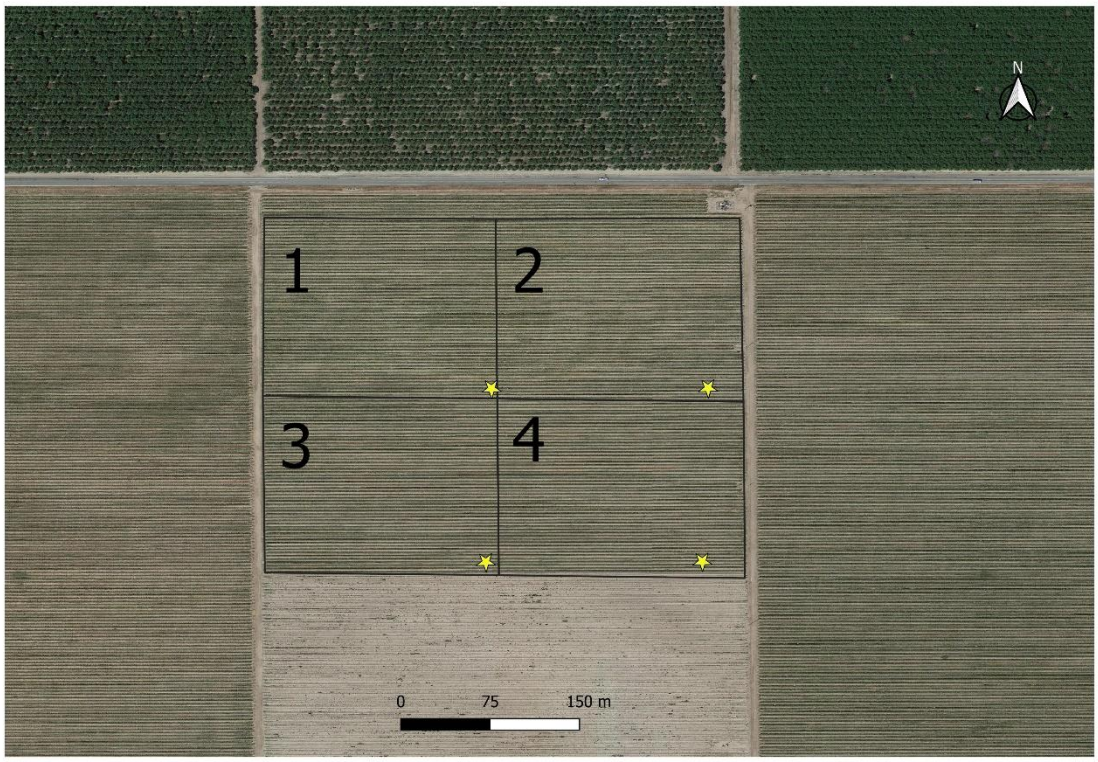

Fig. 3. Layout of the experimental blocks. Black boxes indicate the four study blocks at Site 1. Yellow stars represent the position of the flux towers.

Site 2 is equipped with a conventional drip irrigation system, with the irrigation concentrated at the center of each vine row. Two drip lines were installed parallel to row trellis at 0.3 m a.g.l. and two emitters between vines. The irrigation amount is more consistent between vines in comparison to the first site and the irrigation is scheduled to maintain soil moisture levels constant during the period of grapes development. Typically, occasional irrigation was applied during the bud break (early April and May) to maintain the good levels of the soil water content. Intensive irrigation (i.e, Irrigation interval of 1 to 2 days) starts in late June until the harvest (early September), small amounts of irrigation were applied after harvest to maintain vine canopies. The irrigation depth was calculated using visual inspections, leaf water potential measured with pressure chambers and soil moisture measurements.

2.2.3 SAFER Model description

SAFER is an algorithm for estimating e ET_a based on remote sensing and agrometeorological data such as the daily incoming solar radiation (R_G), the daily average air temperature (T_a), and the reference evapotranspiration (ET_0).

The planetary albedo for the whole solar spectrum (a_p) is calculated as the weighted (w_b) sum of each narrow-band reflectance (r_p) as shown in Equation 1 (Teixeira et al. 2014a):

$$a_p = \sum w_b r_p \tag{1}$$

where w_b is 0.32, 0.26, 0.25, and 0.17 for the blue, green, red, and near-infrared bands, respectively, the weights are calculated as the ratio of incoming shortwave radiation in a particular band and the sum of incoming radiation for all bands.

To calculate the daily surface albedo (a_0) the following equation was applied:

$$a_0 = a\, a_p + b \tag{2}$$

where *a* and *b* are regression coefficients found to be 1.70 and 0.13 for a 24-hour period (Teixeira et al. 2014a)

The daily Land Surface Temperature (*LST*) was estimated as a residual in the daily radiation balance (Teixeira et al. 2014b; Teixeira et al. 2015; Silva et al. 2019)

$$LST = \sqrt[4]{\frac{R_G - a_0 R_G + \varepsilon_A \sigma T_a^4 - R_n}{\varepsilon_s \sigma}} \tag{3}$$

where R_n is the daily net radiation; ε_a and ε_s are the atmospheric and surface emissivities, respectively; and σ is the Stefan-Boltzman constant (5.67 x 10^{-8} W m^{-2} K^{-4}).

The surface emissivity and atmospheric emissivity were calculated by Equation 4 and 5:

$$\varepsilon_a = a_A(-ln\tau_{sw})^{b_A} \tag{4}$$

$$\varepsilon_s = a_s lnNDVI + b_s \quad (5)$$

where τ_{sw} is the shortwave atmospheric transmissivity calculated as the ratio of R_G to the incident solar radiation at the top of the atmosphere (Teixeira et al. 2015), a_A, b_A, a_s and b_s are regression coefficients 0.9634, 0.1135, 1.0035, and 0.0589 (Teixeira 2010; Teixeira et al. 2014a) The regression coefficients in Equation 6 are between those obtained for Idaho (a_A= 0.85 and b_A = 0.09; (Allen et al. 2000a) and Egypt (a_A=1.08 and b_A= 0.26 (Bastiaanseen et al. 1998)

The net radiation (R_n) was calculated using the Slob equation (Teixeira et al. 2014a; Teixeira et al. 2014b):

$$R_n = (1 - a_0)R_G - a_L\tau_{sw} \quad (6)$$

The coefficient a_L can be found through its relation with T_a according to Equation 7:

$$a_L = cT_a - d \quad (7)$$

where *c* and *d* are regression coefficients found to be 6.99 and 39.93 (Teixeira et al. 2008; Teixeira et al. 2009), respectively.

The Normalized Difference Vegetation Index (NDVI) was calculated using Equation 8:

$$NDVI = \frac{r_{NIR} - r_{RED}}{r_{NIR} + r_{RED}} \quad (8)$$

where r_{NIR} represents the reflectance in the near-infrared wavelength and r_{RED} is the reflectance of the red wavelength.

To calculate the instantaneous evaporative fraction (ET_{fr}), i.e., the ratio of actual (ET_a) to reference (ET_0) the only inputs required are the *NDVI*, a_0, and T_0. The ET_{fr} was calculated according to the following equation (Teixeira, 2010):

$$ET_{fr} = \exp\left[a + b\left(\frac{LST}{a_0 NDVI}\right)\right] \quad (9)$$

where *a* and *b* are regression coefficients found to be 1.8 and -0.008 for the semi-arid conditions of the São Francisco basin, Brazil. These coefficients resulted from

comparison between field and remote sensing measurements of ET, ET0, a_0, T_0 and NDVI respectively (Teixeira et al. 2014b, Teixeira, 2010).

Although this equation looks quite similar to the crop coefficient (K_c), the FAO 56 document (Allen et al, 1998) states that this ratio can only be considered a Kc if the soil moisture conditions are optimal, among other conditions. This is the reason we chose to use the ET_r terminology.

The daily ET_a can be then calculated according to Equation 10:

$$ET_a = ET_{fr}\, ET_0 \tag{10}$$

where ET_0 is the reference ET, and its calculation is defined below.

2.2.4 Agrometeorological Data

The reference evapotranspiration was calculated for each tower using the Penman-Monteith equation (Equation 11) by the ref-ET software (Allen 2000b).

$$ET_0 = \frac{0.408\Delta(R_n - G) + \gamma \frac{900}{T+273} u_2 (e_S - e_a)}{\Delta + \gamma(1 + 0.34u_2)} \tag{11}$$

where ET_0 is the reference evapotranspiration (mm day^{-1}), R_n is the net radiation (MJ m^{-2} day^{-1}), G is the soil heat flux (MJ m^{-2} day^{-1}), u_2 is the wind speed at a height of 2m (m s^{-1}), e_s is the saturation vapor pressure and e_a is the actual vapor pressure (kPa), γ is the psychrometric constant and Δ is the slope of the saturation vapor pressure-air temperature curve (kPa °C^{-1}).

The total incoming radiation, mean air temperature measured at each flux tower, was used to compute ET_0 and then interpolated using the kriging method in ArcMap v.10.8 to obtain a raster file with the same pixel size and area to match Sentinel 2 imagery. In normal conditions, when there is no availability of flux tower measurements at the area of interest, the data is acquired from meteorological station networks and then interpolated to generate the ET_0, R_G, and T_a values. The size of the areas (really small scale) has no significant impact in the kriging result. Usually, ET algorithms are executed using single meteorological measurements for the whole area. The purpose

of using kriging in this study was to improve the spatial distribution of the meteorological data used as inputs for the model.

2.2.5 Remote Sensing data

Sentinel Level 1C Top of Atmosphere imagery was downloaded at the Copernicus Open Access Hub website (https://scihub.copernicus.eu/dhus/#/home). The Sen2Cor plugin (v.2.9) provided by the ESA website (https://step.esa.int/main/snap-supported-plugins/sen2cor/) was used to perform an atmospheric correction and obtain the Level 2A Bottom of Atmosphere reflectance images. Level 2A data were transformed from JPEG2000 to Geotiff format using *ArcMap v.10.8*. The model was run on *RStudio* using the Agriwater plugin (Silva et al. 2019). 47 Sentinel 2 Level 2A images from May to October 2018 (21 images for the Sierra Loma site, and 26 for the Ripperdan site) were used for this study.

Table 2 shows the Day of Year (DOY) of the Sentinel 2 images used in this study.

Table 2. DOY of Sentinel 2 images used for running SAFER

Site	DOY	Number of images
Sierra Loma	135, 155, 165, 170, 175, 180, 185, 198, 200, 205, 215, 225, 230, 235, 240, 245, 250, 260, 265, 270, 275.	21
Ripperdan	142, 147, 152, 157, 162, 167, 172, 177, 187, 192, 197, 202, 207, 212, 217, 222, 227, 232, 237, 242, 247, 252, 257, 262, 282.	26

2.2.6 Flux tower footprint

The flux tower footprint is a mathematical function that considers several micrometeorological factors, including the mean wind speed, wind direction, instrument

height, Monin-Obukov length, and friction velocity to calculate the atmospheric stability, which significantly affects the source area of the eddy covariance measurement. The hourly footprint was calculated for each coinciding Sentinel 2 overpass to obtain the source area used for comparison between the observed ET_a and the estimated ET_a. The flux tower footprint model developed by Kjlun et al. (2002) was used through Nassar's python code (Nassar et al., 2020). The resulting file is a raster with 3x3 m pixels for each flux tower, where each pixel receives a weight-related to its significance to the measurement. The weights were summed and divided by 0.90 that represents a 90% footprint area.

2.3 RESULTS AND DISCUSSION

2.3.1 LST Estimation

Figure 4 shows the scatter plot of daily estimated LST compared with the Radiometric Surface Temperature (RST) derived from upwelling longwave radiation measurements at the four eddy covariances systems installed at site 1.

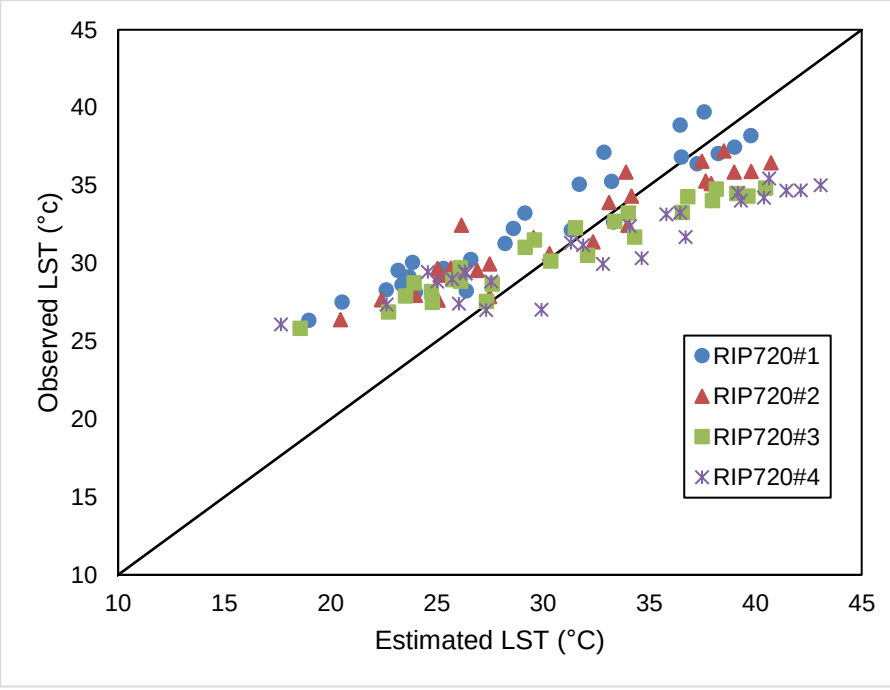

Fig 4. Scatterplot of modeled vs. observed 24-h LST over the 2018 growing season at site 1

The figure shows relatively very good agreement and a linear trend on daily LST estimation, which is confirmed by the $R^2 > 0.86$ for every tower. However, the model underestimates LST at towers 1 and 2. Flux towers 3 and 4 presented the most significant deviations at higher LST values, while tower 1 tends to deviate more at lower LST values.

Table 3 shows the statistical metrics of the agreement between estimated LST and observed RST in units of °C day^{-1}.

Table 3. Statistics metrics of SAFER LST estimation performance at the flux towers located Ripperdan.

	RMSE °C day^{-1}	MAE °C day^{-1}	MAPE °C day^{-1}	R^2 °C day^{-1}
RIP720#1	3.99	3.42	11	0.90
RIP720#2	3.25	2.78	08	0.88
RIP720#3	3.43	2.95	09	0.92
RIP720#4	4.50	3.89	12	0.86

The metrics include root mean square error (*RMSE*), coefficient of determination (R^2), mean average error (*MAE*), and mean absolute percentage error (*MAPE*). Daily RMSE values ranged from 3.99 to 3.25 °C day^{-1}. The results from SAFER showed smaller differences when compared to those from towers 2 and 3 with MAPE above 90%. This indicates a good performance of the algorithm forin estimating T_0 without thermal bands, as the observed trend in RST was modeled with good accuracy.

Figure 5 shows the residuals (estimated – modeled) on each EC tower over the growing season. The flux tower 4 was the one with the highest residuals, and the flux tower 2 presented the smallest, while the residuals varied from 8 to -8 C° day^{-1}. The residuals increased during the stress period (Mid July/Early August). The model tends to overestimate LST during the stress when the irrigation was suppressed. This pattern was confirmed by the increment in the residuals in every tower during this portion of the growing season.

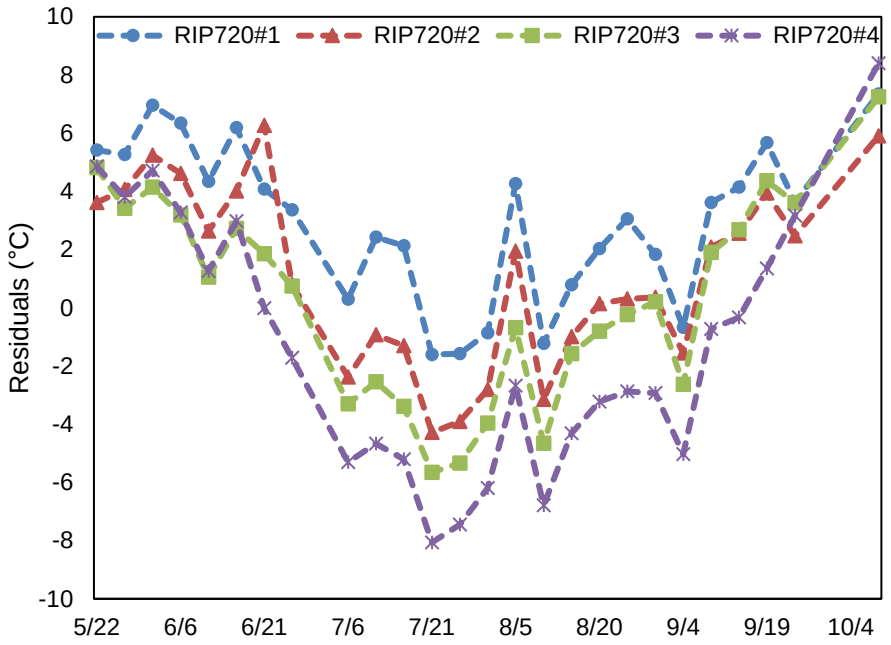

Fig. 5 LST residuals of estimated versus modeled surface temperature over the growing season at the four flux towers located at Ripperdan

Figure 6 presents the LST map simulated by SAFER for July 26th. The model followed the trend of observed RST for the day, representing the spatial variability of the LST. The warmest areas tend to be found at the roads where sensible heat fluxes are higher, while the coldest ones are within the irrigated blocks. The irrigation was completed shutdown on blocks 1 and 2 on July 10th and recommenced at July 23th. On July 26th the irrigation depth applied was 4.38, 4.36, 3.70 and 4.31 mm for blocks 1, 2, 3 and 4, respectively. There was not enough time for recovering soil moisture for optimum moisture conditions in the root zone for the blocks 1 and 2. The model underestimated LST at block 1 which was relatively warmer than block 2 even though the induced stress severity was the same for each block. There was a slight variation of observed T_0 between northern and southern blocks. At the southern blocks, where more water was available, thus cooler temperatures within the same range were observed, while at the northern blocks the temperature was almost 3°C higher. However, the model was only able to capture this pattern for blocks 2 and 3, overestimating LST at blocks 1 and 4 following the trend showed at Figure 4.

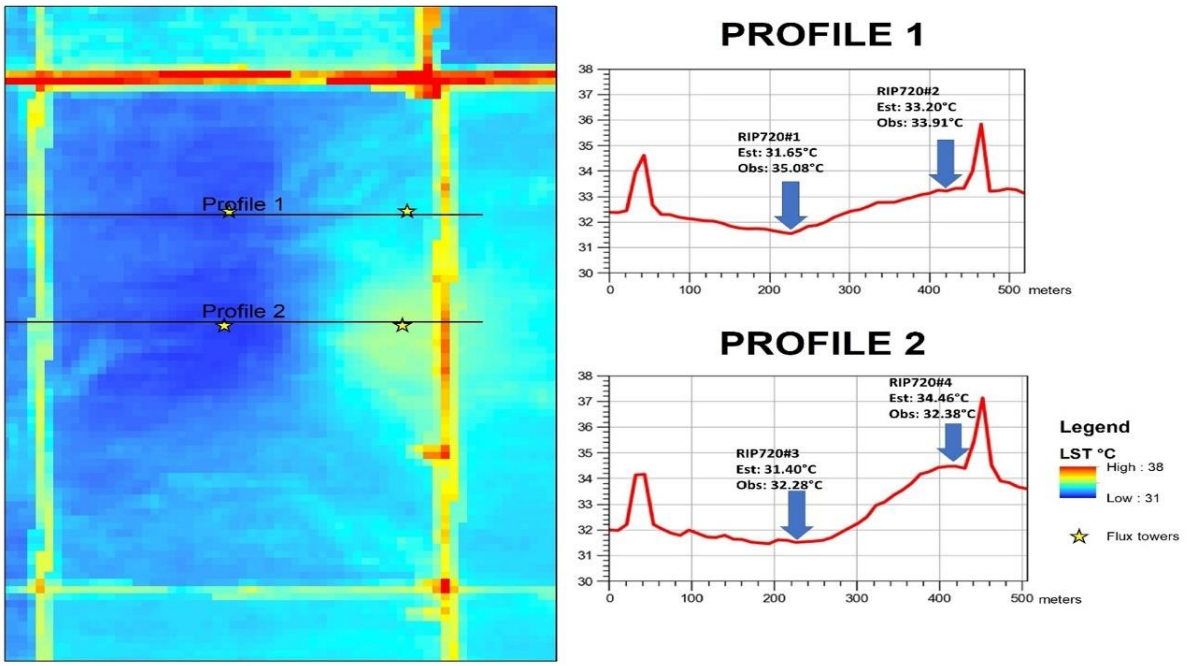

Fig. 6 Map of the LST over vineyards from Ripperdan at July 26th and surface temperature profile at Blocks 1 and 2 (upper panel) and Blocks 3 and 4 (lower panel) where the x axis represents the distance and the y axis the temperature in °C.

2.3.2 Model calibration and ET_a estimation performance

The SAFER model requires an internal calibration to find the optimal *a* and *b* coefficients of Equation 9, as reported by Teixeira 2010; Venâncio et al. 2020. In order to find those coefficients we need to find a linear equation that relates remote sensing parameters (LST/a_0*NDVI) with the ln(ET/ET_0) values observed for each flux tower at both sites. Analyzing three different vineyards (one at Ripperdan and two at Sierra Loma), different patterns were found at Ripperdan. Areas with higher water stress showed a negative correlation, which is the pattern looked for to calibrate the model. The reason might be because the model was developed and initially calibrated for Brazilian semi-arid conditions with areas that presented higher water stress.

We separated the data from the flux towers for calibration and validation. In the Ripperdan site we used the regression coefficients found with the combination of flux towers 1 and 2 (a = 0.55 and b = -0.0011). Nevertheless, at Sierra Loma the coefficients found at the tower installed at the northern vineyard was used to calibration due to its highest correlation and the regression coefficients were 0.066 and -0.0028

for a and b, respectively. These coefficients are drastically different from the ones (a=1.8 and b= -0.08) found by Teixeira (2010).

Figure 7 presents the scatter plots of estimated and observed ET_a with calibration and validation data. A significant improvement of the model results after calibration was observed, with data points more concentrated along the 1:1 line.

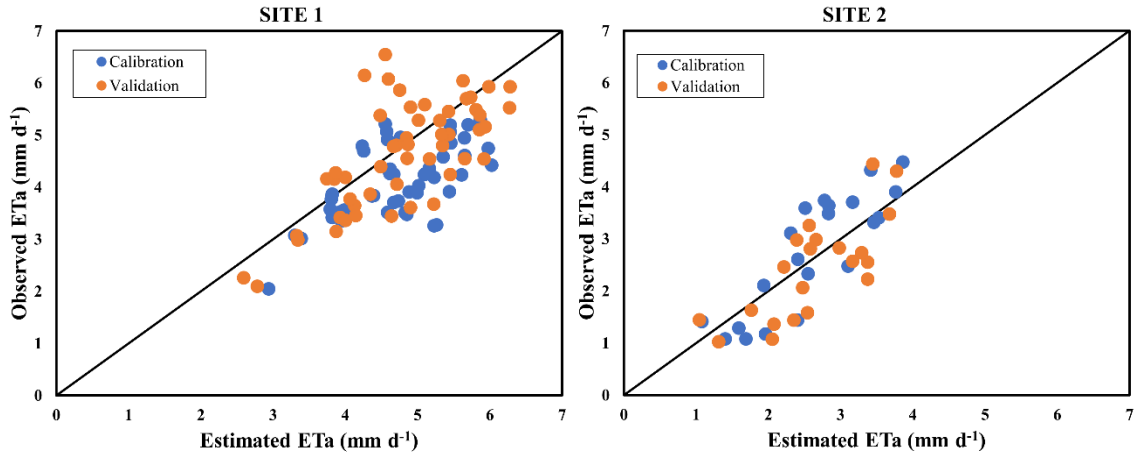

Fig. 7 Scatter plots of observed and modeled ET_a used for calibration and validation at Ripperdan (left panel) and Sierra Loma (right panels)

The statistics between estimated and observed ET_a are presented in Table 4. The model yielded satisfactory performance on the estimating ET_a without thermal bands after calibration. The daily *RMSE* values on validation data ranged from 0.64 to 0.75 mm day$^{-1,}$ while the *MAE* values ranged from 0.56 to 0.58 mm day^{-1}. An error of 0.80 mm d^{-1} is suggested by Seguin et al., (1999) as a target for irrigation purposes. The *MAPE* ranged from 13% to 28%. Semmens et al. (2016), using a multi-sensor fusion approach, observed *RMSE* of 0.63 to 0.67 mm day^{-1} over site 2, while Knipper et al. (2019) found an *RMSE* of 0.95 mm day^{-1} between the four blocks using Landsat images and the ALEXI-DisALEXI model with data fusion over site 1. The larger RMSE from Knipper et al. (2019) is due to the estimation of daily ET_a by interpolating between Landsat overpasses using the data fusion approach.

Table 4. Statistics metrics of ET_a estimates for the calibration and validation data at Ripperdan and Sierra Loma

SITE 1	**Statistics**	***ETa***	**SITE 1**	**Statistics**	***ETa***
	Mean Obs	4.06		Mean Obs	4.62
	Mean Est	4.68		Mean Est	4.8
Calibration	Mean Abs Res	0.72	Validation	Mean Abs Res	0.58
	RMSE	0.86		RMSE	0.75
	MAE	0.72		MAE	0.58
	R^2	0.46		R^2	0.44
	NSE	-0.42		NSE	0.45
	MAPE	18 %		MAPE	13 %
SITE 2	**Statistics**	***ETa***	**SITE 2**	**Statistics**	***ETa***
	Mean Obs	2.74		Mean Obs	2.43
	Mean Est	2.60		Mean Est	2.62
	Mean Abs Res	0.53		Mean Abs Res	0.56
Calibration	RMSE	0.62	Validation	RMSE	0.64
	MAE	0.53		MAE	0.56
	R^2	0.73		R^2	0.57
	NSE	0.68		NSE	0.53
	MAPE	23%		MAPE	28%

Higher residuals were found in July and August (>1.5 mm day^{-1}) at block 3 on site 1 as shown in Figure 8. These residuals followed the induced water stress. Between 10 and 23 of July, irrigation was totally suppressed at blocks 1 and 2. The model underestimated ET_a after this period at block 3. These higher residuals might be caused from the fact that the model was calibrated using data from flux towers 1 and 2, who were subject to the depletion of soil root zone. Also, when irrigation recommenced, on July 23th the depth of water applied was 2.94 mm d^{-1} and then at August 7th the irrigation depths at blocks 1 and 2 were up to 5 mm d^{-1}. Though, these residuals only occurred in two days and only at block 3 while during the remaining

dates the absolute residuals had an average of 0.5 mm. Residuals on block 4 did not reached to values higher than 1 mm day^{-1} .

Residuals at site 2 did not reached to values higher than 1.0 mm d^{-1} with the distribution of errors concentrated between 0.5 and 1.0mm d^{-1} and the variation of the residuals was not correlated to the water depths since site 2 used the conventional practices for management of the water stress period in grapes. This demonstrates a high accuracy of SAFER results and the potential of using this model as a tool for irrigation management since the residuals were in average below 1.0 mm.

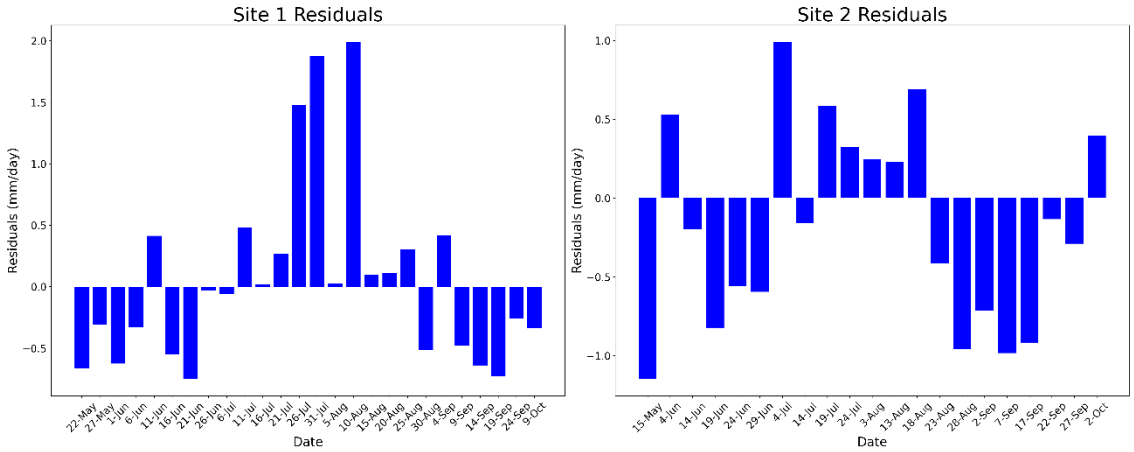

Fig. 8 SAFER residuals on validation data, block 3 on site 1 (left panel), and southern vineyard on site 2 (right panel) during 2018 growing season.

Figure 9 shows the ET simulated values and the irrigation depths at the four blocks on site 1. Since the vine at site 1 is more homogenous in soil and terrain conditions the model was not able to identify differences of irrigation amounts between blocks. This also might be due to a generalization of canopy and soil transpiration, indicating that a finer spatial resolution is needed to identify differences in daily ET between blocks. However, ET trend simulated by the model responded very well to water inputs, as seen by the decreasing trend after early July when the water was suppressed, and the peaks observed before August 14th when the irrigation recommenced.

Figure 9 also clearly shows the reason the model underestimated ET at block 3 after the water stress period. The residuals were caused because the model was calibrated using the data from blocks 1 and 2 and thus followed the ET trend of those blocks, represented by a decline in ET after July 10th and an increase in ET after July

24th. Block 3 was receiving a more consistent amount of water throughout the season, while blocks 1,2, and 4 were subject to water stress in July. Therefore, the model simulated ET with higher precision at block 4.

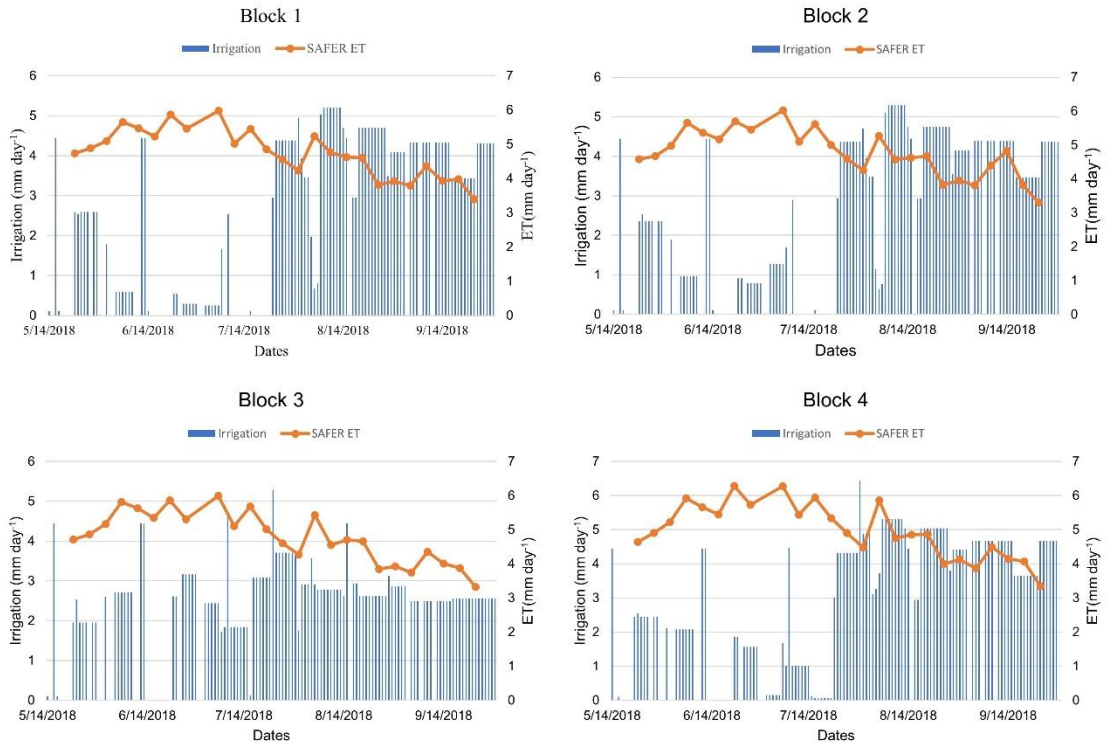

Fig. 9 Irrigation amounts and simulated ET_a values at site 1.

The irrigation totals were similar between blocks at site 1, however it can be seen from Figure 9 how irrigation timing varied in order to achieve different levels of water stress between late June and Early August.

Total irrigation and precipitation during the growing season can be observed in Table 5. Precipitation amounts were not significant at site 1 while at site 2 rainfalls were concentrated during the spring season, maintaining the soil moisture conditions close to field capacity during bud break. Daily water consumption decreased near harvest (Late August and early September), with the last daily ET_a peak at August 5th, the period with the highest maturity of the vines.

Table 5. Total amounts of precipitation during the spring and irrigation during the growing season.

	Precipitation	Irrigation	Total
RIP720#1	12	316.35	328.35
RIP720#2	12	327.58	339.58
RIP720#3	12	305.26	317.26
RIP720#4	12	367.99	379.99
SLM001	226.82	306.69	533.51
SLM002	226.82	306.69	533.51

Although the amount of irrigation applied was pretty much similar between sites, the irrigation interval differs significantly between sites. Site 1 has a higher atmospheric demand and the soil physical properties (sandy) required more frequent applications, with water being applied to the vines almost on a daily basis during the growing season, except during the stress period. This resulted in higher ET values at site 1, which was confirmed by the observed and simulated ET_a. Both mean observed and simulated ET values at site 1 was ~2 mm higher than the ET values at site 2.

2.3.3 Seasonal ET estimation

Time series of daily estimated ET_a (blue) and EC observed ET_a (red) for the 2018 growing season are shown in Figure 10. The estimated values were calculated by interpolating ET_{fr} values generated by SAFER and multiplying those values by the daily ET_0 calculated using the flux tower data. Observed values of ET_a were 69, 71, 83, and 74% of reference ET for Ripperdan at flux towers RIP720#1, RIP720#2, RIP720#3 and RIP720#4 respectively. While at site 2 the observed ET_a were 52 and 47% of reference ET, for SLM001 and SLM002, respectively.

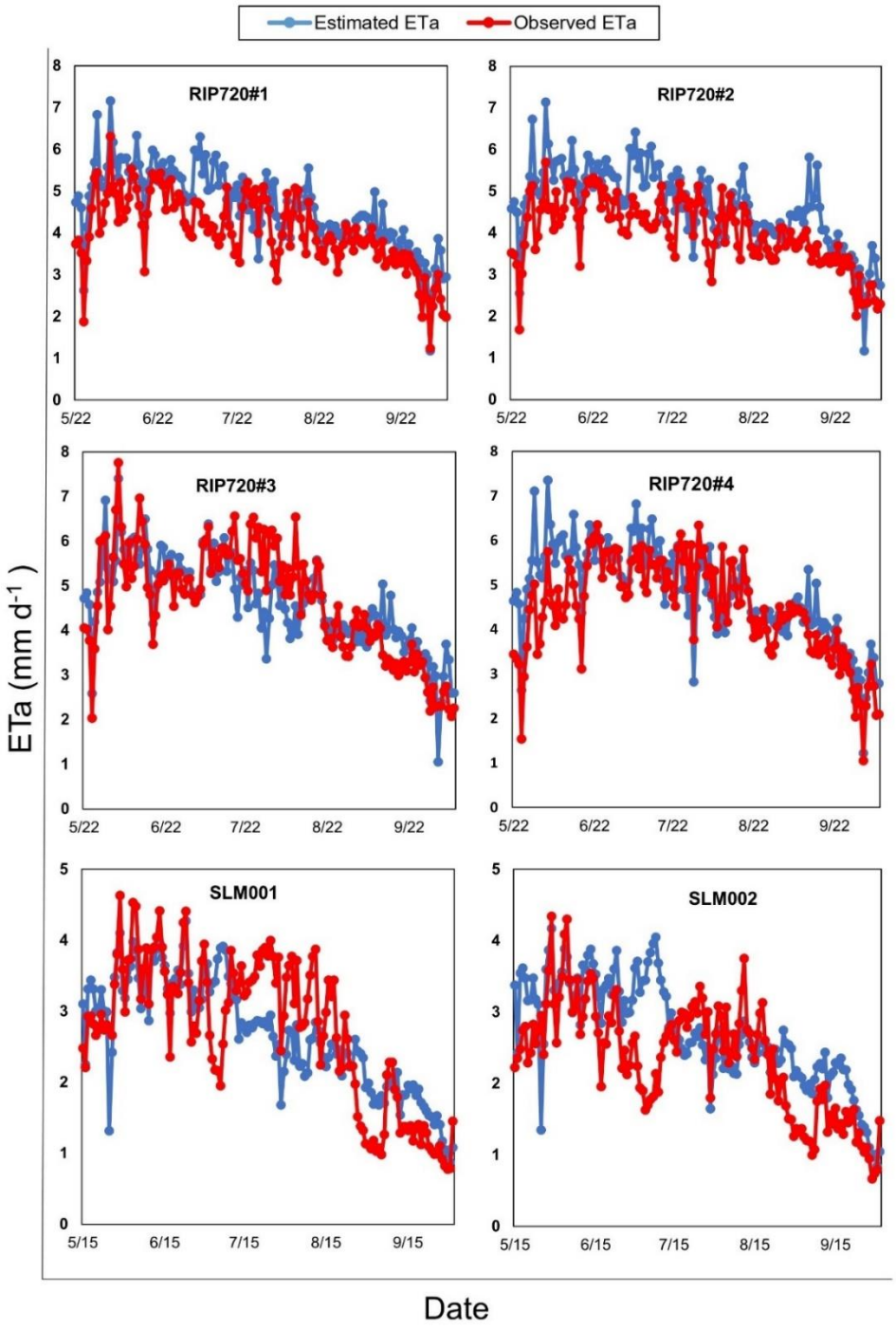

Fig. 10 Time series of observed and estimated *ET* for flux towers at Ripperdan (top panels) and site 2 (bottom panels)

It can be seen a good agreement between modeled and observed ET_a. The model followed the ET_a trends at both sites; however, the model is overestimating daily $ET_{a,}$ especially the peaks in the early portion of the growing season at site 1. It is clear

that the model is capturing the decline of ET_a in every tower Ripperdan after July, caused by induced water stress.

The observed and estimated ET_a is relatively lower at Blocks 1 and 2 in comparison to Blocks 3 and 4 from site 1, during late May and early July. Figure 10 also shows some discrepancies between observed and estimated daily ET_a at Sierra Loma after the early portion of the growing season. The model is underestimating ET at SLM001 and overestimating *ET* at SLM002 after the end of June. This might be because the calibration coefficients were adjusted using the data from SLM001. After the third week of August, the model overestimated ET_a in both vineyards; however, the modeled values followed the trend of observed ones. The precipitation mainly occurred in early spring, and irrigation occurs from May to September, with peaks in late May and earlier September (Kustas et al., 2018).

Figure 11 shows cumulative modeled ET_a (blue) and cumulative observed ET_a (red) in both sites for the growing season of 2018. The cumulative values on site 2 are significantly lower than the ones from site 1.

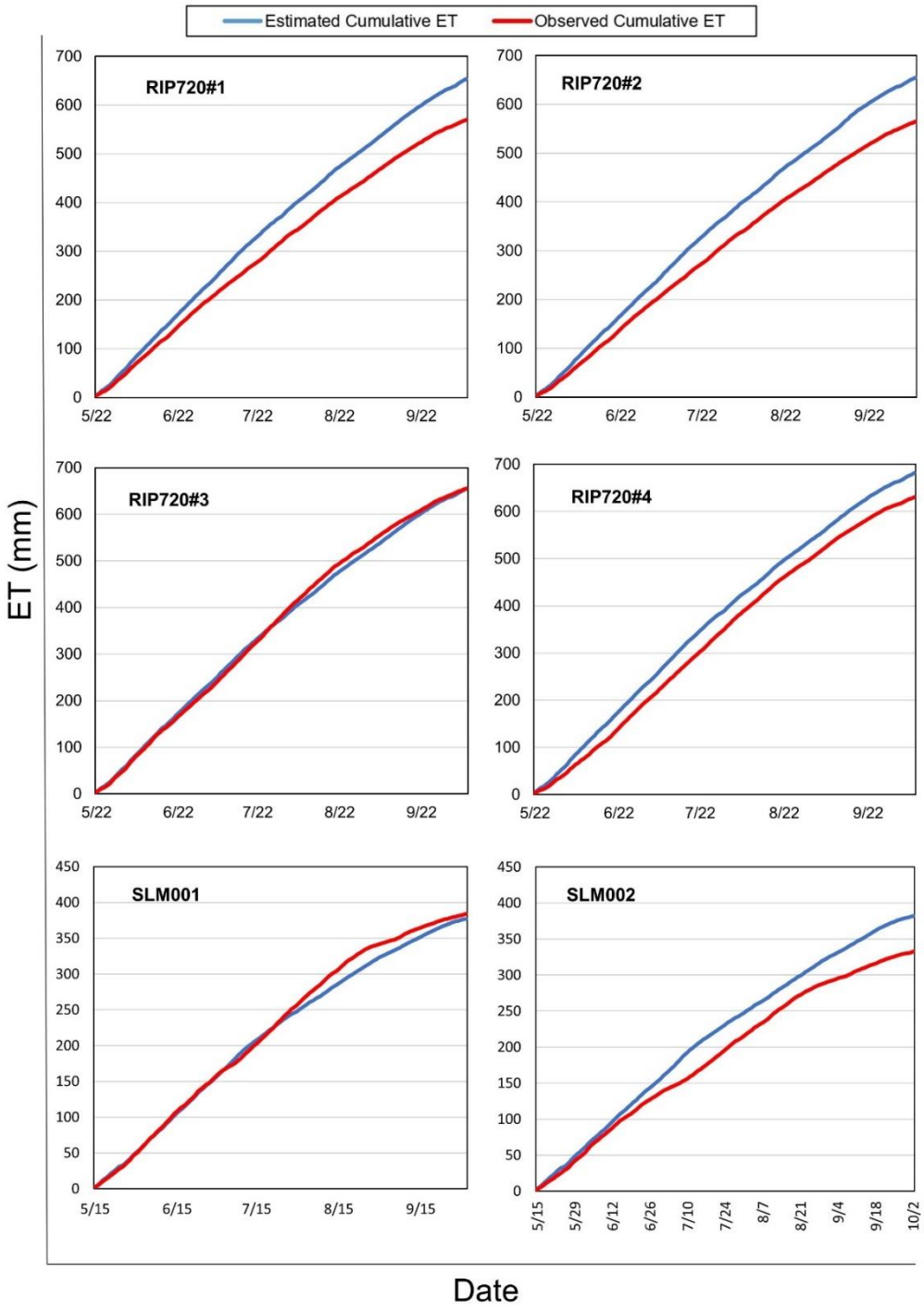

Fig. 11 Time series of observed and estimated accumulated ET for flux towers at the site 1 (top panels) and site 2 (bottom panels)

The cumulative precipitation at Sierra Loma increased from 2016 and 2017, causing a decrease in cumulative irrigation. However, the precipitation rates were lower in 2018, but the irrigation amounts remained the same. This caused water into

the system to decrease by roughly 100 mm, and a decrease in total observed ET compared to the previous years, which were 248 mm at SLM001 and 261 mm at SLM002. Also, at SLM001 the vineyard blocks experienced grapevine red blotch-associated virus, probably decreasing the ability of vines to transpire causing observed ET rates to decrease to values much lower than previous years (Knipper et al. 2020).

The model prediction capabilities seem to improve at the season scale at site 1. This was especially the case at block 3 where there is close agreement between modeled and observed cumulative ET_a. The discrepancies observed at Ripperdan seem to be caused by the overestimation at the peaks observed for late May and early June in every block. The cumulative ET estimation for RIP720#2 was 655 mm, and the observed cumulative ET was 564 showing the highest discrepancy, with an overestimation of total ET by 90 mm. However, the total estimated ET on RIP720#3 was 654 mm, while the observed cumulative ET was 649 mm, with an overestimation of 5 mm for the whole growing season. A seasonal quantitative assessment of the modeled and observed actual evapotranspiration is reported in Table 5.

Table 5. Statistics of the seasonal observed and estimated *ET* at the flux towers located at site 1 and 2.

Site	EC_Total (mm)	SAFER_total (mm)	Residuals (mm)	R^2
RIP720#1	569	653	-84	0.68
RIP720#2	564	655	-90	0.60
RIP720#3	649	654	-5	0.65
RIP720#4	630	681	-51	0.65
SLM001	384	377	6	0.60
SLM002	332	381	-49	0.44

Observed cumulative ET_a variations within site 1 were in the order of 84 mm, while the variations estimated by SAFER were about 28 mm. This showed the model limitation on estimating the different stress levels applied to the same vineyard at site 1. The same limitation can be observed at Sierra Loma where the model estimated a variation of 4 mm between vineyards thought the entire season while the observed variations were about 52 mm. The model predicted higher cumulative ET values for

Ripperdan in agreement with the observed values. The average cumulative ET for site 1 was 661 mm while the average at site 2 was 379 mm, representing a difference of 57%.

2.3.4 Spatial analysis

Satellite-derived *ET* estimation at 10 m resolution can assist in identifying areas with significant deviations in water consumption within and between vineyard blocks. We evaluated the spatial variability of ET by calculating the standard deviation during 2018 growing season for each pixel.

Figure 12 shows the standard deviation map for site 1. The map indicates that the simulated ET spatial variability was around 0.75 to 1.00 mm d^{-1} through the season. These values were consistent with the standard deviation of observed ET in the four blocks, which ranged from 0.84 to 0.92 mm. The map indicates that the spatial variation is homogenous over site 1.

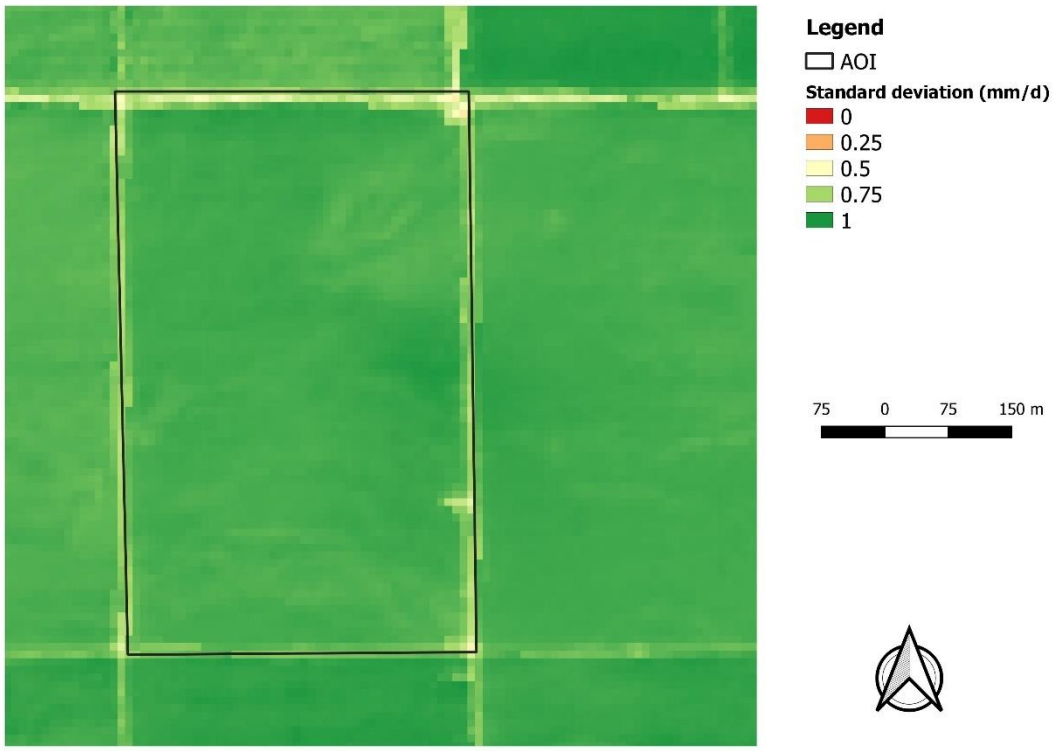

Fig. 12 ET Standard deviation at Site 1 (Ripperdan).

The ET_a standard deviation map for the Sierra Loma is shown in Figure 12. Sierra Loma has higher spatial variability associated with soil and phenological properties. The ET_a standard deviation ranged from 0.4 to 1.6 mm between vines. The variation was higher at the southern portion of SLM002 vineyard with a standard deviation of 1.6 mm while at the central portion the standard deviation was 0.8 mm. At the northern vineyard the variations were higher at the center of the vineyard reaching standard deviation values of 1.2 mm while more constant ET standard deviation were observed at the Northwest boundary (0.4 mm). The variations between blocks at Ripperdan were in the order of 1 mm, while at Sierra Loma, the variations were in the order of 1.6 mm.

The model was able to simulate the seasonal trend of *ET*. However, it showed some limitations in discriminating sensible differences in ET values within the same vineyard at Ripperdan. However, LST approximation using optical Sentinel 2 data can be a good alternative for generating ET maps with a smaller latency between images. SAFER ET_a products can be generated with an excellent temporal resolution of 5 days, showing the potential of using this model as a source of information for water use management in semi-arid regions where the water resource is scarce.

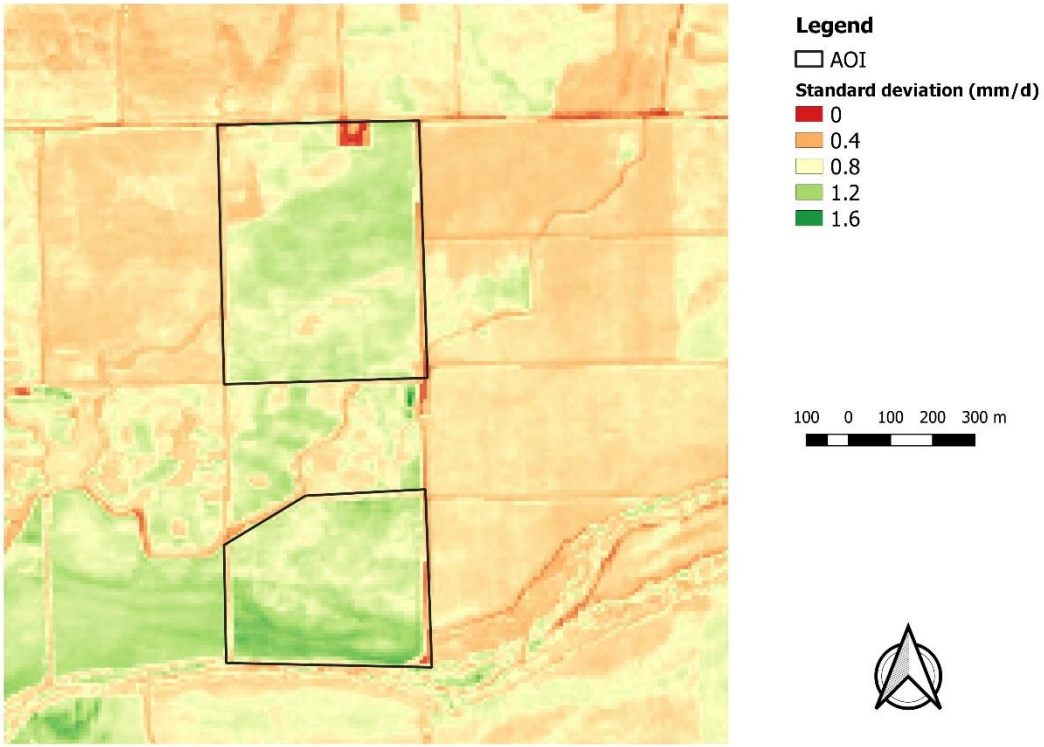

Fig. 13 ET Standard deviation at Site 2 (Sierra Loma).

2.4 Conclusions

Due to its empiric nature, SAFER algorithm is subject to numerous sources of error including imprecise meteorological measurements as any remote sensing ET model, miscalculations during the atmospheric correction process and bad fit of regression coefficients to different areas. The ET_a products derived by SAFER at a 10 m spatial resolution, with a 5-day revisiting time, were validated over two different sites equipped with 6 EC flux towers. The results indicate the potential of this ET model to inform irrigation management and monitor water consumption in vineyards.

The capabilities of the model on deriving LST from optical bands along with meteorological data were evaluated in this study within different vineyards. The results indicate that SAFER provides a good approximation of LST with an average RMSE of 3.79 C° day^{-1}. With that information, it was obtained RMSE values of 0.75 mm day^{-1} at site 1 and 0.64 mm day^{-1} in the estimated ET_a at site 2 on the validation data. Daily MAE ranged from 0.56 to 0.58 mm day^{-1}, what can be considered appropriate for irrigation management purposes.

The ET_a calculated by SAFER was able to capture the seasonal trend of water consumption at both sites. However, the model could not estimate with significant precision the different stress levels applied to each block at Ripperdan. Spatial analysis indicated that Sierra Loma has higher variability between and within vineyards. Nevertheless, the model was able to represent the changes in water surface conditions after the induced stress.

The model has several error sources; thus, the calibration process is absolutely required to obtain satisfactory results in order to apply SAFER for ET estimation. The application of this model without calibration, might led to misinterpretation of crop water demand and gross mistakes regarding ET_a estimations. This is one huge limitation of the model, since it needs to be calibrated to every new environmental condition it is applied. This requires ET data, what might not be easily available since eddy covariance flux towers and lysimeters measurements are scarce and are expensive to obtain. However, ET can be derived from soil moisture data using the water balance approach and then SAFER can be calibrated with this data.

The approach presented in this paper can be a solution for the challenge regarding Landsat's 16-day revisit time. Landsat temporal resolution is not enough to

provide ET_a information for water resources management, especially in high-cost crops like vineyards, where the vines undergo periods of stress during the veraison stage for developing grape quality. The results presented in this paper showed that it is possible to obtain satisfactory *ETa* using visible/near-infrared imagery even in areas with high spatial variation of soil moisture conditions, requiring calibration with additional or independent data sources, like flux towers. With adequate calibration, SAFER has the advantage of being a relatively simple algorithm and has the potential to provide ET operationally to growers for irrigation management

Acknowledgements This paper was possible thanks to the scholarship granted from the Brazilian Federal Agency for Support and Evaluation of Graduate Education (CAPES), in the scope of the Program CAPES-PrInt, process number 88887.467878/2019-00, International Cooperation Project number 41/2017. Authors would like to thank the staff of Viticulture, Chemistry and Enology Division of E&J Gallo Winery for the collection and processing of field data and irrigation management. Authors would also like to thank USDA-GRAPEX team for the data collection and processing of eddy covariance flux towers.

Compliance with ethical standards

Conflict of interest Authors report no conflict of interest in the material present in this study

References

Aboutalebi M, Torres-Rua AF, McKee M, Kustas WP, Nieto H, Alsina MM, White A, Prueger JH, McKee L, Alfieri J, Hipps L (2020) Incorporation of unmanned aerial vehicle (UAV) point cloud products into remote sensing evapotranspiration models. Remote sensing, 12(1), p.50.

Alfieri JG, Kustas WP, Prueger JH, McKee LG, Hipps LE, Gao F, (2019) A multi-year intercomparison of micrometeorological observations at adjacent vineyards in California's Central Valley during GRAPEX. Irrig.Sci. 37: 345–357.

Allen RG, Pereira LS, Raes D, Smith M (1998) Crop evapotranspiration. Guidelines for computing crop water requirements. FAO Irrigation and Drainage Paper. FAO, Rome, Italy 56.

Allen RG, Hartogensis O, de Bruin HAR (2000a) Long-Wave Radiation over Alfafa During the RAPID Field Campaign in Southern Idaho; Research Report; Univ. of Idaho: Kimberly, ID, USA.

Allen RG (2000b) REF-ET, Reference Evapotranspiration Calculator Version Windows 2.0. Univ of Idaho Res. And Ext. Center, Kimberly, ID, 82 p.
Allen RG, Tasumi M, Trezza R (2007) Satellite-based energy balance for mapping evapotranspiration with internalized calibration (METRIC) – model. J Irrig Drain E 133: 380–394.

Anderson MC, Kustas WP, Norman JM, Hain CR, Mecikalski JR, Schultz L, González-Dugo MP, Cammalleri C, d'Urso G, Pimstein A, Gao F (2011) Mapping daily evapotranspiration at field to continental scales using geostationary and polar orbiting satellite imagery, Hydrol. Earth Syst. Sci., 15: 223–239.

Bastiaanssen WGM, Menenti M, Feddes RA, Holtslag AAM (1998) A remote sensing surface energy balance algorithm for land (SEBAL): 1. Formulation. J. Hydrol. 212-213: 198–212.

Cai JB, Liu Y, Xu D, Paredes P, Pereira L S (2009) Simulation of the soil water balance of wheat using daily weather forecast messages to estimate the reference evapotranspiration. Hydrol Earth Syst Sci 13:1045–1059.

Cataldo E, Salvi L, Mattii GB (2021) Effects of irrigation on ecophysiology, sugar content and thiol precursors (3-S-cysteinylhexan-1-ol and 3-S-glutathionylhexan-1-ol) on Vitis vinifera cv. Sauvignon Blanc, Plant Physiology and Biochemistry 164: 247-259.

Courault D, Seguin B, Olioso A(2005) Review on estimation of evapotranspiration from remote sensing data: From empirical to numerical modeling approaches. Irrig Drainage Syst 19:223–249.

FAO (2020) The state of food and agriculture 2021. Overcoming Water Challenges in Agriculture, Fao, Rome, Italy.

Foken T (2008) The energy balance closure problem: An overview. Ecol Appl 18: 1351–1367.

Gago J, Fernie AR, Nikoloski Z, Tohge T, Martorell S, Escalona JM, Ribas-Carbó M, Flexas J, Medrano H (2017) Integrative field scale phenotyping for investigating metabolic components of water stress within a vineyard. *Plant Methods* 13:90.

Glenn EP, Huete AR, Nagler PL, Hirschboeck KK, Brown P (2007) Integrating Remote Sensing and Ground Methods to Estimate Evapotranspiration. Critical Reviews in Plant Sciences 26:139-168.

Howell TA, Schneider AD, Dusek DA, Marek TH, Steiner JL (1995) Calibration and scale performance of Bushland weighing lysimeters. Trans Am Soc Agric Eng 38(4):1019–1024.

Kliewer WM, Freeman BM, Hosssom C (1983) Effect of Irrigation, Crop Level and Potassium Fertilization on Carignane Vines. I. Degree of Water Stress and Effect on Growth and Yield. Am J Enol Vitic 34:186-196.

Knipper K, Kustas WP, Anderson MC, Alfieri JG, Prueger JH, Gao F, McKee LG, Hipps LE, Alsina M (2018) Monitoring water use and stress with evapotranspiration estimates derived using thermal-based satellite remote sensing in California vineyards. Annual Meeting Abstract. https://ams.confex.com/ams/98Annual/webprogram/Paper327040.html. Acessed May 28th 2021.

Knipper KR, Kustas W, Anderson MC, Alsina MM, Hain CR, Alfieri JG, Prueger JH, Gao F, McKee LG, Sanchez LA (2019) Using High Spatiotemporal Thermal Satellite ET Retrievals for Operational Water Use and Stress Monitoring in a California Vineyard. Remote Sens. 11:2124.

Kustas WP & JM Norman (1996) Use of remote sensing for evapotranspiration monitoring over land surfaces. Hydrological Sciences Journal, 41: 495-516.

Kustas WP, Norman JM (1999) Evaluation of soil and vegetation heat flux predictions using a simple two-source model with radiometric temperatures for partial canopy cover. Agr Forest Meteorol 94: 13–29.

Kustas W, Anderson MC, Alfieri JG, Knipper, K, Torres-Rua A, Parry, CK, Nieto H, Agam N, White WA, Gao F (2018) The Grape Remote Sensing Atmospheric Profile and Evapotranspiration Experiment. Bull. Amer. Meteor Soc 99: 1791-1812.

Kustas WP, Alfieri JG, Nieto H, Gao F, Anderson MC, Prueger JH, Wilson TG (2019a) utility of the two-source energy balance model TSEB in vine and inter-row flux partitioning over the growing season. Irrig Sci 37: 375-388

López-Urrea R, Montoro A, Mañas F, López-Fuster P, Fereres E (2012) Evapotranspiration and crop coefficients from lysimeter measurements of mature 'Tempranillo' wine grapes. Agricultural Water Management 112: 13-20.

McCabe MF, Wood EF (2006) Scale influences on the remote estimation of evapotranspiration using multiple satellite sensors. Remote Sensing of Environment 105: 271-285.

Medrano H, Tomás M, Martorell S, Escalona JM, Pou A, Fuentes S, Flexas J, Bota (2015) Improving water use efficiency of vineyards in semi-arid regions. A review. Agron Sustain Dev 35:499–517.

Moorhead, JE, Marek, GW, Colaizzi PD, Gowda PH, Evett SR, Brauer DK, Marek TH, Porter DO (2017) Evaluation of Sensible Heat Flux and Evapotranspiration Estimates Using a Surface Layer Scintillometer and a Large Weighing Lysimeter. Sensors 17:2350

Nassar, A, Torres-Rua, A, Kustas, W, Nieto, H, McKee, M, Hipps, L, Alfieri, J, Prueger, J, Alsina, MM, McKee, L, Coopmans, C, Sanchez, L, Dokoozlian, N (2020) To what extent does the Eddy Covariance footprint cutoff influence the estimation of surface energy fluxes using two source energy balance model and high-resoltuion imagery in commercial vineyards. Autonomous Air and Ground Sensing Systems for Agricultural Optimization and Phenotyping V Proceedings of SPIE, 11414.

Nieto, H, Kustas, WP, Torres-Rúa, A, Alfieri, JG, Gao, F, Anderson, MC, White, WA, Song, L, del Mar Alsina, M, Prueger, JH, McKee, M (2019a) Evaluation of TSEB turbulent fluxes using different methods for the retrieval of soil and canopy component temperatures from UAV thermal and multispectral imagery. Irrigation science, 37(3), pp.389-406.

Nieto H, Kustas WP, Torres-Rúa A, Alfieri JG, Gao F, Anderson MC, White WA, Song L, del Mar Alsina M, Prueger JH, McKee M, Elarab M, McKee LG (2019b) Evaluation of TSEB turbulent fluxes using different methods for the retrieval of soil and canopy component temperatures from UAV thermal and multispectral imagery. Irrig Sci 37: 389-406.

Norman JM, Kustas WP, Humes KS (1995) A two-source approach for estimating soil and vegetation energy fluxes from observations of directional radiometric surface temperatures. Agr Forest Meteorol 77: 263–293.

Paranychianakis NV, Aggelides S, Angelakis AN (2004) Influence of rootstock, irrigation level and recycled water on growth and yield of Soultanina grapevines, Agricultural Water Management, 69: 13-27.

Pimentel D, Berger B, Filiberto D, Newton M, Wolfe B, Karabinakis E, Clark S, Poon E, Abbett E, Nandagopal S (2004) Water Resources: Agricultural and Environmental Issues, *BioScience*, 54, 10: 909–918.

Prueger JH, Hatfield JL, Aase JK, Pikul JL (1997) Bowen-Ratio Comparisons with Lysimeter Evapotranspiration. Agron J 89:730-736.

Sánchez JM, López-Urrea R, Valentín F, Caselles V, Galve JM (2019) Lysimeter assessment of the Simplified Two-Source Energy Balance model and eddy covariance system to estimate vineyard evapotranspiration. Agric and For Meteo 274: 172-183.

Sanchez LA, Sam B, Alsina MM, Hinds N, Klein LJ Dokoozlian N (2017) Improving vineyard water use efficiency and yield with variable rate irrigation in California. Advances in Animal Biosciences 8:574–577.

Santesteban LG, Royo JB (2006) Water status, leaf area and fruit load influence on berry weight and sugar accumulation of cv. 'Tempranillo' under semiarid conditions, Scientia Horticulturae, 109: 60-65.

Sarel Munitz, Amnon Schwartz, Yishai Netzer (2019) Water consumption, crop coefficient and leaf area relations of a Vitis vinifera cv. 'Cabernet Sauvignon' vineyard, Agric Water Manag 219: 86-94.

Silva COF, Teixeira AHC, Manzione RL (2019) agriwater: An R package for spatial modelling of energy balance and actual evapotranspiration using satellite images and agrometeorological data. Env. Model. and Soft 120: 104-497.

Silva COF, Manzione RL, Filho JLA (2018). Large-Scale Spatial Modeling of Crop Coefficient and Biomass Production in Agroecosystems in Southeast Brazil. Hortic. 4:44.

Shi TT, Guan DX, Wu JB, Wang AZ, Jin CJ, Han SJ (2008) Comparison of methods for estimating evapotranspiration rate of dry forest canopy: Eddy covariance, Bowen ratio energy balance, and Penman-Monteith equation, J Geophys Res. 113.

Spittlehouse DL, Black TA (1980) Evaluation of the Bowen ratio/energy balance method for determining forest evapotranspiration. Atmosphere-Ocean 18: 98-116.

Tablemorad H, Ahmadnejad A, Eslamian S, Ostad-ali-askari K, Singh VP (2020) Evaluation of uncertainty in evapotranspiration values by FAO56-Penman-Monteith and Hargreaves-Samani methods. Inter Journ of Hydro Sci and Tech 10:

Trambouze W, Bertuzzi P, Voltz M (1998) Comparison of methods for estimating actual evapotranspiration in a row-cropped vineyard. Agric and For Meteo 91: 193-208.

Teixeira AH de C, Bastiaanssen WGM, Ahmad MD, Bos MG, Moura, MSB (2008) Analysis of energy fluxes and vegetation-atmosphere parameters in irrigated and natural ecosystems of semi-arid Brazil. J. Hydrol. 362: 110–127.

Teixeira AH de C, Bastiaanssen, WGM, Ahmad MD, Bos MG (2009) Reviewing SEBAL input parameters for assessing evapotranspiration and water productivity for the Low-Middle São Francisco River basin, Brazil Part A: Calibration and validation. Agric. For. Meteorol *149*: 462–476.

Teixeira AH de C, Victoria DC, Andrade RG, Leivas JF, Bolfe EL, Cruz CR (2014a) Coupling of MODIS images and agrometeorological data for agricultural water productivity analyses in the Mato Grosso State, Brazil. Proceedings of SPIE, 9239.

Teixeira AH de C, Hernandez FBT, Lopes HL, Scherer-Warren M, Bassoi LH (2014b) A Comparative Study of Techniques for Modeling the Spatiotemporal Distribution of Heat and Moisture Fluxes in Different Agroecosystems in Brazil. In: Petropoulos GG (ed) Remote Sensing of Energy Fluxes and Soil Moisture Content. 1ed.Boca Raton, Florida, pp 169-191.

Teixeira AH de C, Padovani CR, Andrande RG, Leivas JF, Victoria D de C, Galdino S (2015) Use of Modis Images to Quantify the Radiation and Energy Balances in the Brazilian Pantanal. Remote Sens 7: 14597-14619.

Ukkola AM and Prentice IC (2013) A worldwide analysis of trends in water-balance evapotranspiration, Hydrol. Earth Syst. Sci 17: 4177–4187.

Venancio LP, Mantovani EC, Amaral CH, Neale CM, Filgueiras R, Gonçalves IZ, Cunha FF (2020) Evapotranspiration mapping of commercial corn fields in Brazil using SAFER algorithm. Sci. Agric. 78(4).

Westerhoff RS (2015) Using uncertainty of Penman and Penman–Monteith methods in combined satellite and ground-based evapotranspiration estimates. Rem Sens of Env 169: 102-112.

Wilson KB, Hanson PJ, Mulholland PJ, Baldocchi DD, Wullschleger SD (2001) A comparison of methods for determining forest evapotranspiration and its components: sap-flow, soil water budget, eddy covariance and catchment water balance. Agric and For Meteo106: 153-168.

Zhang K, Kimball JS, Running SW (2016) A review of remote sensing based actual evapotranspiration estimation. Water 3: 834-853.

CHAPTER 3[4]

ESTIMATIVA DE UMIDADE DO SOLO POR MEIO DE APRENDIZADO DE MÁQUINA USANDO IMAGENS DE VEÍCULO AÉREO NÃO TRIPULADO (VANT)

ANDERSON LUIZ DOS SANTOS SAFRE[1]; CAIO NASCIMENTO FERNANDES[2]; JOÃO CARLOS CURY SAAD[3]

[1]*Aluno de Doutorado em Irrigação e Drenagem, Departamento de Engenharia Rural, UNESP-Faculdade de Ciências Agronômicas, R. José Barbosa de Barros, 1780, CEP 18610-034, Botucatu-SP, Brasil. E-mail: andersonsafre@gmail.com*
[2]*Aluno de Mestrado em Irrigação e Drenagem, Departamento de Engenharia Rural, UNESP-Faculdade de Ciências Agronômicas, R. José Barbosa de Barros, 1780, CEP 18610-034, Botucatu-SP, Brasil. E-mail: caionfernandes@hotmail.com*
[3]*Professor Titular, Departamento de Engenharia Rural, UNESP-Faculdade de Ciências Agronômicas, R. José Barbosa de Barros, 1780, CEP 18610-034, Botucatu-SP, Brasil. E-mail: joaosaad@fca.unesp.br*

RESUMO

A umidade do solo é um parâmetro importante para o cálculo da lâmina e manejo da irrigação, pois está diretamente relacionada ao conteúdo de água no solo. Técnicas de sensoriamento remoto aliadas a modelos estatísticos podem ser usadas para estimar a variabilidade espacial da umidade do solo, extrapolando medidas pontuais. O objetivo desse estudo foi determinar a umidade do solo por meio de algoritmos de *machine learning* (aprendizado de máquina) como *Support Vector Regression* (SVR), *Random Forests* (RF) e *Artificial Neural Networks* (ANN). Utilizou-se imagens multiespectrais de alta resolução adquiridas por meio de um Veículo Aéreo Não Tripulado (VANT) em uma área de feijão irrigado na Fazenda Experimental Lageado da Unesp, em Botucatu, SP, Brasil. Adotarram-se como dados de entrada nos modelos, as refletâncias nas bandas do verde, vermelho, infravermelho próximo e o NDVI. Todos os algoritmos tiveram performance adequada, porém o que melhor estimou a umidade do solo foi o SVR, com erro médio quadrático (RMSE) de 0,46 vol. % e coeficiente de determinação (R^2) de 0,71.

Palavras-chave: umidade do solo, aprendizado de máquinas, VANT, redes neurais.

SAFRE, A. L. S.; FERNANDES, C. N.; SAAD, J. C. C.
SOIL MOISTURE ESTIMATION THROUGH MACHINE LEARNING USING UNMANNED AERIAL VEHICLE (UAV) IMAGES

ABSTRACT

The soil moisture is an important parameter for the calculation of water depth and irrigation management since it is directly related to the soil water content. Remote sensing techniques combined with statistical models can be used to estimate the spatial variability of soil moisture, extrapolating point measurements. The objective of this study was to determine the soil

[4] Paper published at Irriga journal

moisture through machine learning algorithms such as Support Vector Regression (SVR), Random Forests (RF), and Artificial Neural Networks (ANN). High resolution multispectral images obtained by an Unmanned Aerial Vehicle (UAV) in an irrigated bean area at the Experimental Lageado Farm at Unesp in Botucatu, SP, Brazil, were used. The reflectances in the Green, Red and Near Infrared bands along with the NDVI vegetation index were used as inputs for the models. All the algorithms performed well; however, the model that best fitted the data was the SVR, with mean square error (RMSE) of 0.46% of the estimated soil moisture and determination coefficient (R^2) of 0.71.

Keywords: soil moisture, machine learning, UAV, artificial neural networks.

3.1 INTRODUÇÃO

A disponibilidade dos recursos hídricos e energéticos para a agricultura é cada vez mais limitada devido às mudanças climáticas e à demanda crescente por alimentos. Os agro ecossistemas, principalmente sob condições de irrigação, necessitam de técnicas e manejos que proporcionem altos níveis de eficiência para que haja a preservação dos recursos naturais ao mesmo tempo em que se configuram sistemas de produção agrícolas mais competitivos. Deste modo, o monitoramento da umidade do solo é uma das práticas fundamentais para se realizar um manejo eficiente e racional dos sistemas agrícolas irrigados, visto que a aplicação dessa técnica permite um melhor desenvolvimento das culturas e uma utilização otimizada tanto dos recursos hídricos como energéticos (HUISMAN et al., 2003; DUKES; ZOTARELLI; MORGAN, 2010; MONTESANO et al., 2015; BRITO et al., 2009; FREITAS et al., 2012; BRITO et al., 2014).

A obtenção da umidade do solo pode ser feita por meio de métodos diretos ou indiretos. A determinação da umidade pelo método direto é feita por meio da diferença entre a massa da amostra de solo em seu estado inicial e após essa ser seca. Resistência do solo à passagem de corrente elétrica, sonda de nêutrons, sensores capacitivos e tensão de água no solo, são exemplos de métodos indiretos de determinação da umidade do solo (TEIXEIRA; COELHO, 2005; DOBRIYAL et al., 2012). O uso do sensoriamento remoto também é um método indireto, pois por meio de imagens capitadas por câmeras acopladas à satélites ou veículos aéreos não tripulados (VANTs) é possível relacionar a umidade do solo com a variação da radiação eletromagnética refletida, utilizando para tal, métodos estatísticos.

A medição da tensão de água no solo com tensiômetros é uma das técnicas mais conhecidas de determinação indireta da umidade. Além de ter menor custo, quando comparada às demais técnicas, apresenta fácil manipulação, alta precisão e possibilidade de automação do sistema de leitura (ARRUDA et al., 2017) e do próprio sistema de irrigação (MONTESANO et al., 2015). A quantificação do teor de água no solo de forma precisa é necessária para auxiliar a tomada de decisão do produtor de quando e quanto irrigar e assim, ter um manejo eficiente e racional (THALHEIMER, 2013), fornecendo a quantidade de água adequada ao desenvolvimento das culturas de forma plena, resultando em ganhos de produtividade.

No desenvolvimento inicial do tensiômetro, o elemento químico mercúrio foi utilizado como escala de medida, sendo implementado por Livingston em 1908 (OR, 2001), apresentando a capacidade de medir o potencial mátrico do solo (LIBARDI, 2005). O contato do solo com a capsula porosa do tensiômetro proporciona um equilíbrio do meio. Conforme a umidade do solo diminui, a água presente no tensiômetro é sorvida pela tensão matricial gerada, reduzindo a pressão interna do sistema e ocasionando um aumento da tensão no tensiômetro. A

leitura da tensão é comparada com a curva de retenção de água característica do solo e assim, a umidade do solo pode ser é determinada (CAMARGO; GROHMANN; CAMARGO, 1982).

A agricultura de precisão possibilita aos produtores monitorar as condições especificas de cada local, possibilitando um manejo extremamente eficiente, justamente por apresentar como princípio principal, o uso de parâmetros específicos da propriedade agrícola. Dentro da agricultura de precisão, podemos destacar os sistemas de informações espaciais, como o sistema de informação geográfica (SIG), ferramentas de sensoriamento remoto e os sistemas de posicionamento global.

Pode-se definir o sensoriamento remoto como o método de aquisição de informações de um determinado fenômeno ou comportamento da superfície terrestre sem existir o contato físico (JENSEN, 2009). Esse método permite a identificação de características de alvos específicos a partir da interação com a radiação eletromagnética (REM) (ROSA, 2009). Para isso, são utilizados sensores acoplados em satélites, aeronaves, VANTs e outras plataformas.

A REM é a energia que se desloca na velocidade da luz, seja na forma de partículas ou ondas eletromagnéticas, não sendo necessário um meio físico para sua propagação (ROSA, 2009). Compondo a REM, está o espectro eletromagnético que envolve o intervalo de todos os comprimentos de onda, desde os raios gama, até as ondas de rádio (NOVO, 2008). Ao se propagar pelo espaço, o fluxo de radiação eletromagnética pode ou não interagir com objetos ou a superfície e assim, ser refletido, absorvido ou transmitido (ROSA, 2009; PONZONI; SHIMABUKURO, 2010). Os sensores utilizados no sensoriamento remoto registram a reflectância do alvo, de grande importância na agricultura, pois diversas informações importantes a respeito do estado metabólico das culturas podem ser extraídas.

Recentemente, métodos estatísticos não lineares, como o aprendizado de máquinas (*machine learning*), vêm sendo aplicados a dados de sensoriamento remoto para a estimativa de parâmetros físicos. Algoritmos como *Random Forest* (BREIMAN, 2001), *Support Vector Machines* (KOVAČEVIC; BAJAT; GAJIC, 2010; PRIORI; BIANCONI; CONSTANTINI; 2014), Redes Neurais Artificiais (AITKENHEAD et al., 2013; SILVEIRA et al., 2013) e vizinho próximo – k (MANSUY et al., 2014) têm sido bastante utilizados na agricultura de precisão.

O objetivo desta pesquisa foi determinar a umidade do solo a partir de imagens obtidas por meio de veículo aéreo não tripulado (VANT), utilizando algoritmos de *machine learning*, como *Support Vector Regression*, *Random Forests* e Redes Neurais Artificiais, tendo como referência, a medida de tensão de água no solo.

3.2 MATERIAL E MÉTODOS

3.2.1 Área de estudo

O estudo foi conduzido em uma parcela de 174 m², localizada na área experimental do Departamento de Engenharia Rural e Socioeconomia, da Faculdade de Ciências Agronômicas (FCA) da Universidade Estadual Paulista “Júlio de Mesquita Filho” (Unesp) de Botucatu, SP, como pode ser observado na Figura 1.

Figura 1. Localização da área de estudo.

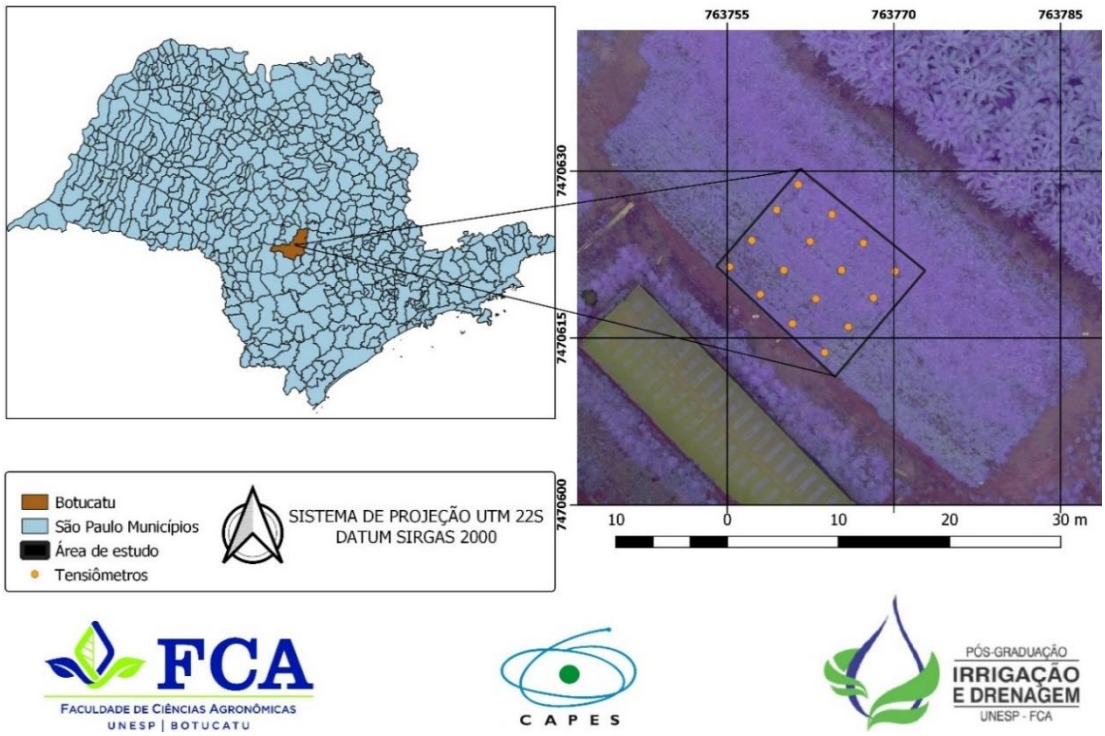

O solo da área é caracterizado como Nitossolo vermelho de textura argilosa, segundo o Mapa Pedológico do Estado de São Paulo (ROSSI, 2017). De acordo com a classificação de Köppen e Geiger (1928), o clima da região é subtropical úmido, Cfa, com duas estações bem definidas, verão quente e úmido e inverno seco. O relevo é plano com declividade de 1%.

Na parcela, foi instalada a cultura do feijão (*Phaseolous vulgaris* L.), variedade Dama, com ciclo de 91 dias. A irrigação foi realizada via aspersão convencional com sobreposição dos aspersores de 12 x 12 m.

Na Figura 2, visualizam-se os equipamentos utilizados para o aerolevantamento. O VANT o foi um Phantom 3® Professional (fabricante SZ DJI Technology Co., Shenzhen, Guangdong, China). O voo foi realizado de maneira autônoma a uma altitude de 120 m, com 60% de sobreposição lateral e 70% de sobreposição frontal. A câmera utilizada foi uma MAPIR Survey 3W (fabricante MAPIR, Peau Productions, Inc., CA, USA).

A MAPIR é uma câmera modificada com um filtro para registro no Infravermelho próximo (850 nm) e registro no Vermelho (660 nm) e Verde (550 nm), possuindo resolução de 12 megapixels (4032 x 3024), produzindo imagens no formato JPG (8-bits) e RAW (12-bits). Foram utilizadas as configurações padrões de abertura, balanço de branco, Sensibilidade ISO (International Standards Organization), abertura do obturador e exposição, conforme recomendado pelo fabricante. Atualmente, essa câmera é a mais barata no mercado (≅ R$ 6.000) quando comparado a outras câmeras multiespectrais disponíveis como a Parrot Sequoia (≅ R$ 30.000) e Micasense RedEdge-M (≅ R$ 50.000).

Figura 2. VANT e painel de calibração.

Um painel de calibração radiométrica foi utilizado para conversão dos números digitais em reflectância. Foram coletadas imagens antes do voo para calibração, e o processamento das imagens captadas foi realizado através do *software* Mapir Camera Control v. 10/16/2019. Para a calibração geométrica, foi utilizado um receptor GNSS RTK Kronos 200 (fabricante Horizon, Survey Instruments Ltd., Singapore) tendo sido coletados cinco pontos de controle distribuídos na área. Para a estimativa de umidade do solo, foram realizados dois levantamentos, o primeiro no dia 18 e o segundo no dia 20, ambos no mês de janeiro de 2020.

Os instrumentos para o monitoramento da tensão de água no solo são apresentados na Figura 3. Utilizou-se uma bateria com 16 tensiômetros instalados na profundidade de 20 cm. A água nos tensiômetros foi mantida a um nível constante após as medições. ~~A~~ Realizou-se a leitura de tensão por meio de um tensímetro digital de agulha (fabricante Hidrodinâmica Tensiômetros, Piracicaba, Brasil). Retiraram-se amostras de solo para a obtenção e cálculo da curva de retenção, utilizando a metodologia da câmara de pressão. Posteriormente, os valores de tensão foram ajustados por meio do modelo de Van Genuchten (1980) para obtenção dos valores do conteúdo volumétrico de água no solo (cm^3/cm^3). Os dados então foram multiplicados por 100 para a obtenção da umidade do solo em porcentagem.

Figura 3. Tensíômetro e tensímetro digital de agulha.

3.2.2 Support Vector Regression

Os algoritmos de *Support Vector Machines* também podem ser aplicados a problemas de regressão por meio da introdução de uma função de perda alternativa (SMOLA, 1996). Enquanto os algoritmos de *Support Vector Regression* (SVR) são uma generalização do problema de classificação encontrados nos classificadores do *Support Vector Machines*. Nesses algorítmicos, os erros são fixados de maneira a descartar pontos para a regressão de acordo com os pontos dentro do intervalo de confiança. O critério de otimização penaliza pontos de dados nos quais os valores y diferem de f(x) mais que o erro ε.

A função genérica de estimativa do SVR pode ser descrita conforme a Equação 1:

$$f(x) = \left(\omega * \Phi(x)\right) + b \quad (1)$$

Em que, Φ é uma transformação não linear para um espaço dimensional maior. O objetivo é encontrar um valor de ω e b de modo que os valores de *x* possam ser determinados minimizando o risco de regressão (R_{reg}) representado pela Equação 2 (WU; HO; LEE, 2004).

$$R_{reg} = C \sum_{i=0}^{l} \Gamma\left(f(x_i) - y_i\right) + \frac{1}{2}\|w\|^2 \quad (2)$$

em que, Γ () é uma função de custo, C é uma constante e o vetor *w* pode ser escrito em termos dos pontos de dados (Equação 3):

$$w = \sum_{i=1}^{l}(a_i - a_i^*)\Phi(x_i) \quad (3)$$

O produto da transformação Φ pode ser estimado usando a função *k* (x_i, *x)* chamada de função Kernel. A Função de Base Radial (RBF) é o Kernel mais utilizado e pode ser definida conforme a Equação 4:

$$RBF = exp\{-\gamma|x - x_i|\} \quad (4)$$

A função de custo mais usada na literatura é a e-insensitivo. Ela determina um tubo delimitado pelos vetores de suporte para corte. Ela é resolvida em função de um valor de erro aceitável com base nos dados (Equação 5).

$$\Gamma(f(x) - y) = |f(x) - y| \geq \varepsilon \quad (5)$$

Mais detalhes sobre a teoria dos SVR podem ser encontrados em Smola e Scholkpof (2004) e Vapnik (1998).

3.2.3 Random Forests

O algoritmo *Random Forests* ou Florestas Aleatórias é um algoritmo de aprendizado supervisionado que utiliza o método de aprendizado em conjunto para classificação e regressão. No algoritmo, são criadas diversas arvores de decisão de maneira aleatória, formando algo semelhante a uma floresta, onde cada árvore é utilizada para definição do resultado final. Tem-se uma coleção de árvores preditoras $h(x;\theta_k)$, k=1,..,K, onde x representa a vetor de entrada observado de comprimento *p* com um vetor aleatório **X** e θ_k são vetores aleatórios distribuídos de maneira idêntica (SEGAL, 2004).

O erro médio quadrático de generalização para qualquer preditor numérico $h(\mathbf{x})$ é descrito conforme a Equação 6 (BREIMAN, 2001):

$$E_{X,Y}(y - h(\boldsymbol{X}))^2 \quad (6)$$

O preditor de *Random Forests* é formado, tomando a média sobre *k* das árvores $\{h(\mathbf{x}, \theta_k)\}$ conforme o número de árvores tende ao infinito (Equação 7):

$$E_{X,Y}(y - méd_k h(\boldsymbol{X}, \theta_k))^2 \rightarrow E_{X,Y}(y - E_\theta h(\boldsymbol{X}; \theta))^2 \quad (7)$$

A quantidade na direita é o erro de predição (generalização) para a *Random Forest* designado PE_f^*. O erro de predição de um arvore individual $h(X;\theta)$ pode ser definido como (Equação 8):

$$PE_t^* = E_\theta E_{X,Y}(y - h(\boldsymbol{X}; \theta))^2 \quad (8)$$

Supondo que para todos θ, a árvore não possuí viés ($EY = E_x h(\mathbf{X}, \theta)$. Então, temos a Equação 9 (SEGAL, 2004):

$$PE_f^* \leq \bar{p} PE_t^* \quad (9)$$

em que, $\bar{p}$ é a correlação ponderada entre os resíduos y – $h(\mathbf{X};\theta)$ e y- $h(\mathbf{X};\theta')$ para θ, θ' que são vetores independentes distribuídos aleatoriamente.

As *Random Forests* funcionam construindo diversas árvores de decisão no processo de treinamento e dando como *output* o valor médio predito pelas árvores individuais. Cada arvore extrai uma amostra aleatória do conjunto, de modo a adicionar mais um elemento de aleatoriedade evitando o *overfitting*. As árvores são rodadas em paralelo não havendo interação entre elas ao construir novas árvores, sendo classificadas como um algoritmo de *bagging* (ensacamento) e não um algoritmo de *boosting* (reforço) como as Redes Neurais.

3.2.4 Artificial Neural Network

Artificial Neural Networks, ou Redes Neurais Artificiais, são algoritmos que usam uma abordagem semelhante à estrutura do cérebro humano para tomada de decisão (MCCULLOCH; PITTS, 1943; ROSENBLATT, 1962; BISHOP, 1995). As variáveis de entrada independentes x_i (i= 1, . . . , *d*) são transformadas em um conjunto de saída dependente y_1,....,y_i. O primeiro estágio da transformação é realizado pelo neurônio ou *Perceptron*. Os *inputs* são multiplicados por um parâmetro de peso w_i que simula os pesos sinápticos nas redes neurais biológicas. Todas as entradas ponderadas serão somadas para dar uma entrada total (Equação 10):

$$a = \sum_{i=1}^{d} w_i x_i + b \quad (10)$$

em que, um viés *b* é adicionado para fornecer um mecanismo para incluir outras influencias, normalmente definido como 1. O processo de aprendizagem começa com algum vetor de pesos arbitrários, sem perda de generalização, podemos assumir ~~que~~ esse ~~seja~~ como o vetor zero (BISHOP, 1995). Uma função de ativação vai definir o limiar aceitável para passar o valor da soma ponderada mais o valor do viés.

O resultado do neurônio é então enviado para uma função de ativação não linear *f*( ) que vai definir, com base no limiar, se esse vai ser ativado ou não (Equação 11).

$$z = f(a) \quad (11)$$

As redes normalmente usam a função sigmoide para o cálculo do limiar. Como esse tipo de rede opera através do neurônio, a partir dos *inputs*, para obter o *output*, são chamadas de *feed-foward* (BISHOP, 1995). As estruturas mais simples de rede possuem somente um neurônio como mostra a Figura 4, entretanto, as estruturas mais utilizadas são chamadas de *Multi Layer Perceptron* (MLP), uma vez que combinam diversas camadas de neurônios.

Figura 4. Modelo matemático de um neurônio artificial. Fonte: Adaptado de Haykin (2009).

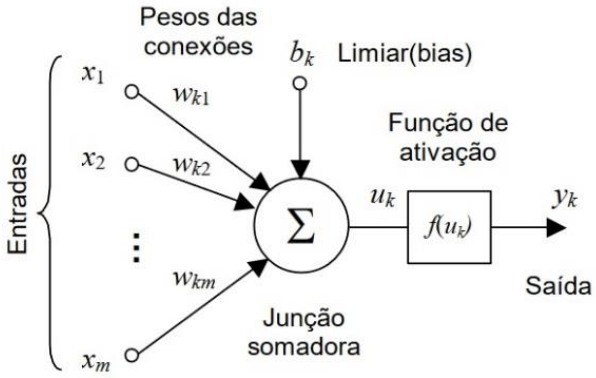

A estrutura *Multi Layer Perceptron* é caracterizada por uma camada de entrada, camadas intermediárias chamadas de camadas ocultas e uma camada de saída. Assim que o processo de aprendizagem progride ao longo do MLP, os neurônios presentes na camada oculta começam a descobrir gradualmente as características salientes que caracterizam os dados de treinamento (HAYKIN, 2009).

O aprendizado da Rede é feito por meio do algoritmo de *Backpropagation*, que faz uso de uma técnica chamada gradiente descendente. Esse algoritmo ajusta os pesos com base na derivada destes em relação ao erro. A Rede é iniciada e os erros são calculados no fim do processo, eles são então propagados de volta às camadas iniciais para ajuste dos pesos. O processo se repete diversas vezes até encontrar a combinação de pesos sinápticos que resultam no menor erro quando então o modelo converge.

Essa técnica mede o erro e a taxa de mudança do erro. Isso leva a grandes modificações quanto maior for o erro, conforme a inclinação diminui ao se aproximar de um mínimo, as mudanças nos pesos se tornam menores (PUJOL; PINTO, 2011). A média de todos os erros quadráticos (E) para a saída é computada para auxiliar na derivada. O descendente é baseado em um gradiente no erro para todo o conjunto de dados segundo a Equação 12 (GROSSAN; ABRAHAM, 2011):

$$\Delta w_{ij}(n) = -\eta * \frac{\delta E}{\varepsilon_{wij}} + a * \Delta w_{ij}(n-1) \quad (12)$$

em que, η^* é a taxa de aprendizado e a^* o momentum.

A utilização desse algoritmo já foi reportada em inúmeros estudos cujo objetivo principal foi a obtenção da estimativa de umidade do solo (JIANG; COTTON, 2004; AHMAD; KALRA; STEPHEN, 2010; KORNELSEN; COULIBALY, 2014; HASSAN-ESFAHANI et al., 2015).

3.2.5 Estratégia de modelagem

Foram utilizados *buffers* circulares ao redor da localização dos tensiômetros com raio de 0,5 m para extração dos valores médios de reflectância de cada banda por meio da ferramenta de estatística zonal do *software* QGIS 3.4. Esses dados foram utilizados como entrada nos algoritmos de *machine learning*. Para as variáveis independentes, utilizou-se as refletâncias nas bandas do Verde, Vermelho, Infravermelho próximo e o Índice de Vegetação por Diferença Normalizada (NDVI). Empregou-se como ~~A~~ variável dependente, ~~era~~ a umidade do solo

registrada por cada tensiômetro nos dois levantamentos realizados (18 e 20 de janeiro de 2020). A matriz de entrada tinha um formato de 32 x 4.

Os dados foram divididos em 70% para treinamento e 30% para teste das predições. Posteriormente, realizou-se uma normalização dos dados por meio do *Standard Scaler* (Equação 13), que padroniza as amostras, removendo a média e deixando a variância unitária com uma distribuição normal gaussiana. Esse processo é um requisito dos algoritmos de *machine learning* para que os dados estejam na mesma escala.

$$z = \frac{(x-u)}{s} \tag{13}$$

Em que, *x* é uma amostra, *u* é a média das amostras de treinamento e *s* é o desvio padrão.

Os algoritmos utilizados nesse estudo foram implementados utilizando a linguagem Python 3.6 por meio da interface de usuário *Jupyter Notebook*, juntamente com as bibliotecas Pandas, Numpy e Scikit-Learn. Em relação aos hiperparâmetros selecionados para os estimadores, no algoritmo de SVR foi utilizado a função Kernel *Radial Basis Function*.

Para o *Random Forests* (RF), utilizou-se 100 árvores de decisão e o critério para otimização foi o '*mean Square Error*'. Já para as *Artificial Neural Networks* (ANN) foi utilizada uma arquitetura de MLP, inicializada com duas camadas ocultas com 100 neurônios cada com a função de ativação 'relu'. A função de custo utilizada foi a "*Square Error*" e a taxa de aprendizado definida como 0,001, o otimizador selecionado foi o 'adam', com a camada de saída sem função de ativação, gerado assim, um número contínuo.

3.2.6 Métricas estatísticas

Para a avaliação do desempenho dos algoritmos de *machine learning* empregados na determinação da estimativa de umidade do solo foram utilizadas as seguintes métricas estatísticas: Erro médio quadrático (*Root Mean Square Error* - RMSE) (Equação 14), Erro médio absoluto (*Mean Absolute Error* - MAE) (Equação 15), Erro médio absoluto percentual (*Mean Absolute Percentage Error* - MAPE) (Equação 16) e Coeficiente de determinação (R^2) (Equação 17).

$$RMSE = \sqrt{\frac{1}{n}\sum_{i=1}^{n}(y_i - x_i)^2} \tag{14}$$

$$MAE = \frac{1}{n}\sum_{i=1}^{n}|y_i - x_i| \tag{15}$$

$$MAPE = \frac{1}{n}\sum_{i=1}^{n}\left|\frac{y_i - x_i}{x_i}\right| * 100 \tag{16}$$

$$R^2 = \frac{\sum_{i=1}^{n}(y_i - x_i)^2}{\sum_{i=1}^{n}(y_i - \bar{y})^2} \tag{17}$$

Em que, y_i são os valores observados de umidade do solo, x_i são os valores simulados, *n* é o número de observações e $\bar{y}$ é a média das observações.

3.4 RESULTADOS E DISCUSSÃO

3.4.1 Umidade do solo e reflectância

Na Figura 5, é possível observar as correlações entre as bandas espectrais (Verde, Vermelho e Infravermelho Próximo), o NDVI e a umidade do solo estimada indiretamente pelos tensiômetros. Observa-se uma correlação negativa entre as bandas do verde e do vermelho e a umidade do solo. Quando a planta não está estressada, a radiação na faixa do vermelho é refletida com menor intensidade devido à absorção da clorofila pelos carotenos e xantofilas, ou seja, áreas com elevado teor de umidade no solo têm menor refletância nessa faixa do espectro eletromagnético.

Figura 5. Gráficos de dispersão demonstrando a correlação entre a umidade do solo e as bandas espectrais.

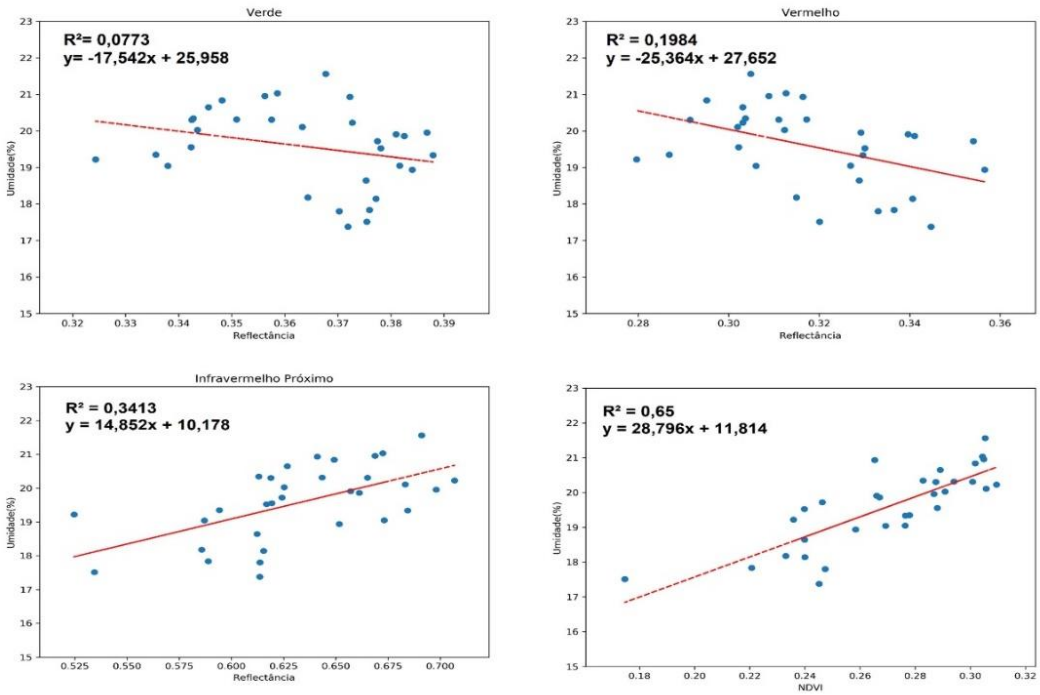

Também é possível identificar uma baixa correlação positiva entre o Infravermelho próximo e a umidade do solo. Isso ocorre porque onde há maior disponibilidade de água, a planta tem um maior desenvolvimento vegetativo, aumentando a refletância no Infravermelho próximo devido ao maior Índice de Área Foliar (IAF). A banda do verde não apresentou correlação significativa com a umidade do solo na profundidade analisada. Esses resultados são similares aos encontrados por Aboutalebi et al. (2019), que observaram a mesma tendência de correlação entre a umidade do solo e essa banda espectral em camadas de solo a partir de 45 cm de profundidade.

É possível notar que existe uma alta correlação positiva entre o NDVI e a umidade do solo (Figura 5). O NDVI está relacionado com a quantidade de umidade no solo, pois uma

planta sem restrições hídricas pode alcançar pleno vigor vegetativo, apresentando altos valores de NDVI, enquanto áreas com baixo NDVI, geralmente associadas a maior presença de solo exposto nos pixels, podem indicar que as plantas estão sofrendo estresse hídrico devido à baixa disponibilidade hídrica no solo (menor umidade). A câmera MAPIR tende a apresentar valores baixos de NDVI como reportado por Gomes et al. (2021).

3.4.2 Performance dos estimadores de machine learning

A Figura 6 apresenta a umidade estimada pelos algoritmos de *machine learning* e a umidade observada nos tensiômetros para os conjuntos de treinamento e teste. Todos os algoritmos tiveram desempenho satisfatório com RMSE < 1 vol. % na estimativa de umidade do solo.

Figura 6. Gráficos de dispersão dos valores de tensão de água no solo observados pelos tensiômetros versus valores estimados pelos algoritmos de *machine learning*.

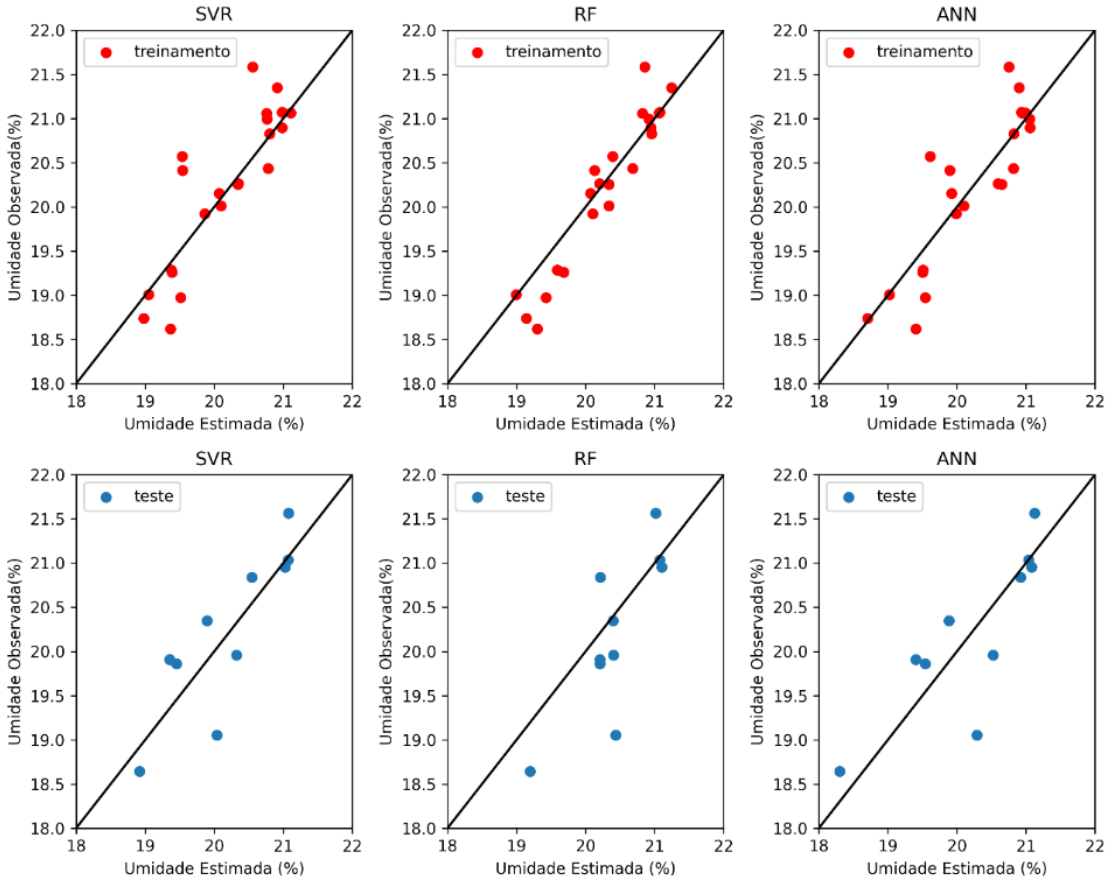

A Tabela 2 apresenta um resumo das estatísticas avaliadas utilizando os dados de teste. Como pode ser observado, o algoritmo SVR foi melhor em relação ao RF e ANN. Isso pode ser confirmado pela distribuição dos pontos em relação a linha 1:1, onde o agrupamento foi maior no algoritmo SVR. O SVR apresentou um RMSE de 0,46 vol. % e o valor do MAPE foi de 4,59 %. O ajuste da regressão foi de 0,71 e o MAE de 0,39 vol. %. O desempenho do algoritmo de ANN foi similar ao SVR com um RMSE de 0,54 vol. % e MAPE de 4,23 %, o R^2

foi de 0,60 e o MAE de 0,40 vol. %. Já o RF apresentou um RMSE de 0,57 vol. % e MAPE de 4,23 %. O R^2 foi de 0,55 com MAE de 0,42 vol. %.

Tabela 1. Resumo das estatísticas dos valores observados versus valores estimados em porcentagem de umidade do solo.

	RMSE[5] **(vol %)**	**MAE (vol %)**	**MAPE (%)**	**R^2**
SVR[6]	0,46	0,39	4,59	0,71
RF	0,57	0,42	4,23	0,55
ANN	0,54	0,40	4,75	0,60

De maneira geral, os modelos conseguiram estimar de maneira precisa o valor da umidade do solo utilizando as bandas do verde, vermelho, infravermelho próximo e o NDVI. Valores muito baixos de erro normalmente estão associados ao fenômeno de *overfitting*, porém ao avaliar os algoritmos nos dados de validação (teste), o R^2 baixo demonstra que o ajuste não foi perfeito, característica essencial de *overfitting* ~~com~~ no qual o R^2 apresenta valores iguais ou muito próximos a 1. Entretanto, os valores de umidade não apresentaram amplitude significativa nos levantamentos (1,3%) o que pode explicar o valor baixo de RMSE.

Os resultados apresentados são semelhantes aos encontrados por Araya et al. (2021), que obtiveram valores para MAE de 3,77 vol. % ao aplicar os mesmos algoritmos empregados neste trabalho em dados multiespectrais coletados pelo sensor Parrot Sequoia (fabricante Parrot SA, Paris, France) em seis levantamentos com 406 amostras de umidade do solo. Ge et al. (2019) também encontraram resultados semelhantes (RMSE = 1,47 vol. %) ao utilizar os algoritmos RF e *Extreme Learning Machine* em 70 amostras de umidade do solo coletadas em um levantamento com uma câmera hiperespectral. Isso demonstra o potencial da utilização de métodos de *machine learning* em dados coletados via sensoriamento remoto e sua aplicação no monitoramento do conteúdo de umidade no solo o que, consequentemente, permite o manejo adequado da irrigação, apresentando-se como uma opção viável à prática da agricultura de precisão.

3.4.3 Mapas de umidade do solo

A Figura 7 apresenta os mapas gerados pelos algoritmos de *machine learning* nos levantamentos realizados nos dias 18 e 20 de janeiro. Todos os mapas apresentam valores menores de umidade no canto inferior esquerdo, o que está de acordo com os dados registrados nos tensiômetros. É possível identificar que o algoritmo RF suavizou os dados, gerando um mapa mais uniforme. Já o algoritmo SVR gerou um mapa de umidade do solo com grande variação espacial para ambos os levantamentos. O algoritmo ANN teve o pior desempenho na estimativa de umidade do solo, apresentando uma maior generalização dos valores, sendo inclusive, possível identificar *clusters* com posições mais definidas.

[5] Root Mean Square Error (RMSE); Mean Absolute Error (MAE); Mean Absolute Percentage Error (MAPE), Coeficiente de determinação (R^2).
[6] Support Vector Regression (SVR); Random Forests (RF) e Artificial Neural Network (ANN).

Figura 7. Mapas de umidade do solo gerados pelos algoritmos de *machine learning* nos dois levantamentos.

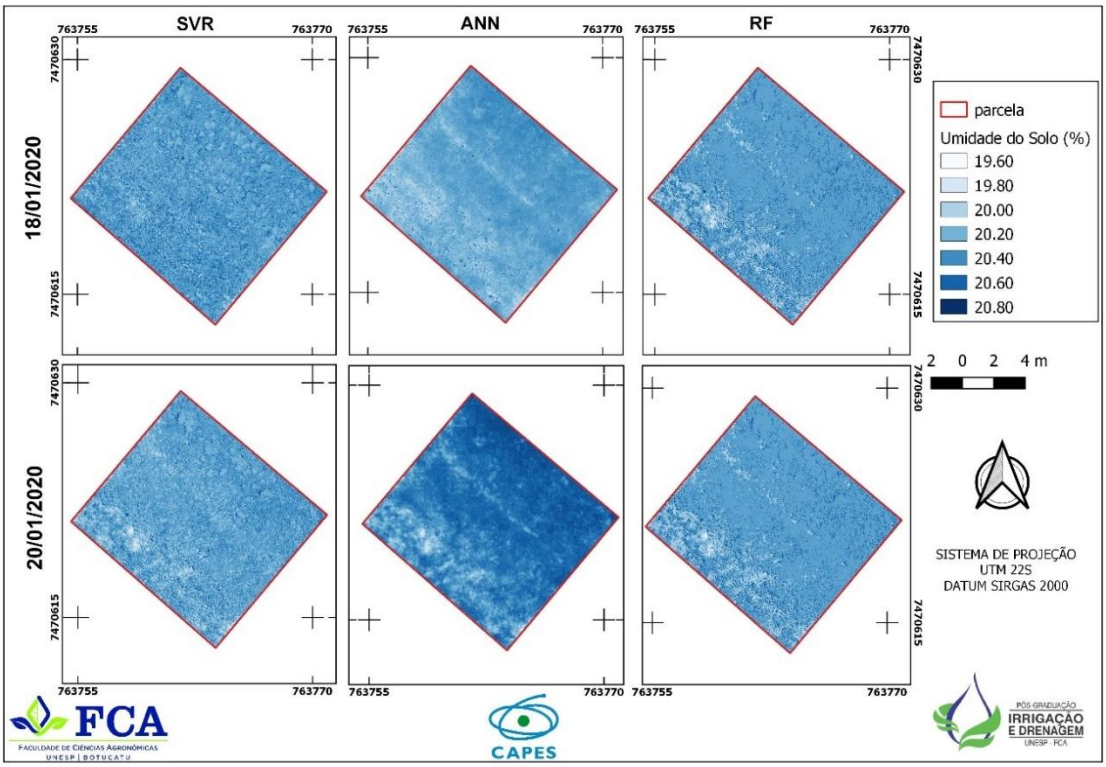

Os mapas foram gerados em alta resolução com pixel de 12 cm, o que pode não ser tecnicamente viável para manejo o da irrigação, porém os dados podem ser reamostrados por meio da técnica de *downsampling* que permite a redução da resolução espacial. Outra alternativa é a realização de voos em altitude superior a 120 m, que é mais interessante para levantamentos em grandes áreas como as ocupadas por sistemas de irrigação por pivô central. Entretanto, ressalta-se que o objetivo deste trabalho foi demonstrar a precisão dos algoritmos de *machine learning* na estimativa de umidade do solo, utilizando para tal, dados coletados por um sensor óptico de baixo custo. A possibilidade de coletar dados em qualquer intervalo de tempo utilizando um VANT, somada à capacidade de reconhecimento de padrões por algoritmos de *machine learning*, configura-se uma excelente ferramenta para a aquisição remot de dados de umidade do solo.

3.5 CONCLUSÕES

Foi possível demonstrar nesse estudo, a utilidade dos algoritmos de *machine learning* para a estimativa da umidade do solo a partir de imagens multiespectrais de alta resolução coletadas por VANT. As bandas do Vermelho e Infravermelho próximo foram as mais correlacionadas com a tensão de água no solo na profundidade de 20 cm. A performance dos algoritmos SVR e ANN foram similares, apresentando pouca diferença em relação ao ajuste da regressão. O melhor algoritmo para a estimativa de umidade do solo, com base nos dados analisados, foi o SVR, que apresentou um RMSE de 0,46 vol. % na estimativa de umidade do solo nos dados de teste e R^2 de 0,71. Os mapas gerados pelos algoritmos demonstram a alta variabilidade espacial da umidade do solo e podem ser utilizados para o monitoramento dela

em qualquer escala temporal, sendo a técnica aqui apresentada limitada somente por condições meteorologicas que podem impedir o levantamento de dados por meio do uso de um VANT.

A performance dos algoritmos de *machine learning*, em especial as Redes Neurais, é influenciada pelo tamanho dos dados de treinamento, podendo haver *overfitting* em conjuntos de dados não tão extensos, o que representa uma limitação dos resultados aqui apresentados. Todavia, destaca-se que novas campanhas podem ser realizadas para a coleta de dados, e esses dados utilizados para retreinar os modelos, aumentando assim, cada vez mais a precisão deles.

Esse estudo fornece evidências de que o *machine learning* pode ser empregado na estimativa, por método indireto, do teor de água do solo, sendo possível obter resultados de alta acurácia mesmo utilizando câmeras de baixo custo acopladas ao veículo aéreo não tripulado.

AGRADECIMENTOS

Os autores agradecem à CAPES pelo auxilio DS 88882.433001/2019-01 e ao CNPQ pelo auxilio 131325/2020-5, essenciais para a realização deste trabalho.

REFERÊNCIAS

ABOUTALEBI, M.; ALLEN, L. N.; TORRES-RUA, A. F.; MCKEE, M.; COOPMANS, C. Estimation of soil moisture at different soil levels using machine learning techniques and unmanned aerial vehicle (UAV) multispectral imagery". *In*: SPIE DEFENSE + COMMERCIAL SENSING, 6., 2019, Baltimore. **Proceedings** […]. Baltimore: Autonomous Air and Ground Sensing Systems for Agricultural Optimization and Phenotyping, 2019. p. 1-12.

AHMAD, S.; KALRA, A.; STEPHEN, H. Estimating soil moisture using remote sensing data: A machine learning approach. **Advances in Water Resources**, Iowa City, v. 33, p. 69-80, 2010.

AITKENHEAD, M. J.; COULL, M.; TOWERS, W.; HUDSON, G.; BLACK, H. I. J. Prediction of soil characteristics and colour using data from the National Soils Inventory of Scotland. **Geoderma**, Amsterdã, v. 200/201, p. 99-107, 2013.

ARAYA, S. N.; FRYJOFF-HUNG, A.; ANDERSON, A.; VIERS, J. H.; GHEZZEHEI, T. A. Advances in soil moisture retrieval from multispectral remote sensing using unoccupied aircraft systems and machine learning techniques. **Hydrologic Earth Systems Science**, Gottingen, v. 25, p. 2739-2758, 2021.

ARRUDA, L. E. V.; FIGUEIRÊDO, V. B.; LEVIEN, S. L. A.; MEDEIROS, J. F. Desenvolvimento de um tensiômetro digital com sistema de aquisição e armazenamento de dados. **Irriga**, Botucatu, v. 1, n. 1, p. 11-20, 2017.

BISHOP, C. M. **Neural Networks for Pattern Recognition**. Oxford: Oxford University Press, 1995.

BREIMAN, L. Random forests. **Machine Learning**, New Jersey, v. 45, p. 5-32, 2001.

BRITO, A. S.; LIBARDI, P. L.; MOTA, J. C. A.; MORAES, S. O. Desempenho do tensiômetro com diferentes sistemas de leitura. **Revista Brasileira de Ciência do Solo**, Viçosa, v. 33, n. 1, p. 17-24, 2009.

BRITO, A. S.; LIBARDI, P. L.; MOTA, J. C. A.; KLEIN, V. A. Variação diurno-noturna do potencial mátrico e gradiente de potencial total da água no solo. **Revista Brasileira de Ciência do Solo**, Viçosa, v. 38, n. 1, p. 128-134, 2014.

CAMARGO, A. P.; GROHMANN, F.; CAMARGO, M. B. P. Tensiômetro simples de leitura direta. **Pesquisa Agropecuária Brasileira**, Brasília, DF, v. 17, n. 12, p. 1763-72, 1982.

DOBRIYAL, P.; QURESHI, A.; BADOLA, R.; HUSSAIN, S. A. A review of the methods available for estimating soil moisture and its implications for water resource management. **Journal of Hydrology**, Amsterdam, v. 458-459, p. 110-117, 2012.

DUKES, M. D.; ZOTARELLI, L.; MORGAN, K. T. Use of irrigation technologies for vegetable crops in Florida. **HortTechnology**, Alexandria, v. 20, n. 1, p. 133-142, 2010.
FREITAS, W. A.; CARVALHO, J. A.; BRAGA, R. A.; ANDRADE, M. J. B. Manejo da irrigação utilizando sensor da umidade do solo alternativo. **Revista Brasileira de Engenharia Agrícola e Ambiental**, Campina Grande, v. 16, n. 3, p. 268-274, 2012.

GE, X.; WANG, J.; DING, J.; CAO, X.; ZHANG, Z.; LIU, J.; LI, X. Combining UAV-based hyperspectral imagery and machine learning algorithms for soil moisture content monitoring. **Environmental Science**, Amsterdã, v. 7, n. 6929, p. 1-27, 2019.

GOMES, A. P. A.; QUEIROZ, D. M.; VALENTE, D. S. M.; PINTO, F. A. C.; ROSAS, J. T. F. Comparing a single-sensor câmera with a multisensor câmera for monitoring coffee crop using unmanned aerial vehicles. **Engenharia Agrícola**, Jaboticabal, v. 41, n. 1, p. 87-97, 2022.

GROSSAN, C.; ABRAHAM, A. **Intelligent Systems**: A modern approach. Berlin: Springer, 2011.

HASSAN-ESFAHANI, L.; TORRES-RUA, A.; JENSEN, A.; MCKEE, M. Assessment of surface soil moisture using high-resolution multi-spectral imagery and artificial neural networks. ***Remote Sensing***, Basel, v. *7*, n. 3, p. 2627-2646, 2015.

HAYKIN, S. **Neural Networks**: A Comprehensive Foundation. 2. ed. New Jersey: Prentice Hall, 1999.

HUISMAN, J. A.; HUBBARD, S. S.; REDMAN, J. D.; ANNAN, A. P. Measuring soil water content with ground penetrating radar: a review. **Vadose Zone Journal**, Madison, v. 2, n. 4, p. 476-491, 2003.

JENSEN, J. R. **Remote sensing of the environment**: an earth resource perspective. 2. ed. New Delhi: Pearson Education, 2009.

JIANG, H.; COTTON, W. Soil moisture estimation using an artificial neural network: A feasibility study. **Canadian Journal of Remote Sensing**. Quebec, v. 30, n. 5, p. 827-839, 2004.

KÖPPEN, W.; GEIGER, R. **Klimate der Erde**. Gota: Justus Perthes, 1928.

KOVAČEVIC, M.; BAJAT, B.; GAJIĆ, B. Soil type classification and estimation of soil properties using support vector machines. **Geoderma**, Amsterdã v. 154, n. 3/4, p. 340-347, 2010.

KORNELSEN, K. C.; COULIBALY, P. Root-zone soil moisture estimation using data-driven methods. **Water Resources Research**, New Jersey, v. 50, p. 2946-2962, 2014.

LIBARDI, P. L. **Dinâmica da água no solo**. São Paulo: EDUSP, 2005.

MANSUY, N.; THIFFAULT, E.; PARÉ, D.; BERNIER, P.; GUINDON, L.; VILLEMAIRE, P.; POIRIER, V.; BEAUDOIN, A. Digital mapping of soil properties in Canadian managed forests at 250m of resolution using the k-nearest neighbor method. **Geoderma**, Amsterdã, v. 235/236, p. 59-73, 2014.

MCCULLOCH W. S.; PITTS. W. A logical calculus of the ideas immanent in nervous activity, **Bulletin of Mathematical Biophysics**, New York, v. 5, p. 115-133, 1943.

MONTESANO, F. F.; SERIO, F.; MININNI, C.; SIGNORE, A.; PARENTE, A.; SANTAMARIA, P. Tensiometer-based irrigation management of subirrigated soilless tomato: effects of substrate matric potential control on crop performance. **Frontiers in Plant Science**, Lausanne, v. 6, n. 1150, p. 1-11, 2015.

NOVO, E. M. L. **Sensoriamento Remoto**: princípios e aplicações. Sao Paulo: Edgard Blucher, 2008.

OR, D. Who invented the tensiometer? **Soil Science Society of America Journal**, New Jersey, v. 65, n. 1, p. 1-3, 2001.

PONZONI, F. J.; SHIMABUKURO, Y. E. **Sensoriamento Remoto no estudo da vegetação**. São José dos Campos: Parêntese, 2010.

PRIORI, S.; BIANCONI, N.; CONSTANTINI, E. A. C. Can γ-radiometrics predict soil textural data and stoniness in different parent materials? A comparison of two machine learning methods. **Geoderma**, Amsterdã, v. 226/227, p. 354-364, 2014.

PUJOL, J. C. F.; PINTO, J. M. A. A Neural-network approach to fatigue life prediction. **International Journal of Fatigue**, Amsterdã, v. 33, n. 3, p. 313-322, 2011.

ROSA, R. **Introdução ao sensoriamento remoto**. 7. ed. Uberlândia: EDUFU, 2009.

ROSENBLATT, F. **Principles of neurodynamics**: perceptrons and the theory of brain mechanisms. New York: Spartan Books, 1962.

ROSSI, M. **Mapa pedológico do estado de São Paulo**: revisado e ampliado. São Paulo: Instituto Florestal, 2017.

SEGAL, M. R. **Machine Learning Benchmarks and Random Forest Regression**. San Francisco: University of California, *2004. Disponível em: h*ttps://escholarship.org/uc/item/35x3v9t4. Acesso em: 09 fev. 2022.

SILVEIRA, C. T.; OKA-FIORI, C.; SANTOS, L. J. C.; SIRTOLI, A. E.; SILVA, C. R.; BOTELHO, M. F. Soil prediction using artificial neural networks and topographic attributes. **Geoderma**, Amsterdã, v. 195/196, p. 165-172, 2013.

SMOLA, J. **Regression estimation with support vector learning machines**. Dissertação (Mestrado em Física) – Technische Universit at Munchen, Munique, 1996.
SMOLA, A. J.; SCHOLKOPF, B. **A tutorial on support vector regression**. London: Royal Holloway College, 2004.
TEIXEIRA, A. S.; COELHO, S. L. Desenvolvimento e calibração de um tensiômetro eletrônico de leitura automática. **Engenharia Agrícola**, Jaboticabal, v. 25, n. 2, p. 367-376, 2005.

THALHEIMER, M. A low cost electronic tensiometer system for continuous monitoring of soil water potential. **Journal of Agricultural Engineering**, Pavia, v. 44, n. 3, p. 114-119, 2013.

VAN GENUCHTEN, M. T. A closed form equation for predicting the hydraulic conductivity of unsaturated soils. **Soil Science Society of America Journal**, Madison, v. 44, n. 5, p. 892-898, 1980.

VAPNIK, V. **Statistical Learning Theory**. New York: Springer, 1998.

WU, C. H.; dHO, J. M.; LEE, D. T. Travel-time prediction with support vector regression. **IEEE Transactions on intelligent transportation systems**, Blacksburg, v. 5, n. 4, p. 276-281, 2004.

GENERAL CONCLUSION

We evaluated the performance of SAFER algorithm in the estimation of actual evapotranspiration using ground truth data collected by six eddy covariance (EC) towers. The model was calibrated using the EC data and the results were validated. The calibration process did not have a strong fit with a R2 of 0.12 for Landsat images and ranging from 0.12 to 0.40 for Sentinel images.

The model improved substantially after the calibration process, demonstrating that the calibration process is required to the correct usage of SAFER evapotranspiration results. Using Landsat images, the RMSE on daily actual evapotranspiration (ET_a) was 0.70 mm d^{-1}. For Sentinel images the RMSE was 0.74 mm d^{-1} demonstrating the potential for the usage of both SAFER versions using and not using the thermal band. SAFER estimation of Land Surface Temperature (LST) was evaluated using surface temperature data derived from upwelling longwave radiation measurements. The results showed that the algorithm provides a good approximation of LST with an RMSE of 3.79 C d^{-1}. Safer was also able to capture the season trend and estimate with accuracy the cumulative evapotranspiration for the analyzed season using information from both satellites.

In this study we also evaluated the performance of machine learning algorithms for the estimation of soil moisture using UAV images. The results showed that all the models had an accurate estimate of soil moisture content. The support vector machine regressor presented a RMSE of 0.46 and a R^2 of 0.71 for the validation dataset.

The results presented in this study highlight the potential for the usage of remote sensing images supported by empirical and machine learning models for agricultural water management. Geospatial data can provide accurate information about crops providing farmers recommendations for the increase water productivity guiding agriculture trough a sustainable development.

REFERENCES

ABOUTALEBI, M.; ALLEN, L. N.; TORRES-RUA, A. F.; MCKEE, M; COOPMANS, C. **"Estimation of soil moisture at different soil levels using machine learning techniques and unmanned aerial vehicle (UAV) multispectral imagery.** In: **Proceedings of SPIE 11008,** Autonomous Air and Ground Sensing Systems for Agricultural Optimization and Phenotyping IV, 2019.

COURAULT, D.; SEGUIN, B.; OLIOSO, A. **Review on estimation of evapotranspiration from remote sensing data: From empirical to numerical modeling approaches**. Irrigation and Drainage Systems*,* v 19, p. 223–249, 2005.

DARI, J.; QUINTANA-SEGUÍ, P.; ESCORIHUELA, M.J.; STEFAN, V., BROCCA, L.; MORBIDELLI, R. **Detecting and mapping irrigated areas in a Mediterranean environment by using remote sensing soil moisture and a land surface model**. Journal of Hydrology, v 596, 2021.

DOLAN, F., LAMONTAGNE, J., LINK, R**. Evaluating the economic impact of water scarcity in a changing world**. Nature Communication **12,** 1915, 2021.

DONG, Z.; JIN S. **Evaluation of the Land GNSS-Reflected DDM Coherence on Soil Moisture Estimation from CYGNSS Data**. Remote Sensing. v13(4):570, 2021.

KERR, Y. H. **Soil moisture from space: Where are we?** Hydrogeology Journal, v15(1), p. 117–120*,* 2006.

KIM, J.; VERMA, S. **Manual:** Measurement of Evapotranspiration by the Bowen Ratio Energy Balance Method. Papers in Natural Resources, v.1411, 1985.

KUSTAS, W.P.; NORMAN, J.M. **Use of remote sensing for evapotranspiration monitoring over land surfaces.** Hydrolical Sciences Journal, v*41*, p.495–516, 1996.

KUSTAS, W.P.; NORMAN, J.M. **Evaluation of soil and vege-tation heat flux predictions using a simple two-source model with radiometric temperatures for partial canopy cover**. Agricultural and Forest Meteorology, v.94, p13–29, 1999.

PANG, X.; LEI, H.; CONG, Z.; YANG, H.; DUAN, L.; YANG, D. **Long term variation of evapotranspiration and water balance based on upscaling eddy covariance observations over the temperate semi-arid grassland of China**. Agricultural and Forest Meteorology, v308–309, 2021.

REICHERT, J.M.; PREVEDELLO, J.; GUBIANI, P.I.; VOGELMANN, E.S.; REINERT, D.J.; CONSENSA, C.O.B.; SOARES, J.C.W., SRINIVASAN, R. **Eucalyptus tree stockings effect on water balance and use efficiency in subtropical sandy soil.** Forest Ecology and Management, Volume 497, 2021.

SAFRIEL, U.; ADEEL, Z. Dryland systems. In: HASSAN, R.; SCHOLES, R.; ASH, N. **Ecosystems and human wellbeing, current state and trends**, vol 1. Island Press, Washington, pp 625-658, 2005.

SOUSA, D.d.P.; FERNANDES, T.F.S.; TAVARES, L.B. **Estimation of evapotranspiration and single and dual crop coefficients of acai palm in the Eastern Amazon (Brazil) using the Bowen ratio system**. Irrigation Science v 39, p. 5–22, 2021.

SUN, G.; ALSTAD, K.; CHEN, J.Q.; Chen, S.P.; FORD, C.R.; LIN, G.H.; ZHANG, Z.Q. **A general predictive model for estimating monthly ecosystem evapotranspiration.** Ecohydrology, 4 (2), p.245-255, 2011.

WANG, L.; QU, J.J. **Satellite remote sensing applications for surface soil moisture monitoring: A review**. Frontiers in Earth Science, v3, p. 237–247, 2009.

YANG, Y.; ANDERSON, M.C.; GAO, F. HAIN, C. R.; SEMMENS, K. A.; KUSTAS, W. P., NOORMETS, A.; WYNNE, R.H.; THOMAS, V.A.; SUN, G. **Daily Landsat-scale evapotranspiration estimation over a forest landscape in North Carolina**, USA using multisatellite data fusion. Hydrolygy and Earth Systems Science, 2016.

ZHANG, K., KIMBALL, J.S.; RUNNING, S. **A review of remote sensing based actual evapotranspiration**. Water, v3, p.834–853, 2016.